The Electronic Structure of Spin Ladders and Spin Chains Studied by Ellipsometry

Christina Hilgers

The Electronic Structure of Spin Ladders and Spin Chains Studied by Ellipsometry

Inaugural Dissertation

zur

Erlangung des Doktorgrades
der Mathematisch-Naturwissenschaftlichen Fakultät
der Universität zu Köln

vorgelegt von

Christina Hilgers

aus Köln

Köln, Februar 2009

Berichterstatter:	Prof. Dr. A. Freimuth Prof. Dr. M. Grüninger
Vorsitzender der Prüfungskommission:	Prof. Dr. L. Bohatý
Tag der mündlichen Prüfung:	30. April 2009

Contents

1 Introduction

The physical properties of condensed matter are ruled by the behavior of the valence electrons of the building atoms. In the conventional picture, bands are formed in a crystal and the compound can have metallic or insulating properties depending on the band filling. However, if the electron-electron interactions are strong, band theory can fail and a compound with a half-filled band can be a strong insulator. In such strongly correlated systems, the complex interplay between charge, spin, lattice and orbital degrees of freedom produces many interesting effects. The most prominent examples are high-transition temperature superconductivity (HTSC) and colossal magneto-resistance (CMR) in the transition metal oxides.

In these materials, many competing ground states exist that lead to complicated phase diagrams. Much experimental and theoretical effort has been spent in the field of transition metal oxides to understand their behavior and has often led to more questions. One interesting finding is that these materials are not homogeneous on the nanoscale which leads to the idea that many of these investigations have to be considered in a broader range of complexity [1].

In the 2D cuprate superconductors it is discussed that the stripe-ordered phase competes with superconductivity [2–4]. Similarly, in the hole-doped spin ladders investigated here, a competition between superconductivity [5, 6] and an insulating charge-ordered state or hole crystal has been predicted [5, 7, 8]. The spin ladders belong to the cuprate family and can be regarded as low-dimensional relatives of the high-T_C materials. The ladders are formed by one-dimensional copper-oxide chains that couple via oxygen ions to neighboring chains. They build a bridge between 1D and 2D. The effect of dimensionality on the electronic excitation spectrum is crucial in correlated electron systems as discussed in chapter two.

Until today, the complex material $Sr_{14-x}Ca_xCu_{24}O_{41}$ that has been investigated within the scope of this thesis, is the only spin-ladder compound in which hole doping could be achieved. This compound shows many interesting phases that have not yet fully been understood despite numerous experimental and theoretical efforts. In the hole-doped spin ladders an insulator to metal transition with Ca substitution is reported [9–11]. For the compound x = 13.6 superconductivity under hydrostatic pressure of 3 GPa was reported [12]. However, without Ca the material shows all signatures of charge ordering, i.e. a charge-carrier density modulation in real space [13–16]. A recent RIXS study [17, 18] found evidence that this charge ordering is not of a Peierls type [19], i.e. not driven by electron-phonon

coupling but by many body interactions that also lead to a periodic modulation of the charge density and thus should show similar signatures in experiment. As a matter of fact, calling SCCO a spin ladder is an oversimplification. This compound is a complicated layer structure that in addition to the spin-ladder layers also contains layers of one-dimensional chains. The six hole carriers per unit cell are distributed among the chain and the ladder subsystem and even today the discussion about where the holes are located and how they are redistributed with Ca content or temperature is heavily debated. In addition, there are still unexplained low energy absorptions for x$\geq$ 8 observed in the far infrared optical conductivity [11, 20]. Trying to shed new light onto the open discussion, this thesis focuses on a systematic investigation of the electronic structure of the spin-ladder compounds by means of optical spectroscopy as a function of doping and temperature. In addition, the one-dimensional zig-zag chain $SrCuO_2$ for which spin-charge separation has been reported [21, 22] is investigated. In this compound, an excitonic resonance was observed closely above the gap [23]. We address the temperature dependence of the electronic excitation spectrum in searching for a unified description of the electron-hole excitations in 1D and 2D.

Optical spectroscopy is a powerful experimental technique of studying the electrodynamic response of correlated electron systems. The optical conductivity contains contributions of lattice vibrations, electronic intra-band and interband transitions, magnetic excitations or collective modes. Regarding the intra-band excitations, free charge-carrier excitations or plasmons lead to prominent features in the spectra and concerning interband transitions, bound electron-hole pairs or excitons can drastically change the absorption spectra. All these features deliver valuable microscopic information about the electronic structure of solids. The optical spectra were acquired by Fourier transform spectroscopy in the energy region from 10 meV to 2 eV and by ellipsometry in the interband region between 0.8 - 5 eV. This thesis is organized as follows: The second chapter gives an overview of the physics of correlated electron systems with focus on the interband excitations and excitonic effects in one-dimensional and two-dimensional cuprates. The third chapter is dedicated to some fundamentals of optical spectroscopy with focus on the newly implemented measurement technique of spectroscopic ellipsometry. Chapter four addresses the experimental techniques of Fourier transform spectroscopy and ellipsometry and focuses on the spectroscopic ellipsometer put into operation by my colleague Alexander Gößling and myself. In chapter five the properties of the spin ladder compounds $(La,Sr,Ca)_{14}Cu_{24}O_{41}$ are summarized before the results of the low-temperature ellipsometry and Fourier transform spectroscopy are presented for the undoped spin-ladder compound $La_{5.2}Ca_{8.8}Cu_{24}O_{41}$ (LCO) and the hole doped spin ladders $Sr_{14-x}Ca_xCu_{24}O_{41}$ for x = 0 (SCO), x = 5 and 8 (SCCO). An interpretation of the electronic structure, taking into account other experimental and theoretical results, follows. In addition to that, a spectral weight analysis is carried out for x = 0, 5, and 8 from the far infrared region to

the energy range of interband transitions (10 meV to 5 eV). Chapter six shows the results of the undoped one-dimensional zig-zag chain $SrCuO_2$ where an excitonic resonance is discovered [23]. The temperature dependence of the electron-hole excitations is investigated. All our results are summarized in chapter seven. Some more details about ellipsometry are found in the appendix.

2 Physics of Transition-Metal Compounds

2.1 The Hubbard model

In the most simple approach, correlated electron systems are described by the single-band Hubbard model [24] which captures the competition between on-site Coulomb repulsion U on the transition-metal sites and the inter-site transfer probability t representing the kinetic energy. For U larger than the bandwidth W, the band splits into a lower and an upper Hubbard band (LHB and UHB). At exactly half filling, the system becomes a Mott-Hubbard insulator with one localized electron or hole per site. Often, the ground state is antiferromagnetic (AF) allowing for virtual hopping processes where kinetic energy is partly recovered. Such an AF insulator is described by the following Hamiltonian:

$$H = -t \sum_{\langle i,j \rangle,\sigma} (c^{\dagger}_{i,\sigma} c_{j,\sigma} + H.c.) + U \sum_{i} n_{i,\uparrow} n_{i,\downarrow} \tag{2.1}$$

where $c^{\dagger}_{i,\sigma}(c_{i,\sigma})$ represent the creator (annihilator) operators on site i with spin $\sigma = (\uparrow \downarrow)$, and $n_{i,\sigma} = c^{\dagger}_{i,\sigma} c_{j,\sigma}$ stands for the number operator. In the cuprates, the Hubbard U lies in the range of 7-10 eV.

t-J model and Heisenberg model

The t-J model was derived to describe the low-energy physics of Mott-Hubbard systems, i.e. double occupancy is explicitly excluded. In case of hole doping, it captures the metallic properties of those systems. For $U >> W$, the t-J model is described by the following Hamiltonian:

$$H = -t \sum_{\langle i,j \rangle,\sigma} (\tilde{c}^{\dagger}_{i,\sigma} \tilde{c}_{j,\sigma} + H.c.) + J \sum_{\langle i,j \rangle} (\mathbf{S}_i \mathbf{S}_j - \frac{1}{4} n_i n_j) \tag{2.2}$$

where $n_i = \sum_{\alpha} \tilde{c}^{\dagger}_{i,\alpha} \tilde{c}_{i,\alpha}$ and $\tilde{c}^{\dagger}_{i,\sigma} = (1 - c^{\dagger}_{i,-\sigma} c_{i,-\sigma}) c^{\dagger}_{i,\sigma}$ are the corresponding operators in case of a projection onto the Hilbert space without double occupancy and $J = 4t^2/U$ is the exchange coupling constant. $\mathbf{S}_i$ defines the spin-operator on site i. The sum $\langle i, j \rangle$ is carried out over nearest neighbors. The first term in equation

2.2 represents charge carrier hopping from a singly occupied site to an empty site. The second term represents the exchange part. The three-site hopping term has been omitted for simplicity. In case of a small number of correlated holes in a doped Mott-insulator, it can come to hole localization and as described later in this section, in case of quasi-1D spin ladders a hole-pairing mechanism leading to superconductivity was proprosed by Dagotto [5]. In case of exactly half filling, i. e. one spin on each site, charge transport is suppressed and for the elementary excitations there remain, apart from phononic excitations, only spin degrees of freedom for energies much smaller than U. Then the first term in equation 2.2 vanishes and the t-J model reduces to the Heisenberg model which describes quantum magnets:

$$H = J \sum_{\langle i,j \rangle} (\mathbf{S}_i \mathbf{S}_j - \frac{1}{4} n_i n_j) \tag{2.3}$$

This means, the energy scales can be separated into a low-energy (spin only) and high-energy (charge fluctuations) region.

2.2 Magnetic Properties of Low-Dimensional Quantum Spin Systems

It has already been shown by Bethe [25] that a one-dimensional S=1/2 quantum Heisenberg antiferromagnet does not show long-range order, even at T=0 K due to strong quantum fluctuations. Such a quantum disordered state is called a spin liquid [26, 27]. For the 2D S=1/2 square lattice, one expects long-range order only at T=0 K. The excitations from a spin-liquid ground state differ from those of a long-range ordered state. In the following, the properties of those new excitations in 1D Heisenberg spin chains and quasi-1D spin 1/2 two-leg ladders shall be described briefly.

1D S=1/2 Chains

The 1D Heisenberg chain is described by the Hamiltonian of equation (2.3) with isotropic exchange coupling J where only spin degrees of freedom remain for low-energy excitations. The elementary excitations of this spin liquid are called spinons and carry spin $S = 1/2$. Therefore, always two spinons are created with one spin flip to fulfill $\Delta S = 1$. This is shown in Fig. 2.1 (a) for a Néel-type ground state. The spinons are visualized by the blue bars and might be identified with the domain wall between two antiferromagnetic domains. In case of the excitation of two spinons, e.g. in neutron scattering, only the total momentum $k = k_1 + k_2$ is

defined, [1] leading to a gapless two-spinon excitation continuum $E(k)$ as depicted in Fig. 2.1(b).

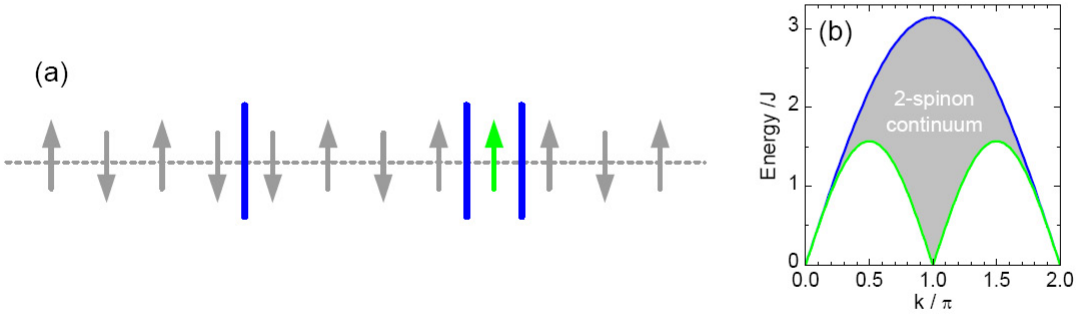

Figure 2.1: (a) Sketch of an AF 1D Heisenberg chain where one spin has been flipped ($\Delta S = 1$, green arrow) creating two spinons (blue bars) with $S = 1/2$ each. The blue bar on the left represents a domain wall, i.e. a further spinon. (b) Dispersion relation of the two spinon continnuum [25, 28–30].

Quasi-1D S=1/2 Ladders

The model of a two-leg S=1/2 ladder was first examined by Dagotto [5, 31], originally for the compound $(VO)_2P_2O_7$. The ladder structure is formed by transition-metal sites connected to each other by superexchange interaction of the transition-metal spin-1/2 moments over oxygen ions. So called legs and rungs can be established and different scenarios can be developed by varying the relative strength of the coupling constants between rungs and legs. The ladders are an interesting object of studies because they can be regarded as crossover from 1D to 2D. Ladders with an even number of legs are expected to be gapped spin liquids and ladders with an odd number of legs should be gapless for the lowest magnetic excitations [5, 32]. The Hamiltonian of a $S = 1/2$ two-leg ladder can be written as:

$$H = \sum_i J_{\parallel}(\mathbf{S}_{1,i}\mathbf{S}_{1,i+1} + \mathbf{S}_{2,i}\mathbf{S}_{2,i+1}) + J_{\perp}\mathbf{S}_{1,i}\mathbf{S}_{2,i} \tag{2.4}$$

The first index of the spin operators denotes the legs and the second index counts the rungs. In the so called strong-coupling limit, $J_{\perp}$ is much stronger than the coupling $J_{\parallel}$ along the legs. Then the ground state consists of a direct product of spin singlets, one on each rung. The elementary excitation from a singlet to a triplet (also called triplon) will cost the energy of the exchange coupling $J_{\perp}$.

[1] In neutron scattering the measured change in neutron spin is $\Delta S = 1$, i.e. two spinons are created by this scattering process. The total momentum transfer k is randomly divided among the two spinons.

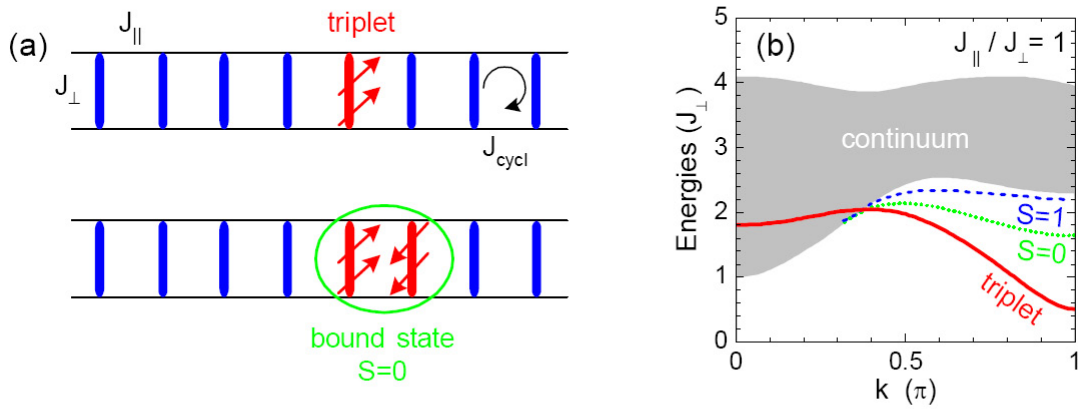

Figure 2.2: (a) Sketch of a two-leg S=1/2 ladder showing the elementary excitations. These elementary triplet states are called triplons. The exchange couplings along rungs and legs can lead to bound states of triplons. (b) The elementary triplet branch, the two-triplet continuum and lower lying bands for bound states with $S = 0$ and $S = 1$ for $J_{\|}$=$J_{\perp}$ [33].

For finite values of $J_{\|}$, these excitations can propagate along the ladder, i.e. they acquire a dispersion as shown in Fig. 2.2 (b). Moreover, the two-triplon continuum as well as the $S = 0$ and $S = 1$ two-triplon bound states are shown. In the limit $J_{\perp} = 0$ the legs decouple and the spin gap of such isolated 1D chains vanishes. This means, a spin excitation will cost no energy. However, it was found that a spin gap opens immediately as soon as a nonzero $J_{\perp}$ is introduced [34]. The $S = 0$ two-triplet bound state has been experimentally observed in $(La,Sr,Ca)_{14}Cu_{24}O_{41}$ by optical spectroscopy [35, 36].

The undoped two-leg ladder is experimentally realized in the compound $SrCu_2O_3$ [37] and the existence of a finite spin gap was proved by magnetic susceptibility measurements.

In 1988, the first hole-doped spin ladder $Sr_{14-x}Ca_xCu_{24}O_{41}$ (SCCO) was reported by McCarron *et al.* [38]. The system is inherently doped with six holes per formula unit. As a matter of fact, they represent up to today the only ladder material where hole doping has been achieved at all. As described in more detail in the next chapter, superconductivity has been predicted for hole-doped ladders by Dagotto *et al.* [5] and experimentally found in SCCO for x>13.6 under high pressure [12].

2.3 Cuprates

After the discovery of high-T_C superconductivity (HTSC) in $La_{1.85}Ba_{0.15}CuO_4$ [39] the family of quasi two-dimensional cuprates became one of the most intensively

studied class of materials in solid state physics. Their physical properties are ruled by the behavior of the electrons within two-dimensional copper-oxide layers. The

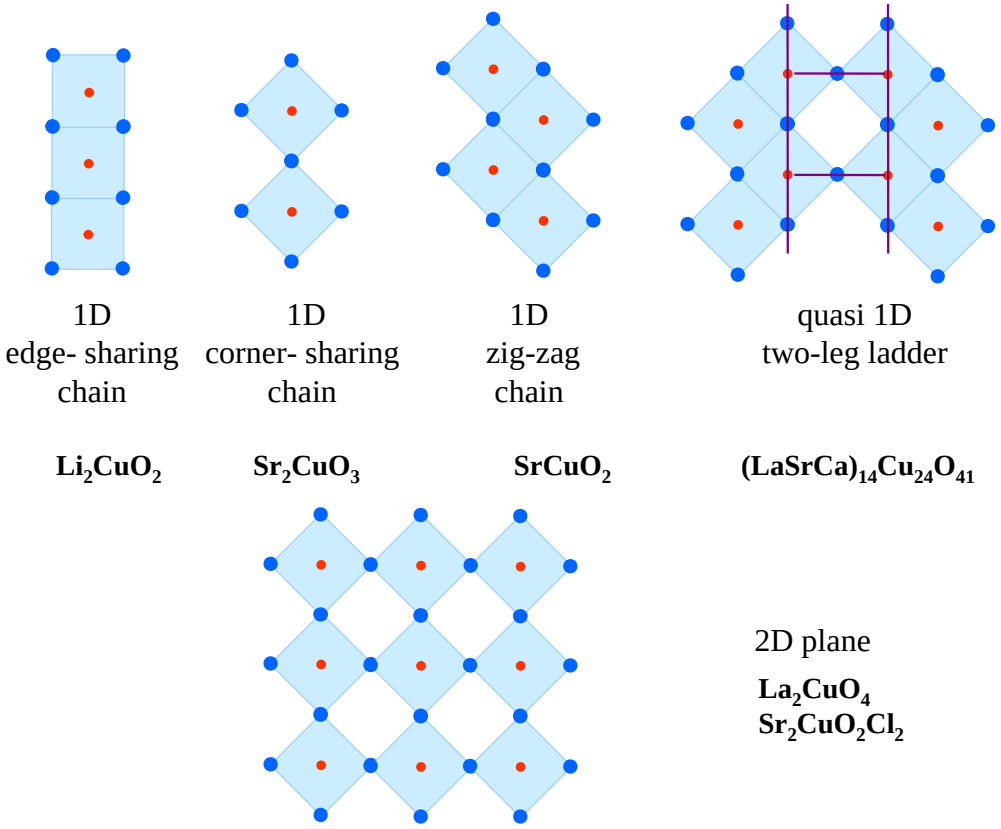

Figure 2.3: Sketch of different Cu-O networks that are the main structural units in low-dimensional cuprates. The connection of CuO_4 plaquettes over corners (180° Cu-O-Cu superexchange interaction) or edges (90° Cu-O-Cu superexchange) rules the nature of the ground state.

cuprates combine two aspects that lead to fascinating physical behavior, namely low dimensionality and strong correlation. Many structures were synthesized after the discovery of high-T_C superconductivity in order to understand the underlying mechanism.

Examples of the insulating 2D cuprates or parent compounds are $Sr_2CuO_2Cl_2$, La_2CuO_4, and $YBa_2Cu_3O_6$ that crystallize in tetragonal or orthorhombic symmetry. As shown in Fig. 2.3, they share the 2D copper-oxide planes allowing for carrier hopping via oxygen orbitals. The electronic behavior from insulating to superconducting can be controlled by charge-carrier doping, e.g. by substituting La^{3+} by Sr^{2+} in La_2CuO_4 or by changing the oxygen content in $YBa_2Cu_3O_{6+y}$.

In addition to compounds with 2D copper-oxide layers, there also exist 1D and

quasi-1D structures. These can be realized by connecting CuO_4 units by their corners, edges, or both as depicted in Fig. 2.3, leading to different behavior due to the different exchange interaction. The two-leg spin ladders shown in Fig. 2.3 build a bridge between 1D and 2D.

2.4 Electron-Hole Excitations

We focus here on the investigations on electron-hole excitations in the cuprates because their nature is still an important question in the understanding of high-T_C superconductivity and in general in correlated electron systems.

The undoped compounds have in common that the formal valence of Cu is +2 which means the electron configuration is $3d^9$. Due to the crystal field, the degeneracy of the 5 Cu $3d$ orbitals is lifted, as shown schematically in Fig. 2.4 for the case of four surrounding oxygen ligands. It follows that the $d_{x^2-y^2}$ orbital is only half filled, and since the band width is small, electron-electron interaction is important. It is widely accepted that in the cuprates the Cu-O hybridization plays an important role and that the lowest-lying charge fluctuations are not of d-d type as described in the one-band Hubbard model of equation 2.1 but of charge-transfer (CT) or p-d type [40]. This means, the lowest-lying electron-hole excitations correspond to the transfer of electrons from oxygen ions to copper ions. The CT gap involves the charge-fluctuation energy Δ which directly depends on the electronegativity of the anion, in this case oxygen, and the Madelung potential [40]. In other words, the nature of the conductivity gap depends on the relative size of U and Δ, yielding Mott-Hubbard and charge-transfer type insulators (see Fig. 2.5). The most simple model then is the three-band Hubbard model as proposed by Emery [41]

$$\begin{aligned} H = \epsilon_d \sum_{i,\sigma} n^d_{i,\sigma} + \epsilon_p \sum_{j,\sigma} n^p_{j,\sigma} + \sum_{\langle i,j\rangle\sigma} t^{ij}_{pd}(d^\dagger_{i,\sigma} p_{j,\sigma} + H.c.) \\ + \sum_{\langle j,j'\rangle,\sigma} t^{jj'}_{pp}(p^\dagger_{j,\sigma} p_{j',\sigma} + H.c.) + U_d \sum_i n^d_{i,\uparrow} n^d_{i,\downarrow} \\ + U_p \sum_j n^p_{j,\uparrow} n^p_{j,\downarrow} + U_{pd} \sum_{\langle ij\rangle,\sigma,\sigma'} n^d_{i,\sigma} n^p_{j,\sigma'} \end{aligned}$$

The index $i(j)$ denotes Cu (O) sites, and $d^\dagger_{i,\sigma}$ ($d_{i,\sigma}$), $p^\dagger_{j,\sigma}$ ($p_{j,\sigma}$) create (annihilate) a hole with spin σ in the Cu $d_{x^2-y^2}$ and O $p_{x,y}$ orbitals, respectively. The $n^d_{i,\sigma} = d^\dagger_{i,\sigma} d_{i,\sigma}$ and $n^p_{j,\sigma} = p^\dagger_{j,\sigma} p_{j,\sigma}$ are the hole number operators. The Cu onsite energy is given by ϵ_d, and the oxygen onsite energy by ϵ_p, and $\Delta = \epsilon_p - \epsilon_d$ is positive in hole notation. U_{pd} takes the intersite Coulomb interaction into account, and U_d (U_p) counts the double occupancy on Cu (O) orbitals. In this picture, the

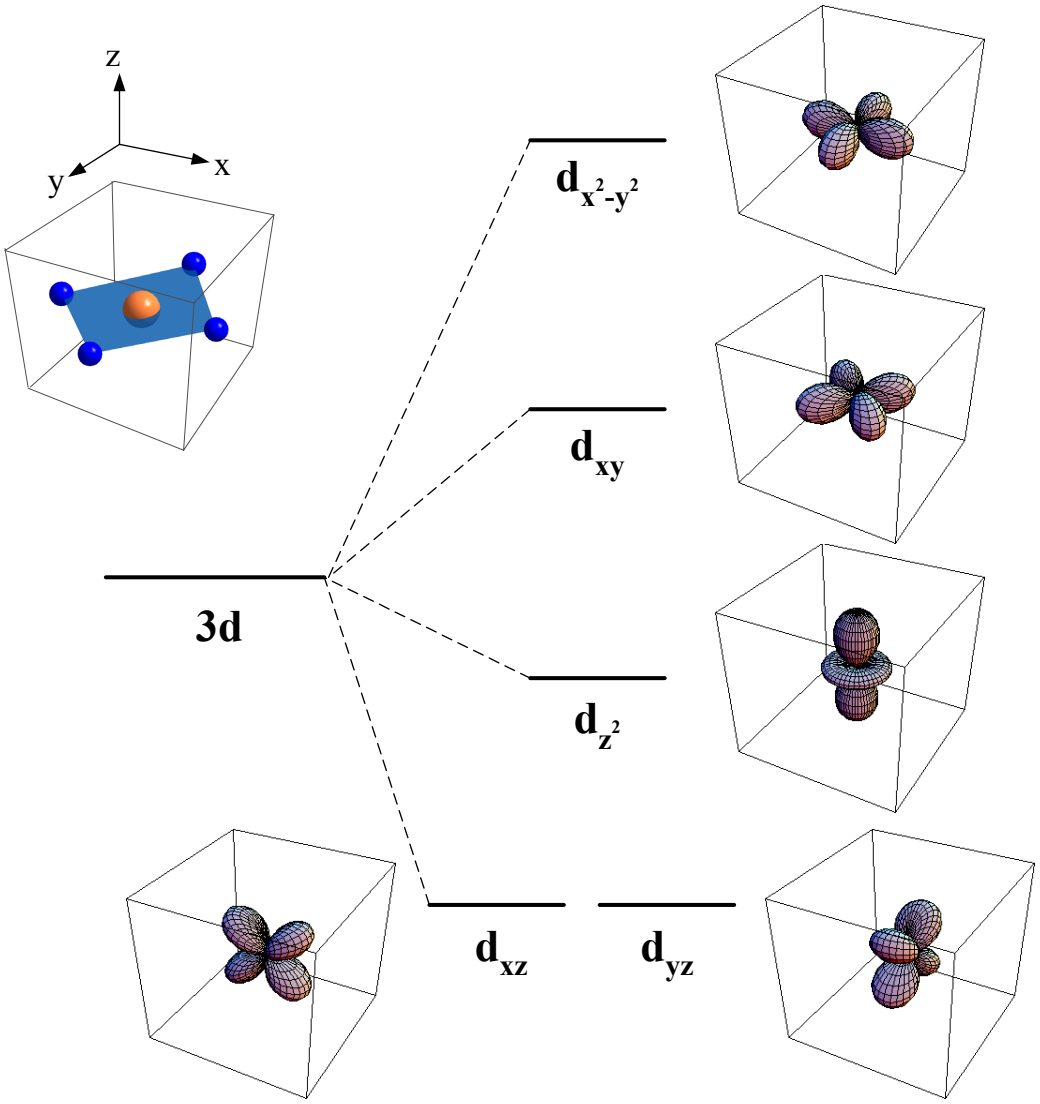

Figure 2.4: Schematic picture of the crystal-field splitting in copper-oxide systems with Cu^{2+} square-planar geometry leading to a half-filled $d_{x^2-y^2}$ orbital .

exchange interaction J_{Cu-Cu} between Cu sites is mediated via the oxygen orbitals and therefore becomes a *super*exchange constant [42]. The case of hole doping of a CT insulator was investigated by Zhang and Rice in 1988 [43]. The so-called Zhang-Rice singlet state (ZRS) [43] was introduced, in which the hole doped into the O orbitals forms a singlet with the hole on a Cu site, as depicted in Fig. 2.6. In La_2CuO_4 and other corner-sharing two-dimensional members of the high-T_C family, the ZRS can propagate to neighboring CuO_4 plaquettes along the Cu-O bond direction and along the diagonal [43–46]. In the copper-oxide compounds,

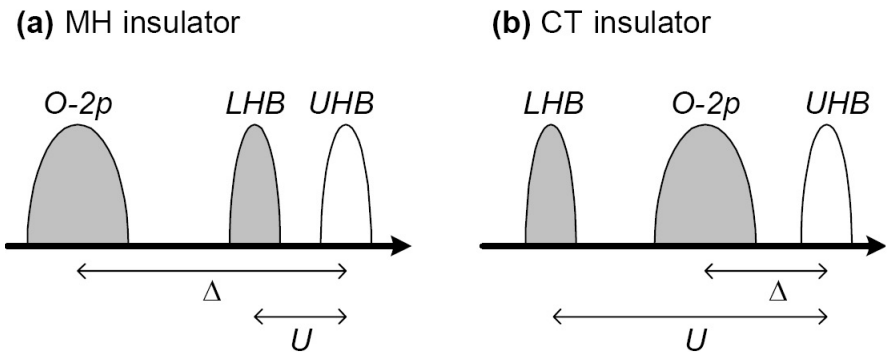

Figure 2.5: Schematic representation of the level splitting into a lower Hubbard band (LHB) and an upper Hubbard band (UHB), separated by the Coulomb repulsion U in case of (a) a Mott-Hubbard (MH) insulator and (b) a charge-transfer (CT) insulator.

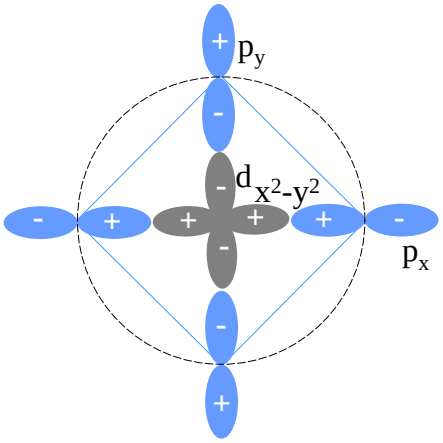

Figure 2.6:
Schematic description of a Zhang-Rice singlet with Cu-O hybridization between Cu $3d_{x^2-y^2}$ and O $2p_{x,y}$ orbitals. A hole is doped into the surrounding oxygen atoms (O $2p^5$) and forms a spin singlet with the hole on the Cu site ($3d^9$). The + and - signs denote the phase of the wave function.

the CT gap lies in an energy range of the order of 1.5 - 2.0 eV showing variations in gap size and line shape of the optical conductivity with oxygen coordination and dimensionality as shown in Fig. 2.7 [47, 48]. Extensive experimental and theoretical work has been done to understand the character of electron-hole excitations in insulating parent compounds as well as in the hole-doped cuprates but the precise nature of these excitations is still controversial. A short summary is given in the following section with focus on the low-energy excitation spectrum which is believed to be of fundamental importance for the physics of high-T_C compounds.

The common optical techniques to investigate the excitations of correlated electrons are optical reflectance measurements followed by a Kramers-Kronig transformation, ellipsometry, and Raman spectroscopy. The dependence of dipole-allowed and dipole-forbidden excitations on the momentum **k** is studied by angle-resolved electron energy loss spectroscopy (EELS). Single-particle excitations of occupied states are probed by angle-resolved photoemission (ARPES); x-ray ab-

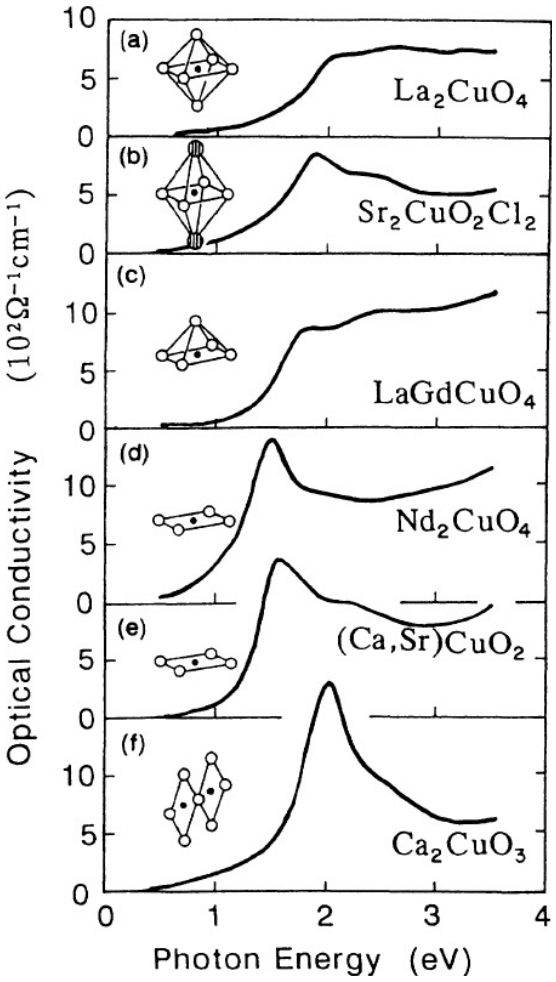

Figure 2.7:
Optical conductivity spectra for 1D and 2D cuprates with changing Cu-O networks [47]. The optical conductivity was derived by a Kramers-Kronig transformation on reflectance data. The reflectance was measured on the (001) surface with polarization of the electrical field parallel to the Cu-O basal planes.

sorption spectroscopy (XAS) investigates the unoccupied states, and more recently momentum-resolved resonant inelastic x-ray scattering (RIXS) is used to investigate momentum-dependent excitations into unoccupied states. Due to immense progress especially in this technique (higher resolution), new data and new insights on some already investigated compounds such as La_2CuO_4 are available today. As a consequence, some interpretations may have to be revised.

2.4.1 Excitons and excitonic resonances

The spectrum of the charge-transfer excitations in 2D cuprates above the gap shows a prominent peak near the band edge (see Fig. 2.7), and despite many theoretical and experimental investigations it is still discussed if this represents an excitonic resonance or not. What this means and why this question is difficult to answer will be described in this section.

In an optical absorption process in conventional band insulators, photons can

excite an electron from the valence band into the conduction band, leaving behind a hole in the valence band. The effect of electron-electron interaction, i.e. the Coulomb interaction between the excited electron in the conduction band and those left behind in the almost filled valence band is described in a picture of electron-hole interaction. The resulting attraction between electron and hole can cause their motion to be correlated. Such a bound electron-hole pair is called exciton. Two cases can be distinguished. In one, the electron-hole attraction is strong and the excitons are bound tightly together, i.e. the exciton radius is comparable to the size of a unit cell. These so-called Frenkel excitons often exist in ionic crystals. However, if the Coulomb interaction is strongly screened by the valence electrons, the electron-hole pair is only weakly bound. In that case, the radius of the exciton is much larger than the lattice spacing and the binding energy is small. These bound states are called Wannier-Mott excitons. Excitons can be identified as absorption peaks in the optical conductivity just below the band gap (see Fig. 2.8) At the same time, excitonic effects can drastically change the shape of absorption edges and the line shape in the continuum above the gap in optical spectra. While a true excitonic bound state is found as a sharp peak below the onset of the optical gap, a so-called excitonic resonance is represented by a prominent peak found within the continuum of states above the gap. An excitonic resonance is sometimes called scattering state of electron-hole pairs. In other words, the bound states of the electron-hole pairs have much shorter lifetime.

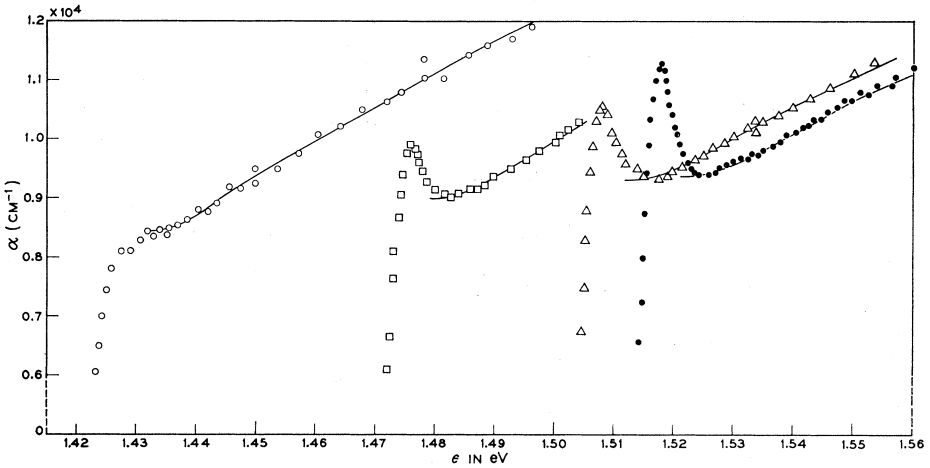

FIG 3 Exciton absorption in GaAs; ○ 294°K, □ 186°K, △90°K, ● 21°K.

Figure 2.8: Optical absorption coefficient of GaAs [49] from 1.41 to 1,56 eV for 4 different temperatures showing sharp peaks at the fundamental absorption edge due to the formation of excitons. With increasing temperature, the band edge shifts and the exciton peak broadens

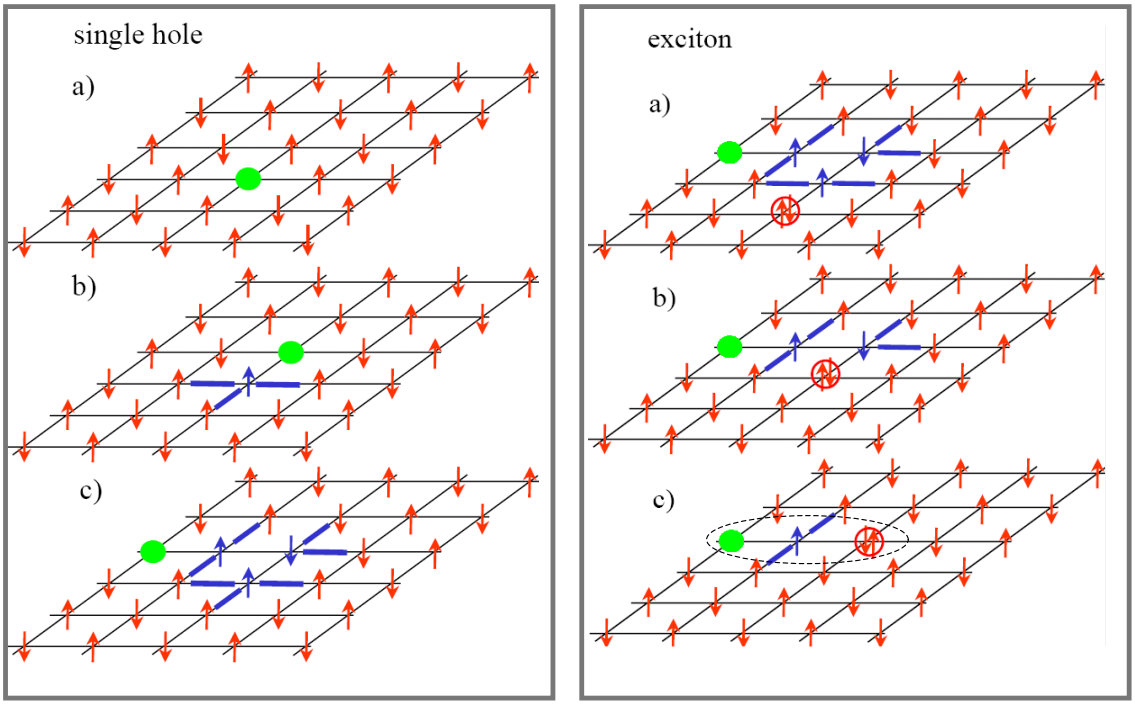

Figure 2.9: Left panel: Simplified picture of the movement of a single hole (green dot) in a 2D AF Mott-Hubbard insulator. Cu spins are represented by red arrows, and the blue bars represent unfavorable bonds where the AF order is destroyed and leading to an increase in energy. The order can be restored by a spin wave. Right panel: A hole followed by a doubly occupied site (red circle) which restores the AF order. Coherent motion of double and empty site gives rise to a gain in kinetic energy. A very similar pairing mechanism is also discussed as a possible mechanism for Cooper-pair formation in high-T_C superconductors [50–53].

Excitons in Mott-Hubbard insulators

In Mott-Hubbard insulators the lowest optical interband transition creates an empty site and a doubly occupied site, i.e., a hole in the LHB and a particle in the UHB. In this picture, an exciton can be regarded as a bound state of an empty site (hole) and a doubly occupied site (double), moving in a background of singly occupied sites. While in the above described conventional band insulators, the creation of an electron-hole pair is driven by a reduction in Coulomb energy, theoretical studies of excitons in 1D and 2D Mott-Hubbard systems have shown that the exciton binding can either be driven by a gain in Coulomb *or* kinetic energy.

In 2D, strong magnetic interaction was found to be the origin of the exciton

binding energy in contrast to the conventional mechanism via long-range Coulomb interaction [50, 54–64]. This means the gain in *kinetic* energy rules the exciton

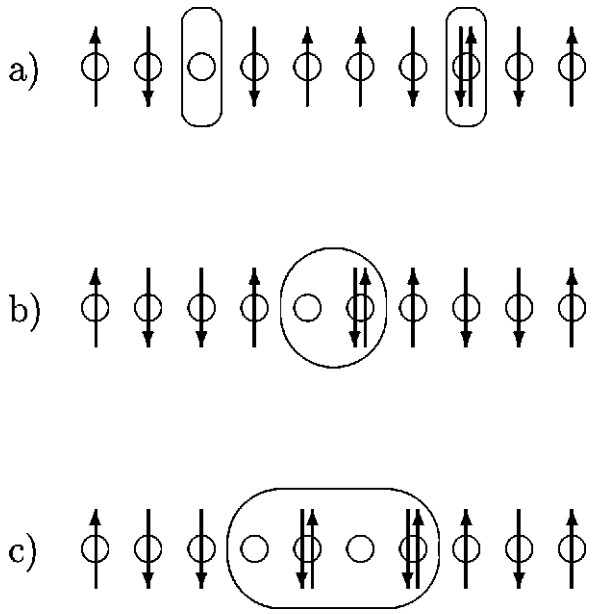

Figure 2.10: Possible electron-hole excitations in 1D Mott insulators at half filling and in the limit of a large Mott gap ($U \gg t$). Elementary charge excitations are represented by moving one electron from one site to another, creating an empty site and a doubly occupied site. Depending on the size of V, the following excitations are created: (a) an unbound holon-doublon pair (see explanation in text); (b) a bound pair (exciton), or (c) a biexciton in the strong coupling limit $U - 2V \gg t$ [65].

binding. In this picture, hopping processes are suppressed for well separated single holes or single doubles because of the AF (short-range) order. However, if a hole and a double form a singlet, then the hopping of this singlet is not suppressed by the magnetic background, giving rise to an effective gain of kinetic energy (see Fig. 2.9).

In many theoretical studies it has been found that in 1D Mott-Hubbard insulators the Coulomb-driven exciton binding is dominant [23, 65–72]. Here, the extended Hubbard model at half filling is used to describe excitons. It takes into account the intersite repulsion V between electrons on neighboring transition-metal sites [66, 68]. It turns out that excitons are only formed below the gap if V exceeds a critical value [66, 69]. As mentioned before, in Wannier-Mott theory of conventional band insulators, the exciton formation is ruled by Coulomb attraction. Properties as size, binding energy, etc. exhibit a monotonic dependence on the strength of the Coulomb repulsion. Excitons in 1D Mott-Hubbard insulators

however, show a much more complex nature since in a Mott-Hubbard insulator the Coulomb interaction determines at the same time the size of the Mott gap, the exciton properties, and the coupling of the exciton to the other electrons in the system. In particular, the binding energy of a Mott-Hubbard exciton does not give a good estimate of the Coulomb interaction strength [65, 69]. The one-dimensional

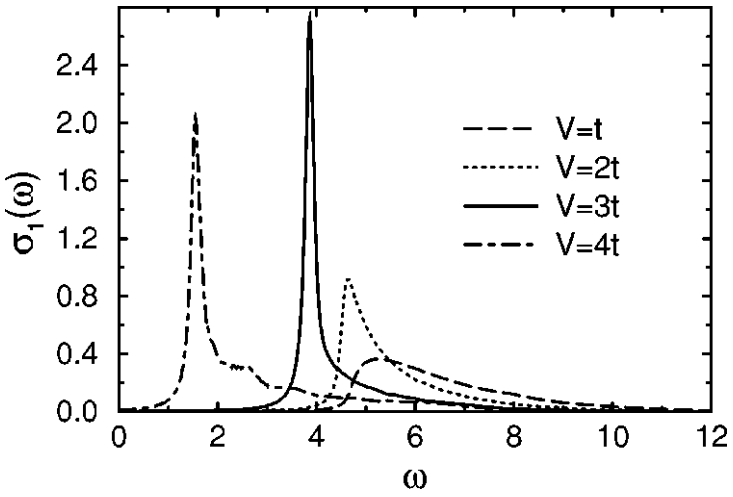

Figure 2.11: Optical conductivity $\sigma_1(\omega)$ in a one-dimensional Mott chain in the regime of finite Mott gap ($U = 8t$) for four different values of V_1 (nearest-neighbor repulsion) calculated with DDMRG (N=128 sites) [65]. The energy state is given in units of t. The next-nearest neighbor repulsion V_2 is set to zero. Several excitations are found in the low-energy spectrum for different regions of parameter space (U,V). In 1D the band width is given by $W = 4t$. For $U = 8t$ and $V = 0$, one expects that the LHB-UHB excitation peaks at $8t$, and the band gap is located a $U - W = 4t$. At $V = t$ and $V = 2t$ the spectrum shows one continuous band belonging to free charge-carrier excitations above the optical gap (dashed and dotted lines). In comparison to $V = 0$, a finite V pulls down the spectral weight to lower frequencies forming an excitonic resonance. However, a true bound state is only found for $V > 2t$. For $V = 3t$ a strong peak corresponding to an exciton below the Mott gap and a continuous band above the Mott gap are observed. The exciton takes a large part of the spectral weight. For $V = 4t$, CDW droplets below the gap dominate the spectrum [65].

extended Hubbard Hamiltonian is given by [24]

$$\begin{aligned} H = -t \sum_{l;\sigma} (\hat{c}^{\dagger}_{l,\sigma} \hat{c}_{l+1,\sigma} + \hat{c}^{\dagger}_{l+1,\sigma} \hat{c}_{l,\sigma}) \\ + U \sum_{l} (\hat{n}_{l,\uparrow} - \frac{1}{2})(\hat{n}_{l,\downarrow} - \frac{1}{2}) \\ + V_1 \sum_{l} (\hat{n}_{l} - 1)(\hat{n}_{l+1} - 1) \\ + V_2 \sum_{l} (\hat{n}_{l} - 1)(\hat{n}_{l+2} - 1) \end{aligned}$$

It describes electrons with spin $\sigma = \uparrow, \downarrow$ that can hop between neighboring sites. $\hat{c}^{\dagger}_{l,\sigma}$ and $\hat{c}_{l,\sigma}$ are creation and annihilation operators for electrons with spin σ at site l. $\hat{n}_{l,\sigma} = \hat{c}^{\dagger}_{l,\sigma} \hat{c}_{l,\sigma}$ are the number operators, and $\hat{n}_l = \hat{n}_{l,\uparrow} + \hat{n}_{l,\downarrow}$. Here, t is the hopping amplitude, U the onsite Coulomb interaction, and V_1 nearest and V_2 next-nearest-neighbor repulsion. Essler *et al.* [69] use dynamical density-matrix renormalization group (DDMRG) calculations and a field-theoretical approach on the basis of the one-dimensional extended Hubbard model to calculate the optical conductivity in the limit of large Mott gap ($U \gg t, V_1, V_2$) to small Mott gap ($t \gg U, V_1, V_2$). In the limit of small Mott gap, the Hamiltonian shows spin-charge separation [69]. In this case the system shows collective excitations of decoupled charge and spin degrees of freedom [73] called holons (charge e^+ and no spin) and spinons (no charge, spin = 1/2), respectively. The phenomenon is known in one-dimensional metals, where the low-energy excitations are described in the frame of the so-called Tomonaga-Luttinger liquid model [74, 75]. In the small gap limit of 1D Mott insulators the doubly occupied site and hole become antiholons and holons, respectively (spinless excitations of opposite charge) which in certain parameter regimes can build bound pairs [69]. Figure 2.11 shows $\sigma_1(\omega)$ for intermediate Mott gap ($U = 8t$) in the parameter regime $V_2 = 0$ and $t \leq V_1 \leq 4t$ [65].

2.5 Experimental overview

Next, an overview on the experimental an theoretical findings on the electron-hole excitations in 2D and 1D cuprates is given. We start with the 2D compound $Sr_2CuO_2Cl_2$ which is maybe the most ideal realization of a 2D antiferromagnetic (AF) Mott insulator.

2.5.1 Excitations in 2D copper oxide planes

$Sr_2CuO_2Cl_2$ is isostructural to La_2CuO_4. However, the apex Cl ions have a larger distance to the copper-oxide planes and hence a reduced influence on their excitation spectrum. We discuss results of EELS and optical spectroscopy on the 2D compound in order to understand the nature of the lowest-lying electron-hole excitations.

The ZN model

In 1998, Zhang and Ng [56] developed a local model to explain the excitation spectrum in the 2D compound $Sr_2CuO_2Cl_2$ measured by EELS [55]. The spectrum showed an optically allowed excitation at 2.8 eV in the [110] direction for $\mathbf{k} = 0$ with large dispersion[2] of ~ 1.5 eV.

The model of Zhang and Ng delivers four exciton modes corresponding to $d-, s-$, and $p_{x,y}$-wave symmetry, where the lowest excitation is represented by the d-wave mode. It is described by an empty site (or, regarding electrons, a doubly occupied site, namely Cu^+) and a Zhang-Rice singlet state on a neighboring site as depicted in Fig. 2.12 [56]. This bound pair (empty site - double) is often referred to as ZN exciton. This spin-singlet electron-hole pair may move freely through the 2D lattice without disturbing the spin background as depicted in Fig. 2.9, explaining the large dispersion in EELS.[3]

However, the strong dispersion of the ZN exciton has been questioned recently on the basis of high-resolution EELS data [60, 76–78] and RIXS investigations on La_2CuO_4 which show the same excitation in the copper-oxide planes but much smaller dispersion (0.3-0.5 eV) [63, 64]. In addition, the high-resolution EELS measurements and RIXS data show a multi peak structure of the spectrum in both compounds. The data reveal a new feature at 2.2 eV and $\mathbf{k}$=0 that was not resolved before and does not show a dependence on momentum transfer. The excitation at 2.6 eV that was already reported by Wang *et al.*(ZN-exciton) is observed too. Then evidence was found for more dispersionless narrow bands at higher energies near 4.2, 5.4, and 7.2 eV that cannot be explained by the simple ZN model.

Cluster model

Moskvin *et.al.* [60, 71, 78] have generalized the ZN model into a new cluster theory to explain the multi-peak structure in EELS data of $Sr_2CuO_2Cl_2$ [76] and also explaining excitations in the 1D corner-sharing chain Sr_2CuO_3 [71, 78].

[2] This means the excitation shifts to higher energy with rising momentum transfer.

[3] In conventional semiconductors, EELS can probe excitations of the electron-hole continuum as well as the excitonic spectrum. The latter lies below the electron-hole continuum and its bandwidth is *narrower* than that of an electron or hole, respectively.

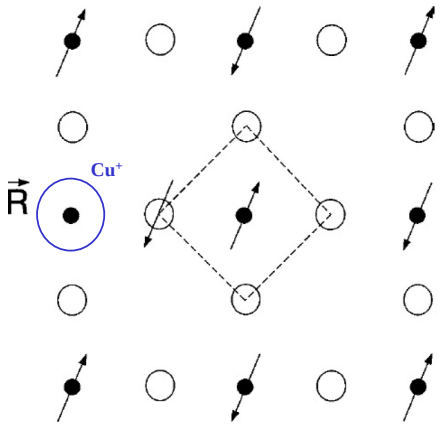

Figure 2.12: Schematic description of an exciton in a CuO_2 plane (ZN-exciton)[55]. The open circles represent oxygen ions (O) and the solid circles represent copper ions (Cu). The arrows represent spins of the holes. The quasiparticle is at site $\vec{R}$ (Cu^+) and the quasihole is located on the neighboring square of O atoms and forms a spin singlet with the central Cu hole (Zhang-Rice singlet).

In their approach, two new aspects are introduced. First, they do not only consider O2p_σ orbitals but O2p_π and O2p_z orbitals as well, and second, they argue that the O-Cu charge-transfer process generates two types of excitons (see figure 2.14): one-center excitons (OCE) on one CuO_4 plaquette, and two-center excitons (TCE) extending over two plaquettes [60, 71, 78][4].

In their local picture, two neighboring CuO_4 plaquettes, embedded into the insulating cuprate, are considered. Beginning from 5 Cu 3d and 12 O 2p atomic orbitals for a CuO_4 cluster with D_{4h} symmetry, 17 symmetrized even ($a_{1g}, a_{2g}, b_{1g}, b_{2g}, e_g$) or odd ($a_{2u}, b_{2u}, e_u(\sigma), e_u(\pi)$) orbitals are constructed. The even Cu 3d orbitals $a_{1g}(3d_{z^2}), b_{1g}(3d_{x^2-y^2}), b_{2g}(3d_{xy})$, and $e_g(3d_{xz}, 3d_{yz})$ hybridize with even combinations of O 2p orbitals of the same symmetry, forming bonding γ^b and antibonding γ^a states. Among the odd orbitals, only $e_u(\sigma)$ and $e_u(\pi)$ hybridize, forming bonding e_u^b and antibonding e_u^a oxygen states. The oxygen orbitals a_{2g}, a_{2u}, and b_{2u} are nonbonding states. The model predicts a large number of excitons or excitonic resonances at the Γ-point ($\mathbf{k}$=0).

The two lowest dipole-allowed excitations are a one-center exciton ($b_{1g} \rightarrow e_u(\pi)$) and the two-center exciton with a Zhang-Rice singlet as final state (ZN exciton, $b_{1g} \rightarrow b_{1g}$) as depicted in Fig. 2.14.

Moskvin *et al.* interpret the seemingly large dispersion of the ZN exciton (at

[4]It should be noted that in optical spectroscopy, fixed to the $\mathbf{k}$= 0 region, it is in principle not possible to distinguish between one-center (dispersionless) and two-center excitons with a noticeable dispersion.

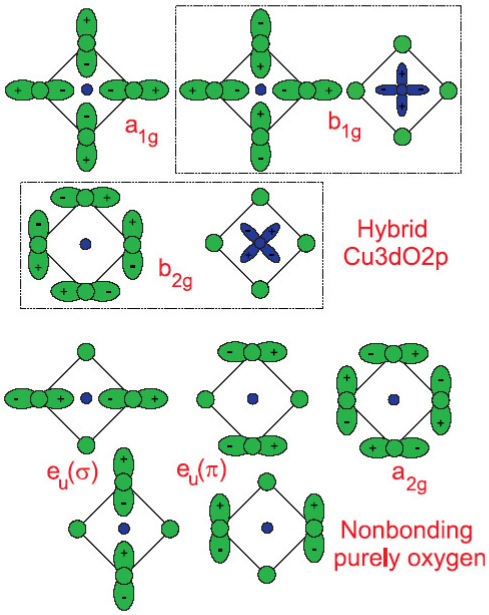

Figure 2.13: Electron (hole) density distribution for planar copper and oxygen molecular orbitals on one CuO_4 plaquette [71]

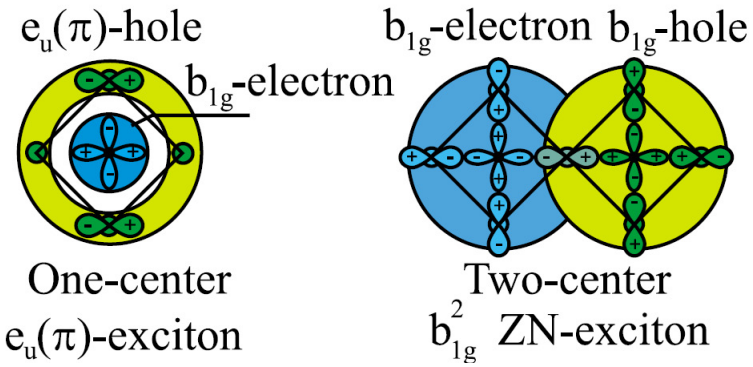

Figure 2.14: Left panel: example of a one-center exciton formed by an electron in the Cu $3d_{x^2-y^2}$ hybridized state (even symmetry b_{1g}) and a hole in the purely oxygen hybridized states (odd symmetry $e_u(\pi)$). Right panel: The two-center exciton corresponding to the ZN exciton between a b_{1g} electron and a b_{1g} hole. The b_{1g} hole is a Zhang-Rice singlet.

2.6 eV) in the EELS spectra of $Sr_2CuO_2Cl_2$ [55, 76, 77] in terms of an exciton-exciton interaction. It is argued that the dipole-allowed exciton vanishes with rising momentum transfer while the intensity of a dipole-forbidden exciton at 3.8 eV near the BZ boundary rises. They propose that this effect might be misin-

terpreted in terms of a large dispersion of one peak. It is stressed by the authors that the model prediction for the OCE absorption spectrum for one CuO_4 plaquette shows an interplay of forbidden $d-d$ transitions ($b_{1g} \rightarrow b_{2g}, a_{1g}, e_g$) and forbidden ($b_{1g} \rightarrow a_{2g}$) as well as allowed ($b_{1g} \rightarrow e_u(\pi)$) CT transitions which are close in energy. Moskvin *et al.* point out that a separation of optical transitions into crystal-field $d-d$ and CT $d-p$ transitions is questionable in the cuprates or other strongly covalent systems since the forbidden $d-d$ transitions are accompanied by a strong $p-d$ and $p-p$ charge transfer.

The ($b_{1g} \rightarrow e_u(\pi)$) exciton is expected to be small with large effective mass due to coupling to the lattice.[5] It is emphasized that this cluster model cannot prove whether the low-lying particle-hole pairs are bound (lying below the gap) or not (forming resonances within the continuum), i.e. the question of lifetime is not answered. Thus, in this model all electron-hole excitations are called excitons. Moskvin *et al.* stress that a peak assignment in 2D is very difficult due to the superposition of OCEs and TCEs. [6]

Choi *et al.* [81] have measured the transmittance and reflectance of $Sr_2CuO_2Cl_2$ near the gap as a function of temperature (293 - 523 K) and identified three major excitations which show different behavior with rising temperature (see Fig. 2.15). This can give insight into the nature of the electron-hole excitations. In general, one expects a slight shift of the excitations to lower energy with increasing temperature due to lattice expansion. In the cuprates, the Cu-O distance will change and correspondingly the band energies since crystal-field splitting and Madelung potentials change with Cu-O distance. In addition to that, spin-ordering, electron-phonon or electron-electron interaction are temperature dependent and may influence the gap energy. The observed peaks (see Fig.2.15) assigned in the following way [81]: small peak at 1.4 eV which is only observed in transmittance measurements (see Fig.2.15 (c)) is assigned to a local $d-d$ transition, i.e., a crystal-field excitation. Since this excitation is not dipole-allowed it is very weak in intensity. Peak **B** (see Fig. 2.15 (b)) at 2.0 eV is assigned to the ZN-exciton and **C** at 2.6 eV is identified with an excitation from non bonding oxygen bands NBB to the UHB. This interpretation is in contradiction to the interpretation of Wang *et al.*[55], Zhang and Ng[56] and Moskvin *et al.*[78] where the excitation at 2.6 eV **C** is assigned to the ZN-exciton.

Choi *et al.* support their assignment with the temperature dependence of the peaks. While peak **B** shows a strong redshift (- 121 meV) within the measured temperature range, peak **C** does not shift as much in energy (-59 meV). It is argued [81] that the strong shift of **B** is not only due to lattice expansion but also due to a change in the AF spin ordering. They propose that the excitation **B** is

[5] The $e_u(\pi)$ and $e_u(\sigma)$ excitations are doubly degenerate leading to a strong electron-lattice coupling and self trapping [78].

[6] Additional information by ARPES data [79, 80] was used for interpretation of EELS data at the Γ-point.

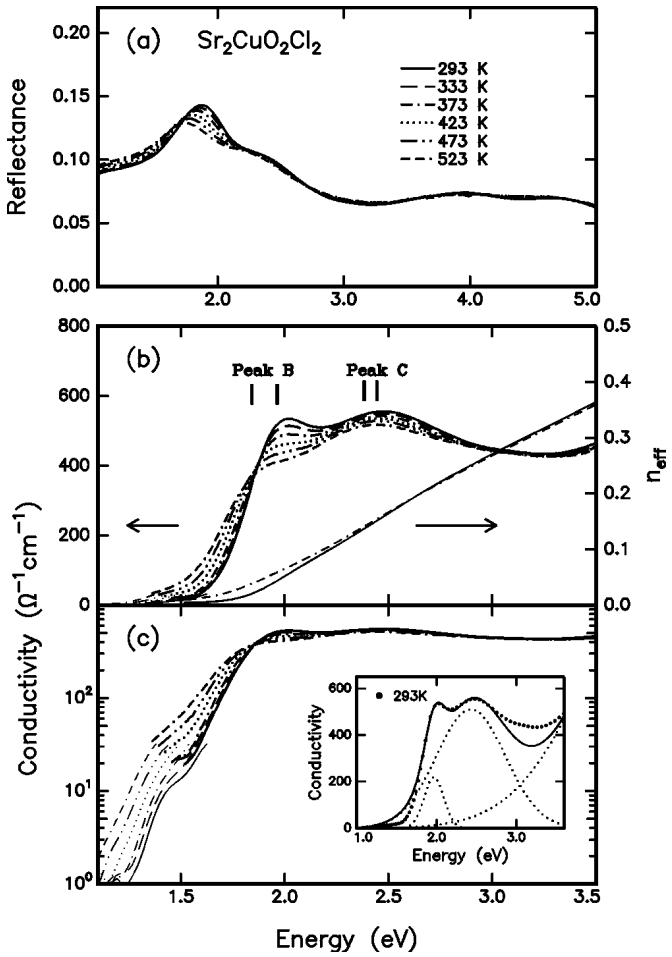

Figure 2.15:
Temperature dependence of reflectance data of $Sr_2CuO_2Cl_2$ (a). Panel (b) shows optical conductivity data from reflectance measurements followed by Kramers-Kronig transformation [81]. c) shows optical conductivity data on a logarithmic scale to compare with optical conductivity derived from transmittance measurements. Three peaks are identified. Peak A (around 1,4 eV) which is very weak in intensity and only observed in transmittance measurements is assigned to an intra-atomic (one-center) dipole-forbidden $d-d$-excitation $Cu3d_{x^2-y^2} \rightarrow 3d_{xy}$. Peak B (at 2,0 eV) is assigned to the charge transfer from $O_{2p} \rightarrow$ Cu $3d$ forming a Zhang-Rice singlet. Peak C (2,5 eV) is assigned to the excitation from a nonbonding oxygen band to Cu $3d$. Peak B shows a strong redshift with rising temperature.

more affected by spin order since the hole in the oxygen orbitals of the Zhang-Rice band is strongly coupled to the Cu spins due to the strong hybridization. It is proposed that the weakening of the AF order leads to a shift of the ZRS to the UHB [81]. The nonbonding oxygen bands of peak **C** do not hybridize strongly with the Cu orbitals and thus are not much affected by spin ordering. Its temperature dependence is explained by the expected lattice expansion [81].

Falck *et al.* [82] have measured the temperature dependence of the reflectance spectrum of La_2CuO_4 in the range between 0.5 and 3.1 eV and calculated ε_2 by Kramers-Kronig transformation. The spectra show the same excitations as those in $Sr_2CuO_2Cl_2$ [81]. Falck *et al.* also identify the first weak excitation at 1.75 eV with a crystal-field excitation. This is supported by photoconductivity measurements that do not show a photocurrent in this energy range. The peak at 2.0 eV is classified as charge-transfer excitation without giving more details. Here, a photocurrent is detected (i.e. free electrons and holes are created).

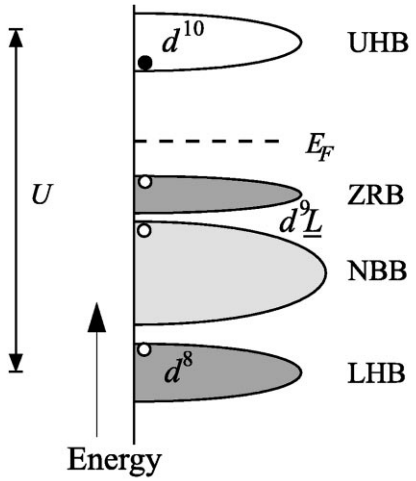

Figure 2.16: Schematic description of the density of states (or better: photoemission and inverse photoemission spectra) in a Mott-Hubbard insulator including nonbonding oxygen bands. In this picture, the in-plane Cu-O hybridization is considered between Cu $3d_{x^2-y^2}$ orbitals and O $2p_\sigma$ forming Zhang-Rice bands (ZRB). The nonbonding bands (NBB) with predominantly oxygen character and small overlap with Cu orbitals are situated below the ZRB [81], i.e. an excitation to the UHB lies higher in energy than from the ZRB.

The temperature dependence of the spectrum of the 2D planes in La_2CuO_4 has also been observed by Ellis *et al.* [64] in RIXS measurements. They confirm a low-energy excitation at 1.8 eV also assigned to a local $d-d$ transition and an excitation at 2.2 eV which is identified with the ZN exciton [56] (showing small dispersion). The edge of the CT excitation shifts to lower energy with increased temperature as also reported by Falck *et al.*[82] This shift with temperature is interpreted in terms of strong electron-phonon coupling by Ellis *et al.*[64]. The coupling to phonons in this picture also explains the small exciton dispersion since the effective mass of the excitations is enhanced [64].

2.5.2 1D corner-sharing and edge-sharing chains

In 1D, the one-center excitations can be separated in EELS by choosing a momentum transfer perpendicular to the chain direction because in polarization perpendicular to the chains only one-center excitations (OCE) are expected. Therefore, Moskvin *et al.* investigated the electronic excitations of the 1D corner-sharing compound Sr_2CuO_3 in both polarization directions to confirm their model predictions. Figure 2.17 shows momentum-resolved EELS data of Sr_2CuO_3 [71, 78].

In the spectrum with **k** perpendicular to the chain (right panel in Fig. 2.17) one dispersionless peak at around 2.0 eV and another dispersionless peak at 5.5 eV are visible. Moskvin *et al.* associate them with the dipole allowed one-center charge-transfer excitations (OCE) $e_u(\pi)$ and $e_u(\sigma)$, respectively. In the response with **k**

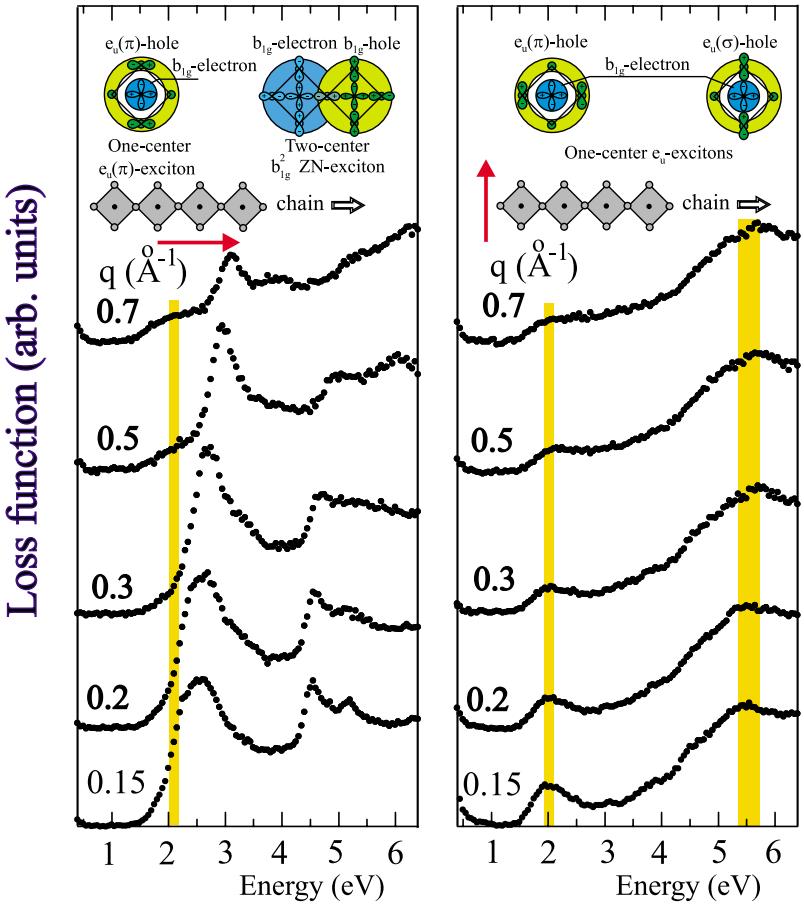

Figure 2.17: *k*-resolved EELS spectra of the 1D corner-sharing chain Sr_2CuO_3 for **k**∥ chain(left panel) and **k**⊥ chain (right panel) [71, 78]. The measurement was carried out in two directions to identify one-center (OCE) and two-center excitons (TCE).

parallel to the chains (left panel in Fig.2.17), the dispersionless OCE at 2.0 eV is observed, too but less pronounced since it is sitting on the tail of a strong excitation around 2.5 eV. This second excitation at 2.5 eV shows a clear dependence on **k** and is therefore associated with the two-center ZN exciton [71]. The overall assignment is very similar to the 2D case.

Next, the experimental observations in the 1D edge-sharing chains are reported, starting with Li_2CuO_2 (see Fig. 2.3). Mizuno *et al.* have calculated the optical

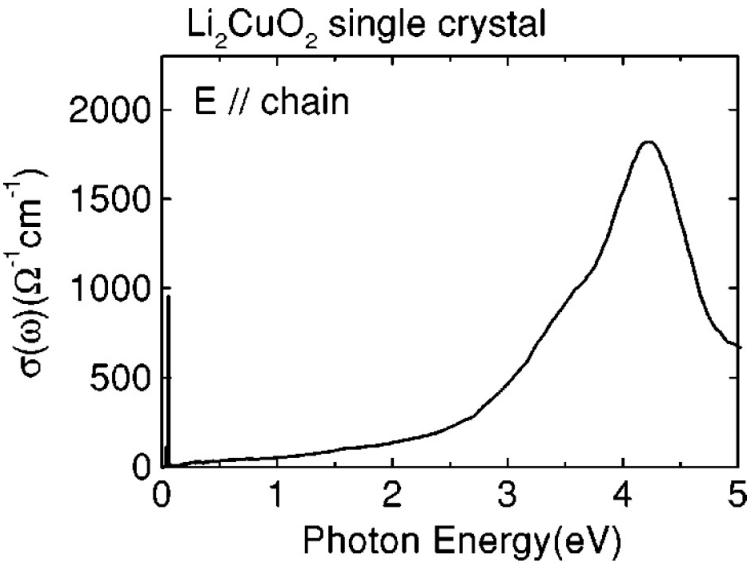

Figure 2.18: Optical conductivity $\sigma(\omega)$ along b axis (chain direction) of Li_2CuO_2 from reflectance measurements between 0.01 - 40 eV at near normal incidence and Kramers-Kronig transformation by Mizuno *et al.* [83]. The excitation spectrum shows one main absorption around 4 eV and *not* the ZN-excitation expected in theory [83] at 2.2 eV.

conductivity $\sigma(\omega)$ for polarization along the chain direction using the three-band Hubbard model [83] for Li_2CuO_2, the chain part in $La_6Ca_8Cu_{24}O_{41}$ and $CuGeO_3$. The calculations were compared with optical conductivity data of Li_2CuO_2, shown in Fig. 2.18 (E ∥ chains). The main excitation is observed around 4 eV and is assigned to a one-center excitation from O $2p$ non-bonding (NB) bands to the upper Hubbard. For $La_6Ca_8Cu_{24}O_{41}$ such an excitation is found at 4.0 eV and for $CuGeO_3$ at 5.0 eV. From theory another excitation around 2.2 eV is expected for all compounds [83] with much weaker intensity and which is ascribed to the ZN exciton. However, in the experimental optical conductivity spectra of Li_2CuO_2 this excitation is not observed [83]. The non-observation was explained with poor resolution or insensitivity of reflectance data to such weak features [83]. The peak was also not observed in EELS measurements [84]. Here, it should be noted that in the edge sharing chains charge carrier hopping is suppressed due to the 90° Cu-O-Cu bonds.

Magnetic ground state and optical conductivity

A recent theoretical study of Màlek *et al.* [85] addresses the temperature dependence $\sigma(\omega, T)$ and magnetic field dependence $\sigma(\omega, T, H)$ of the optical conductivity of Li_2CuO_2 in the range of low-energy electronic excitations. In this work, a sce-

nario is depicted where the observation of the peak is strongly correlated to the magnetic ground state. It could be suppressed at room temperature and might be observed at low temperatures depending on the GS. This discussion is included here because the authors encourage low-temperature measurements to verify their theory. The undoped parent compound of the spin ladders $Sr_6Ca_8Cu_{24}O_{41}$ is proposed as a candidate and since we investigated the quasi undoped compound $La_{5.2}Ca_{8.8}Cu_{24}O_{41}$) at low temperature in this thesis and will come back to this discussion in chapter5.

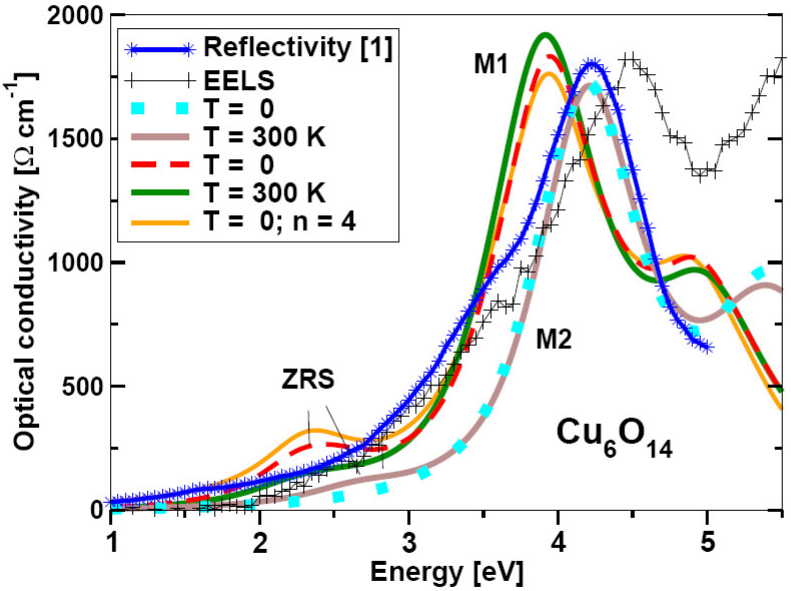

Figure 2.19: Calculated [85] and experimental [83] optical conductivity of Li_2CuO_2 for the two magnetic ground states M1 (AFM) and M2 (FM) at T=0 K and T=300 K for a Cu_6O_{14} cluster.

Málek *et al.* present two different scenarios depending on the magnetic ground state adopted. AFM ground state for M1 and FM ground state for M2. The T dependence is very different for M1 and M2. The calculated optical conductivity $\sigma(\omega)$ at T=0 K shows a multi-peak structure in both scenarios. Differences exist mainly between 2 and 4 eV. Here the result for different cluster sizes from 1 up to 6 edge-sharing CuO_4 plaquettes are shown. Already one unit shows a double-peak structure between 4 and 5.5 eV that which corresponds to one-center excitations from non-bonding O states to Cu-O hybridized states that of Mizuno *et al.* for Li_2CuO_4 [83]. This one-center excitation remain basically within that energy range for larger cluster sizes.

From $n = 2$ on, intersite transitions are possible. However, the final states depend on the ground state. The reason is that in optical spectroscopy the total

spin S and S_z are conserved. Therefore, for a GS with $S = 0$ (AFM), the lowest-lying excited state with S=0 corresponds to the Zhang-Rice singlet excitation (ZRS). This peak appears between 2 and 3 eV depending on cluster size. This transition is forbidden if the ground state is FM. In that case, the final state can be a Zhang-Rice triplet state (ZRT) which appears as a small shoulder below the strongest peak at 4 eV. For M1, the exact diagonalization provides $\omega_{ZRS} = 2.25\,\text{eV}$ and $\omega_{ZRT} = 3.7\,\text{eV}$, and for M2 $\omega_{ZRS} = 2.7\,\text{eV}$, $\omega_{ZRT} = 4\,\text{eV}$.

The temperature dependence of the optical conductivity $\sigma(\omega, T)$ for both models M1 (AFM) and M2 (FM) is shown in Fig. 2.19 in comparison with experimental 300 K data. In the FM ground state, the ZRS excitation is forbidden, however, at finite temperatures the spectral weight becomes finite due to magnetic fluctuations. In the AFM ground state it is allowed at T=0 but it loses weight with rising temperature. This means it is allowed for both cases at room temperature but due to its weak intensity it is not easy to resolve. Therefore, it is hardly possible to make a decision on the GS. At low temperatures, the ZRS excitation is not suppressed for the AFM state and expected at $\omega_{ZRS} = 2.25$.

2.5.3 1D spin ladders and spin chains

Now we turn to the spin-ladder system $(La,Sr,Ca)_{14}Cu_{24}O_{41}$ investigated within the scope of this thesis. The compounds show a mixture of electron-hole excitations of corner-sharing and edge-sharing 1D systems. It is obvious that with the difficulties already encountered in the pure 2D or 1D systems, it is not an easy task to identify the excitations and separate them into the subsystems. Another striking effect is the observed spectral-weight (SW) transfer by isovalent substitution of Sr by Ca. The spin-ladders have been investigated by means of optical spectroscopy by several groups [86–88]. We focus on the work of Osafune *et al.* who have carried out room temperature optical reflectance measurements on various samples with different Ca contents. Fig. 2.20 and 2.21 show room-temperature reflectance and optical conductivity data respectively along the ladder/chain direction by Osafune *et al.* [86]. They have investigated the spectral-weight transfer for different Ca contents by a sum-rule analysis and come to the conclusion that holes are redistributed from chains to ladders upon Ca substitution. The compound $Sr_{11}Y_3Cu_{24}O_{41}$ (doped with 3 holes per f.u.) and the compounds $Sr_{14-x}Ca_xCu_{24}O_{41}$, x = 0, 3, 6, and 11 (each compound doped with 6 holes) were investigated. The reflectance of $Sr_{11}Y_3Cu_{24}O_{41}$ shows insulating behavior and the compounds x = 0, 3, 6, and 11 show a metallic behavior mirrored by a plasma edge that shifts to higher energies with higher Ca content (see Fig. 2.20). To make a quantitative analysis on the SW transfer, the optical conductivity was calculated by Kramers-Kronig transformation of the reflectance data (see Fig. 2.21). Osafune *et al.* ascribe the low-energy excitations below 1.2 eV in the strongly hole-doped compounds to charge-carrier excitations in the ladders

because the holes are more itinerant there. The statement follows that the rise of the low-energy spectral weight with Ca substitution is a consequence of increased hole density by redistribution from chains to ladders and not a consequence of localized holes becoming more itinerant. The peak at 2.0 eV observed in all compounds is identified as a CT excitation between O2p and Cu3d orbitals. From the spectral-weight analysis Osafune *et al.* conclude that the spectral weight of the charge-transfer excitation at 2.0 eV is only transferred to the low-energy ladder excitations below 1.2 eV similar to the SW transfer into a 2D CT insulator upon hole doping [48, 89]. The strong peak above 2.5 eV is ascribed to an excitation in the chain subsystem where the holes are reported to remain localized. The intensity of this peak rises strongly from the CT insulator $Sr_{11}Y_3Cu_{24}O_{41}$ to $Sr_{14}Cu_{24}O_{41}$ (6 holes most of which probably in the chains) and then decreases again with x standing for a redistribution from chains to ladders. The SW analysis of Osafune *et al.* was carried out up to 2.5 eV with the argument that the spectral weight above 2.5 eV is not strongly dependent on x. As we will see later in our analysis, we find an alternative interpretation of the double peak structure above the gap and also find evidence for a spectral weight transfer to the energy region *above* 2.0 eV with Ca doping.

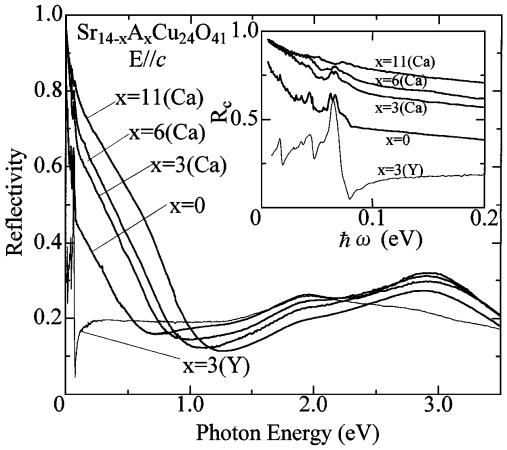

Figure 2.20: Room temperature reflectance data for different doping levels. The spectra show a plasma edge for x $\geq$ 0 and a shift in plasma edge to higher energy with rising x . The only insulating compound (no plasma edge at optical frequencies) is the reference compound $Sr_{11}Y_3Cu_{24}O_{41}$ (3 holes per f.u.) [86].

Mizuno *et al.* [90] have carried out cluster calculations in order to explain room-temperature data of Osafune *et al.* [86]. The exact diagonalization method was used to calculate excitations on Cu_6O_{17} clusters simulating the ladders and Cu_4O_{10} clusters representing edge-sharing chains. In compounds without holes

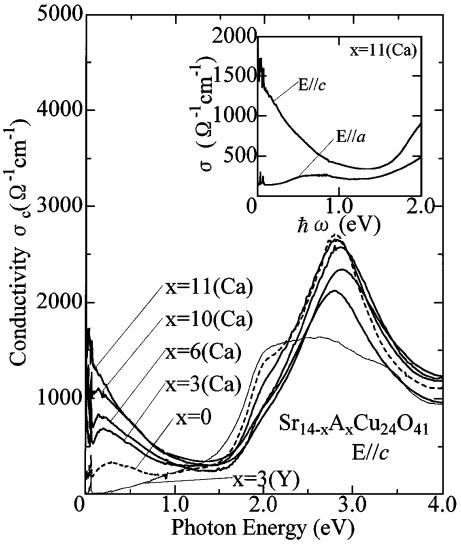

Figure 2.21: Room temperature optical conductivity data from reflectance measurements for different doping levels. The spectra show a shift of spectral weight with hole-doping and Ca-doping [86].

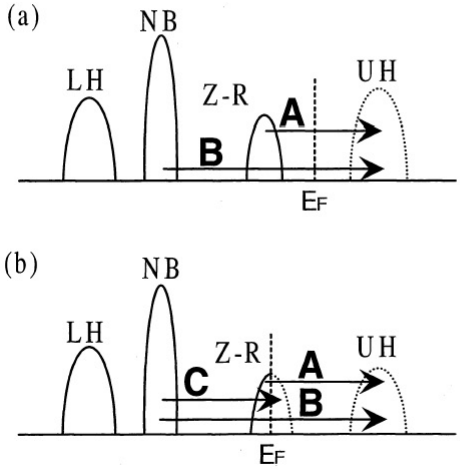

Figure 2.22: Schematic representation of charge-transfer type excitations in (a) undoped and (b) holed-doped spin ladders as discussed by Mizuno *et al.* [90].

two major optical interband excitations are expected in the ladder subunit as shown in Fig. 2.22 (a). One at 1.7 eV (A) is assigned to an excitation from one Zhang-Rice singlet (ZR) to the upper Hubbard band (UHB) (corresponding to the ZN exciton or $b_{1g} \rightarrow b_{1g}$) and the second around 4.5 eV (B) assigned to an

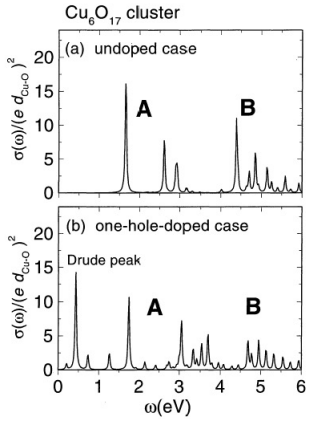

Figure 2.23: Results of cluster calculations for a undoped (a) and hole doped (b) *ladder* cluster by Mizuno *et al.* [90].

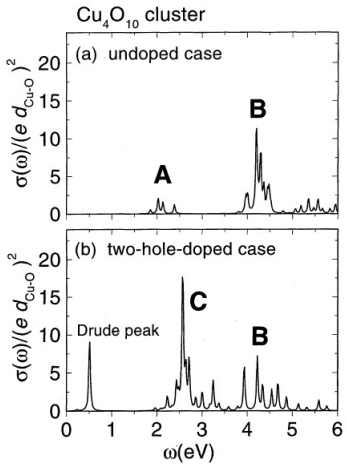

Figure 2.24: Results of cluster calculations for undoped (a) and two-hole doped (b) *chain* cluster calculation by Mizuno *et al.* [90].

excitation from non-bonding oxygen (NB) to the UHB. The two-center excitation or ZN exciton (A) is not expected in the chains due to 90° Cu-O-Cu bonds that make overlap small. In the hole-doped case, an additional Drude weight builds up in chains and ladders. In the **chains** a strong excitation C builds up that arises due to electron hopping from non-bonding oxygen to Zhang-Rice singlets (see Fig. 2.22 (b)).

2D planes	peak energy [eV]	assignment	character
$Sr_2CuO_2Cl_2$			
EELS	2.2	$b_{1g} \rightarrow e_u(\pi)$	OCE
[55, 60, 76, 77]	2.7	$b_{1g} \rightarrow b_{1g}$ (ZN-exciton)	TCE
	4.2	$b_{1g} \rightarrow e_u^b(\pi - character)$	TCE
	6.0	$b_{1g} \rightarrow e_u(\sigma)$	OCE
	7.1	$b_{1g} \rightarrow e_u^a(\sigma)$	TCE
optics	1.4	$d-d$ excitation	OCE
[81]	2.0	ZN exciton	TCE
	2.6	non-bonding O to UHB	OCE
La_2CuO_4			
optical spectroscopy	1.75	$d-d$ excitation	OCE
[82]	2.0	CT excitation	
RIXS	1.8	$d-d$ excitation	OCE
[64]	2.2	ZN exciton	TCE

Table 2.1: Experimentally observed peaks in $Sr_2CuO_2Cl_2$ and La_2CuO_4 and assignment due to model predictions [64, 71, 78, 81, 82]. The upper part summarizes EELS data followed by results of optical spectroscopy and RIXS. It is striking that the assignment of the lowest lying charge-transfer excitation is not unambiguous.

Summary

In this overview the electron-hole excitations in 1D and 2D compounds observed by different spectroscopic techniques are compared to help identify the peaks observed in our optical spectra.

All authors agree upon the identification of the excitation around 1.4-1.8 eV with a local $d-d$ or crystal-field excitation. When it comes to the lowest-lying charge-transfer excitation, there is a variation between three-band Hubbard model to cluster model. In the cluster model of Moskvin *et al.*[78] the lowest lying CT excitation (around 2.0 eV) is a one-center excitation as depicted in Fig. 2.14 (left side). The higher-lying excitation at 2.6 eV is assigned to the two-center excitation which corresponds to the ZN exciton and is in accordance with the interpretation of Zhang and Ng [56]. Choi *et al.*, Falck *et al.*, and Ellis *et al.*[64, 81, 82] identify the absorption at 2.0 eV with the ZN exciton and the one at 2.6 eV with a one-center excitation.

This point will be discussed in more detail in chapter 5 where the electron-hole excitations of the undoped spin-ladder compound $La_{5.2}Ca_{8.8}Cu_{24}O_{41}$ (LCO) with 0.2 holes per formula unit (f.u.) and the hole-doped compounds (6 holes per f.u.) $Sr_{14-x}Ca_xCu_{24}O_{41}$ with x = 0 (SCO) and x = 5, and 8 (SCCO) are investigated

along all three crystallographic directions. Here too, multipeak structures are found. Moreover, the excitations show a strong dependence on hole-doping, Ca doping and temperature.

1D chains	observed peaks [eV]	assignment	character
Sr_2CuO_3	**corner sharing**		
EELS	**k** $\perp$ to chains		
[78]	2.0	$b_{1g} \rightarrow e_u(\pi)$	OCE
	5.5	$b_{1g} \rightarrow e_u(\sigma)$	OCE
	k $\parallel$ to chains		
	2.0	$b_{1g} \rightarrow e_u(\pi)$	OCE
	2.5	$b_{1g} \rightarrow b_{1g}$ (ZN-exciton)	TCE
	4.2	$b_{1g} \rightarrow e_u^b(\pi - character)$	TCE
Li_2CuO_2	**edge sharing**		
optical spectroscopy	**E** $\parallel$ to chains		
[83]	4.0 (theory + exp.)	non-bonding O to UHB	OCE
[85]	4.0-4.5 eV (theory)	non-bonding to Cu-O hybridized [85]	OCE
$Sr_{14-x}Ca_xCu_{24}O_{41}$	**E** $\parallel$ to chains /legs		
optical spectroscopy			
[86]	2.0 eV	CT excitation (ladders)	
	2.5 eV	excitation in chains	
clusters[90]			
undoped ladders	1.7 eV	ZN exciton	TCE
	4.5 eV	non bonding O to UHB	OCE
hole doped ladders	1.7 eV	ZN exciton	
	4.5 eV	nonbonding O to UHB	OCE
undoped chains	4 - 4.5 eV	non-bonding O to UHB	
hole doped chains	2.5 eV	non-bonding O to ZRS	OCE
	4.5 eV	non-bonding O to UHB	OCE

Table 2.2: Summary of experimentally observed and theoretically predicted electron-hole excitations in Sr_2CuO_3 (corner-sharing chain) and Li_2CuO_2 edge-sharing chain), and the chain and ladders in LCO and SCCO. [64, 71, 78, 81–83, 86, 90].

3 Optical Spectroscopy

Optical spectroscopy is a powerful experimental technique of studying the electrodynamic response of correlated electron systems. The interaction of electromagnetic radiation with matter delivers information on optical constants in a frequency-region where elementary excitations and collective modes are located. The optical conductivity contains contributions of lattice vibrations, electronic intra-band and interband transitions, magnetic excitations or collective modes. Regarding the intra-band excitations, free charge-carrier excitations lead to prominent features in the spectra and concerning interband transitions, bound electron-hole pairs or excitons can drastically change the absorption spectra. All these features deliver valuable microscopic information about the electronic structure of solids.

In optical spectroscopy the typical unit is the wavenumber:

$$1\,\mathrm{cm}^{-1} = 1.2\,\mathrm{K} = 0.12398\,\mathrm{meV} = 29.979\,\mathrm{GHz} \tag{3.1}$$

3.1 Electrodynamics in Matter

3.1.1 Linear Response Functions

The interaction of light with matter leads to phenomena like dispersion, refraction, absorption and reflection and for non-magnetic matter, all information on those interactions is described by the dielectric function $\varepsilon(k,\omega)$ where $\mathbf{k}$ is the momentum and ω the frequency.

In solid state physics we deal with many body systems with up to 10^{23} particles. Since it is almost impossible to conceive the microscopic states of so many particles, usually the macroscopic observable behavior is looked at. One example is the macroscopic electrical susceptibility $\chi(\mathbf{k},\omega)$ that is a measure of the response of a net polarization $\mathbf{P}$ to an applied electrical field $\mathbf{E}$. Other examples are the dielectric function $\varepsilon(\mathbf{k},\omega)$ or the optical conductivity $\sigma(\mathbf{k},\omega)$. The displacement field $\mathbf{D}$, the polarization $\mathbf{P}$ and the current $\mathbf{J}$ are connected to the electrical field $\mathbf{E}$ by the the following relations formulated in Fourier space:

$$\mathbf{D}(\mathbf{k},\omega) = \varepsilon_0\,\varepsilon(\mathbf{k},\omega)\mathbf{E}(\mathbf{k},\omega) \tag{3.2}$$

$$\mathbf{P}(\mathbf{k},\omega) = \varepsilon_0\,\chi(\mathbf{k},\omega)\mathbf{E}(\mathbf{k},\omega) \tag{3.3}$$

$$\mathbf{J}(\mathbf{k},\omega) = \sigma(\mathbf{k},\omega)\mathbf{E}(\mathbf{k},\omega) \tag{3.4}$$

The response functions $\varepsilon(\mathbf{k},\omega)$, $\chi(\mathbf{k},\omega)$, and $\sigma(\mathbf{k},\omega)$ in general are second rank tensors. Since the electric field of the electromagnetic wave is transverse to the photon momentum, the elements of the dielectric tensor and the optical conductivity are transverse to the direction of propagation. In solids with orthorhombic symmetry the tensors are diagonal. This will be discussed in more detail later. In isotropic media, the response functions reduce to scalar functions. In the energy range of optical absorptions, the wavelengths of the electromagnetic wave is much larger than the atomic length scale and therefore, the wavevector $\mathbf{k}$ is assumed to be zero. The dielectric function is then written as $\varepsilon(\omega)$.

3.1.2 Kramers-Kronig-Relations

From the causality principle follows that real and imaginary part of a response function are not independent from each other. This shall be illustrated first by Fig. 3.1 [91]. In the upper graph of figure 3.1 we see a wave packet **A** at the time t = 0. It is a sum of all Fourier components $\cos(\omega_i, t)$ which are all defined from $-\infty < t < \infty$. Next, it is assumed that one frequency $\cos(\omega_0, t)$, denoted with component **B**, is absorbed. If absorption and dispersion were independent from each other, the output simply was the difference A-B = A - $\cos(\omega_0, t)$ for all t. If we look at figure 3.1, the problem is obvious. The answer of the system exists already at $t < 0$, before the question was posed. This is in contradiction to the causality principle and therefore must be wrong. The solution to the problem is that the other components of the wave packet undergo a phase shift such that the answer at $t < 0$ vanishes. The Kramers-Kronig relations are derived with complex analysis. If a general complex valued response function

$$\beta(\omega) = \beta_1(\omega) + \beta_2(\omega) \tag{3.5}$$

satisfies the conditions that $\beta(\omega)$ does not have singularities in the plane of complex frequencies for $Im(\omega) > 0$ and $\beta(\omega)/\omega$ goes faster to zero for $|\omega| \to \infty$ than $1/|\omega|$, the integral

$$I(\omega) = \int_C \frac{\beta(\omega')}{\omega' - \omega} d\omega' \tag{3.6}$$

over the complex half space vanishes because it is equal to the sum of residues which was defined to be zero by the condition that $\beta(\omega)$ is not allowed to have singularities in the upper half space of the complex plane, i.e. $\beta(\omega)$ is analytic. Therefore:

$$\oint_c = \int_{C_1} + \int_{C_2} + \int_{C_3} + \int_{C_4} = 0. \tag{3.7}$$

The integral over C_4 vanishes due to the the asymptotic behavior of $\beta(\omega)$. The

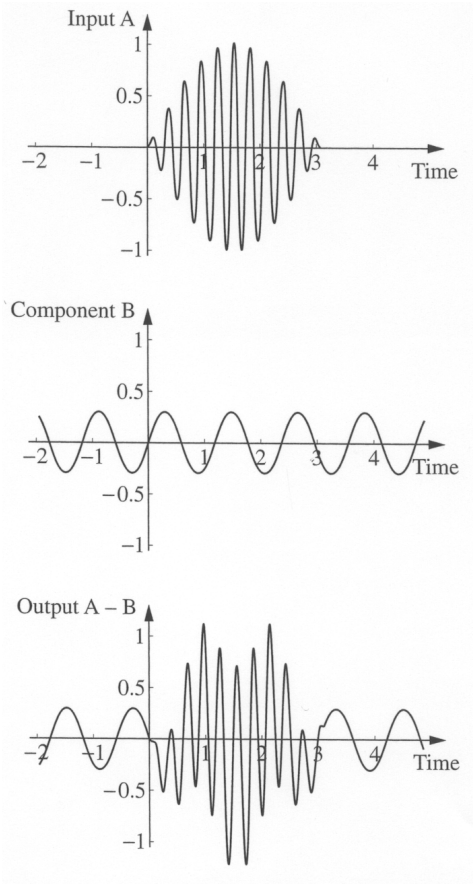

Figure 3.1: Correlation between absorption and dispersion, reproduced from [91]

maximum value of the integral over a semi-circle for $\omega' \to \infty$ approaches the value of the path length which is $\pi\omega'$. Since the function $\beta(\omega)$ goes faster to zero than $1/|\omega|$, the integral vanishes in the limit of $\rho \to 0$. Then the integral over C_2 becomes:

$$lim_{\rho\to 0} \int_{C_2} \frac{\beta(\omega')}{\omega' - \omega} d\omega' = -i\pi\alpha(\omega), \tag{3.8}$$

where ρ denotes the radius of the semi-circle around the singularity at frequency ω. It follows

$$lim_{\rho\to 0} \left[\int_{C_1} \frac{\beta(\omega')}{\omega' - \omega} d\omega' + \int_{C_3} \frac{\beta(\omega')}{\omega' - \omega} d\omega' \right] - i\pi\alpha(\omega) = 0 \tag{3.9}$$

and

$$\alpha(\omega) = \frac{1}{i\,\pi} \mathcal{P} \int_{-\infty}^{\infty} \frac{\beta(\omega')}{\omega' - \omega} d\omega' \tag{3.10}$$

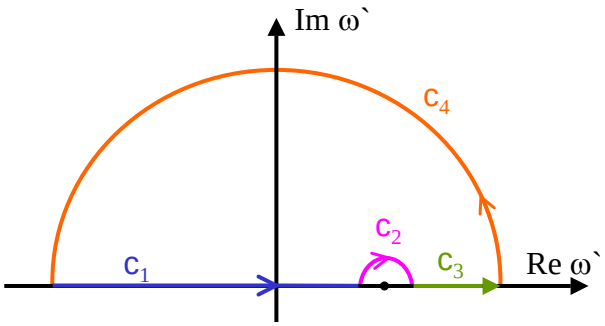

Figure 3.2: Path of integration in the plane of complex frequencies ω'.

where $\mathcal{P}$ is the principal value of the Cauchy-integral in equation 3.9. Splitting the integral into real and imaginary part leads to the Kramers-Kronig relations. Using the symmetry conditions for a real valued function $\beta_1(-\omega) = \beta_1(\omega)$ and $\beta_2(-\omega) = -\beta_2(\omega)$, the above equations read

$$\beta_1(\omega) = \frac{2}{\pi}\mathcal{P}\int_0^\infty \frac{\omega'\,\beta_2(\omega')}{\omega'^2 - \omega^2}d\omega' \tag{3.11}$$

and

$$\beta_2(\omega) = -\frac{2\,\omega}{\pi}\mathcal{P}\int_0^\infty \frac{\beta_1(\omega')}{\omega'^2 - \omega^2}d\omega'. \tag{3.12}$$

It can be shown that the dielectric function shows the same symmetry features and fulfills the the analytic properties and asymptotic behavior as β. Thus the Kramers-Kronig relations for the dielectric function follow:

$$\varepsilon_1(\omega) - 1 = \frac{2}{\pi}\mathcal{P}\int_0^\infty \frac{\omega'\,\varepsilon_2(\omega')}{\omega'^2 - \omega^2}d\omega' \tag{3.13}$$

and

$$\varepsilon_2(\omega) = -\frac{2\,\omega}{\pi}\mathcal{P}\int_0^\infty \frac{\varepsilon_1(\omega')}{\omega'^2 - \omega^2}d\omega'. \tag{3.14}$$

In general, the dielectric function cannot be addressed directly by experimental methods. At optical frequencies, the experimental observables for the electromagnetic response of a solid are the reflectance R, transmittance T and ellipsometric angles Ψ and Δ which are all frequency dependent. The real and imaginary parts of the complex dielectric function $\varepsilon(\omega) = \varepsilon_1(\omega) + i\varepsilon_2(\omega)$, the complex refractive index $\mathrm{N}(\omega) = \mathrm{n}(\omega) + \mathrm{i}\ \mathrm{k}(\omega) = \sqrt{\varepsilon(\omega)}$ and the complex optical conductivity $\sigma(\omega) = \sigma_1(\omega) + i\sigma_2(\omega)$ can be determined by several approaches. Those can be a combination of reflectance and transmittance measurements, a Kramers-Kronig analysis of either reflectance or transmittance or through determination of ellipsometric coefficients.

The refractive index is related to the real and imaginary part of the dielectric function by:

$$N(\omega) = n(\omega) + ik(\omega) = \sqrt{\varepsilon(\omega)} = \sqrt{\varepsilon_1 + i(\frac{4\pi\sigma_1}{\omega})} \tag{3.15}$$

where σ_1 is the real part of the optical conductivity that represents losses due to dissipation. For the real and imaginary part of the dielectric function follows

$$\varepsilon_1(\omega) = n(\omega)^2 - k(\omega)^2 \tag{3.16}$$

$$\varepsilon_2(\omega) = 2n(\omega)k(\omega). \tag{3.17}$$

In the case of normal incidence, the complex reflectivity is defined as

$$r(\omega) = \frac{N(\omega) - 1}{N(\omega) + 1} \tag{3.18}$$

and the measured intensity reflectance is

$$R(\omega) = |r(\omega)|^2 = \frac{(n-1)^2 + k^2}{(n+1)^2 + k^2}, \tag{3.19}$$

$$r(\omega) = |r(\omega)|e^{i\phi_r} = \sqrt{R(\omega)}\, e^{i\phi_r}, \tag{3.20}$$

where $R(\omega)$ is the measured intensity reflectance and ϕ_r the phase shift. It follows

$$ln\, r(\omega) = ln|r(\omega)| + i\phi_r(\omega). \tag{3.21}$$

Thus from equation 3.14 ϕ_r can be calculated if the reflectance is known over a broad range of frequencies and adequate extrapolations to zero and high frequencies are made. For insulators, R = const. for $\omega \to 0$ and for metals, a Hagen-Rubens behavior $R \propto \sqrt{\omega}$ for $\omega \to 0$ is assumed. If the DC-conductivity is known, it is used as a reference value. At high frequencies, a decay of R $\propto \omega^{-4}$ is assumed.

$$\phi_r(\omega) = -\frac{2\,\omega}{\pi}\,\mathcal{P}\int_0^\infty \frac{ln\,|r(\omega)|}{\omega^2 - \omega'^2} d\omega'. \tag{3.22}$$

A detailed description about the numerical evaluation of this integral can be found in [92]. Measurements of the the reflectance $R(\omega)$ determines $n(\omega)$ and $k(\omega)$ by the equations:

$$n(\omega) = \frac{1 - R(\omega)}{1 + R(\omega) - 2\sqrt{R(\omega)}\cos(\phi_r(\omega))} \tag{3.23}$$

and

$$k(\omega) = \frac{2\,\sqrt{R(\omega)}\sin(\phi_r(\omega))}{1 + R(\omega) - 2\sqrt{R(\omega)}\cos(\phi_r(\omega))}. \tag{3.24}$$

If in addition the transmittance is measured, the equations

$$T = \frac{(1-R)^2\Phi}{1-(R\,\Phi)^2} \tag{3.25}$$

and

$$\Phi = e^{-(4\pi k d\omega)/10^4} \tag{3.26}$$

can be used. Here d denotes the sample thickness in μm and ω the frequency in cm^{-1}. The optical conductivity in SI units can be calculated directly if a combination of reflectance and transmittance measurements is done [93]:

$$\sigma_1 = 2\varepsilon_0\tilde{\omega}n\,k. \tag{3.27}$$

Here, $\tilde{\omega} = 2\pi\nu$ is the angular frequency which translates into wave numbers by $\tilde{\omega}[s^{-1}] = 29.97 \cdot 10^9\omega[\text{cm}^{-1}]$. In case of very small samples, a reflectance measurement might be inaccurate or impossible to do at all. In that case, the following approximation can be used[94] for regions where absorptions are small, i. e. above the phonon region and well below the band-gap transitions

$$T \approx (1-R)^2 e^{-\alpha(\omega)d}. \tag{3.28}$$

In this region, the reflectance R is small and nearly constant. Here, $\alpha = 2\frac{\omega k}{c}$ is the linear absorption coefficient and d is the sample thickness given in μm. Then the following approximation for the absorption can be made:

$$\alpha(\omega) \approx -\ln T/d + 2\ln(1-R)/d \approx -\ln T/d + \text{const.} \tag{3.29}$$

From the relations above, n and k read inverted:

$$n = \frac{1+R+\sqrt{4R-k^2(R-1)^2}}{1-R} \tag{3.30}$$

$$k = \frac{10^4}{4\pi d\,\omega}\ln\frac{-2R^2T}{(1-R)^2-\sqrt{(1-R)^4+4R^2\,T^2}}. \tag{3.31}$$

Finally, the optical conductivity $\sigma = \sigma_1 + i\sigma_2$ reads

$$\sigma_1 = \varepsilon_0\,\tilde{\omega}\,\varepsilon_2 \tag{3.32}$$

$$\sigma_2 = \varepsilon_0\,\tilde{\omega}\,(1-\varepsilon_1). \tag{3.33}$$

The equations are given in SI units where $[\sigma] = \Omega^{-1}$ cm^{-1}, $\varepsilon_0 = 8.85 \cdot 10^{-14} s\Omega^{-1}$ cm^{-1}. A very nice conversion table can be found in [95].

3.2 Fundamentals of Ellipsometry

In ellipsometry, the change of the polarization state of a light beam after interaction with a sample is measured. Two independent parameters are obtained in one measurement and both, real and imaginary parts of the dielectric function can be calculated. The principles of ellipsometry go back to Paul Drude and his concept is now referred to as standard ellipsometry. This chapter shall give an insight into the fundamentals of ellipsometry. It starts with the description of the Stokes parameters and the Mueller and Jones matrix formulation, followed by the introduction of the ellipsometric parameters Ψ and Δ. Finally, an example of a measurement setup is given and the Euler angles are introduced.

3.2.1 Polarized Light

The polarization state of a monochromatic light wave is in general elliptic. This means the endpoint of the electric field vector $\mathbf{E}$ moves periodically around an ellipse at each point in space in a fixed plane perpendicular to the propagation vector $\mathbf{k}$. In other words, the electric field vector rotates and changes its magnitude as well. In special cases it moves on a circle (circularly polarized) or a straight line (linearly polarized) [96]. In all cases we speak of fully polarized light. The behavior of the electric field vector depends on the intensities of two of its components which are arbitrary but orthogonal and the correlation between them. In case of unpolarized light the endpoint moves irregularly and the $\mathbf{E}$ vector shows no preferential direction.

Stokes Vector and Mueller Matrix

In 1852, G.G. Stokes [97] proposed that the most general description of the polarization state of a light beam can be achieved by introducing four parameters s_0, s_1, s_2, and s_3 which all have the dimension of intensity. These parameters were called Stokes parameters and they can be used to describe partially and fully polarized light. They may be defined either operational [98, 99] or in terms of electromagnetic theory [100–102]. For a better understanding, it is helpful to look at the operational approach first. In this case, the parameters can be defined by a set of four optical filters. Each will transmit half the incident light and will be interposed one after the other into the beam. For example, let the first be isotropic, the second linearly horizontally polarizing, the third linearly $+45°$ polarizing and the last one right-circularly polarizing. Then a polarization-independent, intensity-calibrated detector is put into the beam. The four signals at the detector may be called I_0, I_1, I_2 and I_3. The operational definition of the

Stokes parameters is then

$$\begin{aligned} s_0 &= 2I_0 \\ s_1 &= 2I_1 - 2I_0 \\ s_2 &= 2I_2 - 2I_0 \\ s_3 &= 2I_3 - 2I_0 \end{aligned} \tag{3.34}$$

where s_0 gives the total intensity, s_1 the difference between intensities between the x and y component. The value of s_1 can be positive (preference for horizontal polarization), negative (tendency for vertical polarization) or zero (e.g. elliptically, circularly polarized or unpolarized). Similar arguments are valid for s_3 (+45° or -45° linear polarization). If $s_3 > 0$, the beam shows a preference toward right-handedness, and if negative, towards left-handedness [98, 99]. In a completely polarized beam $s_0^2 = s_1^2 + s_2^2 + s_3^2$ applies, i. e. the first Stokes parameter is redundant. In a partially polarized beam $s_0^2 > s_1^2 + s_2^2 + s_3^2$ is true. In that case, s_0 is no longer redundant since it contains information on the unpolarized light.

Derivation of the Stokes parameters from the polarization ellipse

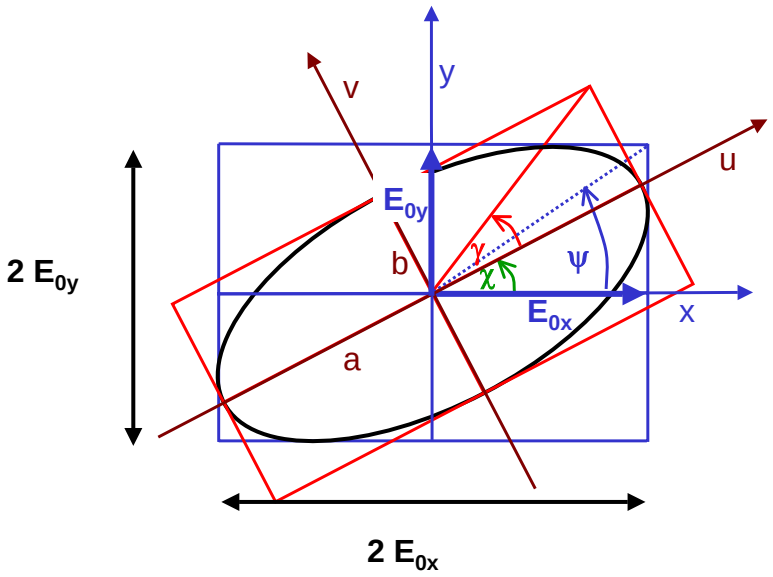

Figure 3.3: Sketch of a polarization ellipse that is drawn into a Cartesian coordinate system. The angle χ describes the rotation of the ellipse around the origin. The new coordinates are denoted by u and v.

In the following the relation between the Stokes parameters and the polarization ellipse is described. A monochromatic light wave with frequency ω which propagates along the z direction can be described by the following equations

$$\begin{aligned} E_x(t) &= E_{0x}(t)\cos(\omega t + \delta_x) \\ E_y(t) &= E_{0y}(t)\cos(\omega t + \delta_y) \end{aligned} \tag{3.35}$$

where $E_x(t)$ and $E_y(t)$ represent the orthogonal components of the electric field vector at a certain point in space. By combining both expressions, the general equation of the polarization ellipse [99] at a given instant of time follows

$$\frac{E_x^2(t)}{E_{0x}^2} + \frac{E_y^2(t)}{E_{0y}^2} - \frac{2E_x(t)E_y(t)}{E_{0x}E_{0y}}\cos\Delta = \sin^2\Delta \tag{3.36}$$

where $\Delta = \delta_y - \delta_x$. The observables of the electromagnetic field are obtained by taking the time averages

$$\frac{\langle E_x^2(t)\rangle}{E_{0x}^2} + \frac{\langle E_y^2(t)\rangle}{E_{0y}^2} - \frac{\langle 2E_x(t)E_y(t)\rangle}{E_{0x}E_{0y}}\cos\Delta = \sin^2\Delta. \tag{3.37}$$

This is the equation of an ellipse drawn into a rectangle with sides $2E_{0x}$ and $2E_{0y}$ and rotated in the coordinate system x,y by an angle χ as shown in figure 3.3. The ellipse touches the sides at ($\pm$ E_{0x}, $\pm$ E_{0y} cos Δ) and ($\pm$ E_{0x} cos Δ, $\pm$ E_{0y}). After taking the time average over an infinite interval of time[1] and using some substitutions, the equation of the ellipse will look as follows [102]:

$$(E_{0x}^2 + E_{0y}^2)^2 - (E_{0x}^2 - E_{0y}^2)^2 - (2E_{0x}E_{0y}\cos\Delta)^2 = (2E_{0x}E_{0y}\sin\Delta)^2. \tag{3.39}$$

By substituting the expressions in parentheses with

$$\begin{aligned} s_0 &= E_{0x}^2 + E_{0y}^2 \\ s_1 &= E_{0x}^2 - E_{0y}^2 \\ s_2 &= 2E_{0x}E_{0y}\cos\Delta \\ s_3 &= 2E_{0x}E_{0y}\sin\Delta \end{aligned} \tag{3.40}$$

equation 3.39 reads

$$s_0^2 = s_1^2 + s_2^2 + s_3^2. \tag{3.41}$$

This definition is not as straightforward as the operational approach and especially for s_2 and s_3 it is not directly obvious that they correspond to the parameters defined before. This equivalence is shown very instructively in [100]. As shown above, the Stokes parameters represent the observables of the polarization ellipse. The ellipticity of the ellipse is defined by

[1] Here we have used

$$\langle E_i(t)E_j(t)\rangle = \frac{1}{T}\int_0^T E_i(t)E_j(t)\,dt \tag{3.38}$$

.

$$\tan\gamma = \frac{b}{a} \tag{3.42}$$

and

$$\tan\Psi = \frac{E_{0y}}{E_{0x}}. \tag{3.43}$$

Stokes Vector

As mentioned above, the Stokes parameters represent the most general description of partially polarized and unpolarized light. The following calculus is a powerful tool to describe the polarization state of light and the effect of optical devices on the incident beam. Mueller [103] has shown that the Stokes parameters can be regarded as the components of a 4-vector. Inserting the results of equation 3.40 will lead to:

$$\mathbf{S} = \begin{bmatrix} s_0 \\ s_1 \\ s_2 \\ s_3 \end{bmatrix} = \begin{bmatrix} E_{ox}^2 + E_{oy}^2 \\ E_{ox}^2 - E_{oy}^2 \\ 2E_{ox}E_{oy}\cos\Delta \\ 2E_{ox}E_{oy}\sin\Delta \end{bmatrix}. \tag{3.44}$$

The degree of polarization is defined as:

$$P = \frac{I_{pol}}{I_{unpol}} = \frac{\sqrt{s_1^2 + s_2^2 + s_3^2}}{s_0}. \tag{3.45}$$

The Stokes vector for horizontal polarization ($\Delta = 0$ or π and $E_{0y} = 0$) will be for example $\mathrm{S} = \{E_{0x}^2, E_{0x}^2, 0, 0\}$ or in the normalized form $\mathrm{S} = \{1, 1, 0, 0\}$ [98, 101].

Example: Mueller Matrix of a Polarizer and a Retarder

A polarizer is an optical device that can turn an unpolarized light beam into one with a well defined polarization state. There are different classes of polarizers as to their function like linear, circular or elliptical polarizers. They can be spectrally selective or achromatic, i. e. wavelength independent [98]. In this section, we first cite some examples taken from Shurcliff [98]. The Mueller matrix of a linear polarizer whose transmission axis is horizontal can be written in the form:

$$\begin{bmatrix} 1 & 1 & 0 & 0 \\ 1 & 1 & 0 & 0 \\ 0 & 0 & 0 & 0 \\ 0 & 0 & 0 & 0 \end{bmatrix} \tag{3.46}$$

Retarders are optical elements that, without changing the intensity or degree of polarization of a polarized monochromatic beam, resolve the beam into two components, retards the phase of one relative to the other, and reunites the two

components forming a single beam. Most retarders are of birefringence type like quartz or calcite which were cut parallel to the optical or fast axis. The Mueller matrix of an ideal 180° retarder with the optical or fast axis is at 45° is defined as follows [98]:

$$\begin{bmatrix} 1 & 0 & 0 & 0 \\ 0 & -1 & 0 & 0 \\ 0 & 0 & 1 & 0 \\ 0 & 0 & 0 & -1 \end{bmatrix} \tag{3.47}$$

The following example shows a horizontally polarized beam with the Stokes vector[2] (1,1,0,0) hitting the above mentioned retarder. As we will see, the transmitted beam turns out to be vertically polarized. The corresponding matrix multiplication looks as follows:

$$\begin{bmatrix} 1 \\ 1 \\ 0 \\ 0 \end{bmatrix} = \begin{bmatrix} 1 & 0 & 0 & 0 \\ 0 & -1 & 0 & 0 \\ 0 & 0 & 1 & 0 \\ 0 & 0 & 0 & -1 \end{bmatrix} \begin{bmatrix} 1 \\ -1 \\ 0 \\ 0 \end{bmatrix} \tag{3.48}$$

The first element of the transmitted beam represents the intensity and the second term is negative indicating a preference for vertical polarization.

3.2.2 Jones Vector and Jones Matrix

Another formalism widely used in ellipsometry is the Jones calculus that was first introduced by R.C. Jones in 1940 [104]. The light beam is described by a 2 component vector representing the components of the electric field vector. In analogy to the Stokes- and Mueller matrix calculus, the action of an optical device on the incoming beam is described by a matrix, the so-called Jones matrix J which is a 2 x 2 matrix with, in general, complex entries. However, the Jones formalism is only applicable to polarized light and can therefore not handle depolarizing optical devices or samples.

The Jones vector can be written as follows:

$$\mathbf{E} = \begin{bmatrix} E_x \\ E_y \end{bmatrix} = \begin{bmatrix} |E_x|e^{i\delta_x} \\ |E_y|e^{i\delta_y} \end{bmatrix} \tag{3.49}$$

Where E_x E_y represent the components of the electrical field vector and δ_x and δ_y the phases. The effect on an optical device will change the Jones vector of the incident beam. This change is described by the Jones matrix J of an optical device which relates the Jones vector of the incoming light wave with the one of the outgoing wave.

[2] For simplicity the column vector is here written as a row vector

$$\mathrm{E}_o = \mathrm{J}\mathrm{E}_i \tag{3.50}$$

or

$$\begin{bmatrix} E_{xo} \\ E_{yo} \end{bmatrix} = \begin{bmatrix} J_{11} & J_{12} \\ J_{21} & J_{22} \end{bmatrix} \begin{bmatrix} E_{xi} \\ E_{yi} \end{bmatrix}, \tag{3.51}$$

where E_o represents the outgoing wave and E_i the incoming wave. In the next section we introduce the ellipsometric parameters Ψ and Δ and transform the Jones vector and Jones matrix into the coordinate system for reflection.

3.2.3 Ellipsometric Parameters Ψ and Δ

Figure 3.4 shows a typical ellipsometric setup. The two independent parameters Ψ and Δ are obtained via a measurement of the complex ratio ρ that relates the two linearly independent field components of the polarized light beam before and after interaction with the sample. As we will see, those parameters can be constructed from the polarization ellipse and are consequently also related to the Stokes parameters.

In this notation, the electric field vector E of the electromagnetic plane wave is split into the two linearly independent components E_s and E_p where s (p) denotes the direction perpendicular (parallel) to the plane of incidence (see figure 3.4).

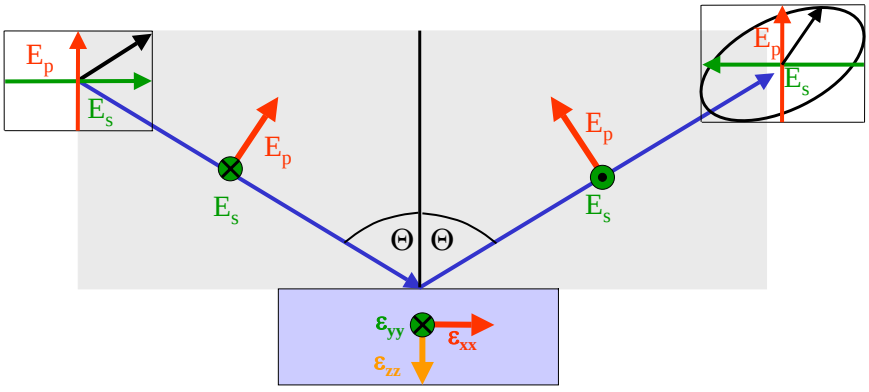

Figure 3.4: Ellipsometric reflection setup. E_p is the component of the field vector parallel to the plane of incidence and E_s the component perpendicular to the plane of incidence. The incoming beam is linearly polarized and the reflected beam in general elliptically polarized. The sketches on the upper left and upper right represent the polarization states when looking into the beam

.

3.2.4 Fresnel equations and Brewster angle

Snells law connects the refractive indices of ambient medium n_i and sample n_t with the angles of incidence θ_i and refraction θ_t

$$n_i sin\theta_i = n_t sin\theta_t \tag{3.52}$$

and the Fresnel equations relate the reflected and transmitted field amplitudes of the electric field vector E_{0r}, E_{0t} to the incident amplitude E_{0i} by the angles of incidence θ_i and transmission θ_t. They can be deduced from the electromagnetic theory of light by taking into account the boundary conditions of the electric and magnetic field amplitudes. The reflection coefficients are defined as follows

$$\begin{aligned} r_p &= \left(\frac{E_{rp}}{E_{ip}}\right) = \frac{\mathrm{n}_t \cos\theta_i - \mathrm{n}_i \cos\theta_t}{\mathrm{n}_i \cos\theta_t + \mathrm{n}_t \cos\theta_i}, \\ r_s &= \left(\frac{E_{rs}}{E_{is}}\right) = \frac{\mathrm{n}_i \cos\theta_i - \mathrm{n}_t \cos\theta_t}{\mathrm{n}_i \cos\theta_i + \mathrm{n}_t \cos\theta_t}. \end{aligned} \tag{3.53}$$

Here, r_p, r_s, n_i and n_t are in general complex quantities. The index of refraction is related to the dielectric function by $\sqrt{\epsilon} = \mathrm{n}$.

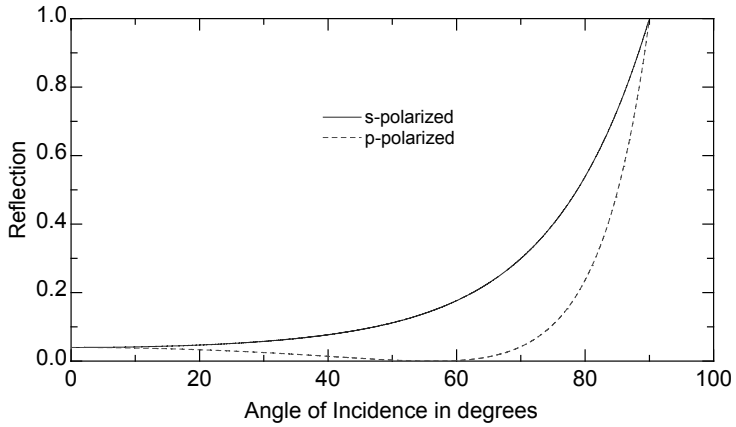

Figure 3.5: The p and s polarized intensity reflectance versus angle of incidence for an isotropic non-absorbing media with $\mathrm{n}_i = 1$ and $\mathrm{n}_t = 1.5$. The p and s reflectance are calculated from the Fresnel reflection coefficients as follows: $R_p = r_p * r_p^*$ where r_p^* denotes complex conjugation. R_p and R_s are identical at normal incidence. The s reflectance increases monotonically from normal to grazing incidence where it approaches unity. The p polarized reflectance, however decreases to zero at the Brewster angle and then increases to unity at grazing incidence [105]

In the coordinate (s, p) coordinate system, the Jones vector of the reflected and incoming wave reads

$$\mathrm{E}_i = \begin{bmatrix} E_{ip} \\ E_{is} \end{bmatrix} = \begin{bmatrix} |E_{ip}|e^{i\delta_{is}} \\ |E_{is}|e^{i\delta_{ip}} \end{bmatrix} \quad \text{and} \quad \mathrm{E}_r = \begin{bmatrix} E_{rp} \\ E_{rs} \end{bmatrix} = \begin{bmatrix} |E_{rp}|e^{i\delta_{rs}} \\ |E_{rs}|e^{i\delta_{rp}} \end{bmatrix}. \tag{3.54}$$

With the Fresnel reflection coefficient for p-polarization

$$r_p = \frac{E_{rp}}{E_{ip}} = \frac{|E_{rp}|e^{i(\delta_{rp})}}{|E_{ip}|e^{i(\delta_{ip})}} = \frac{|E_{rp}|}{|E_{ip}|}e^{i(\delta_{rp}-\delta_{ip})} \tag{3.55}$$

and s-polarization

$$r_s = \frac{E_{rs}}{E_{is}} = \frac{|E_{rs}|}{|E_{is}|}e^{i(\delta_{rs}-\delta_{is})} \tag{3.56}$$

, the complex ellipsometric parameter ρ is defined as

$$\rho = \frac{r_p}{r_s} = \frac{|E_{rp}|}{|E_{ip}|}\frac{|E_{is}|}{|E_{rs}|}\,e^{i\Delta} = tan\Psi\, e^{i\Delta}. \tag{3.57}$$

Here,

$$\Delta = (\delta_{rp} - \delta_{rs}) - (\delta_{ip} - \delta_{is}) \tag{3.58}$$

and

$$\tan\Psi = \frac{|E_{rp}|}{|E_{ip}|}\frac{|E_{is}|}{|E_{rs}|}. \tag{3.59}$$

ρ is the quantity that is actually measured in ellipsometry, i. e. the ratio of field amplitudes is measured, making ellipsometry a very accurate technique. ρ is directly related to the Fresnel reflection coefficients. Since in the experimental setup, the incoming light beam is linearly polarized and then $(\delta_{ip} - \delta_{is})$ is zero or 180°.

Jones matrix of a Reflecting sample

The effect of the Jones matrix of a reflecting sample will be

$$\mathrm{E}_r = \mathrm{R}\mathrm{E}_i, \tag{3.60}$$

$$\mathrm{R} = \begin{bmatrix} r_p & r_{ps} \\ r_{sp} & r_s \end{bmatrix} = \begin{bmatrix} \frac{E_{rp}}{E_{ip}} & \frac{E_{rs}}{E_{ip}} \\ \frac{E_{rp}}{E_{is}} & \frac{E_{rs}}{E_{is}} \end{bmatrix} \tag{3.61}$$

where E_i (E_r) are the component of the incident (reflected) wave. The ellipsometric parameters are defined as

$$\rho = \frac{r_p}{r_s} = \tan(\Psi_p)e^{i\,\Delta} \tag{3.62}$$

$$\rho_{ps} = \frac{r_{ps}}{r_p} = \tan(\Psi_{ps}) e^{i\,\Delta_{ps}} \tag{3.63}$$

$$\rho_{sp} = \frac{r_{sp}}{r_s} = \tan(\Psi_{sp}) e^{i\,\Delta_{sp}} \tag{3.64}$$

In case of orthorhombic samples or higher symmetries, the anisotropy in the measured Mueller matrix elements vanishes and the Jones matrix is diagonal:

$$\mathrm{R} = \begin{bmatrix} r_s & 0 \\ 0 & r_p \end{bmatrix}. \tag{3.65}$$

If the incoming light beam is linearly 45° polarized, $\frac{|E_{is}|}{|E_{ip}|} = 1$. In this case $\tan\Psi_{pp} = \frac{|E_{rp}|}{|E_{rs}|}$. The transformation of the Jones matrix of equation 3.65 into a Mueller matrix normalized to the total intensity m_{11} reads

$$M = \begin{bmatrix} 1 & m_{12} & 0 & 0 \\ m_{21} & 0 & 0 & 0 \\ 0 & 0 & m_{33} & m_{34} \\ 0 & 0 & m_{43} & m_{44} \end{bmatrix}, \tag{3.66}$$

with

$$m_{11} = \frac{|r_p|^2 + |r_s|^2}{2}, \tag{3.67}$$

$$m_{12} = m_{21} = \frac{|r_p|^2 - |r_s|^2}{|r_p|^2 + |r_s|^2}, \tag{3.68}$$

$$m_{33} = m_{44} = 2\,\frac{\mathrm{Re}(r_p)\,\mathrm{Re}(r_s) + \mathrm{Im}(r_p)\,\mathrm{Im}(r_s)}{|r_p|^2 + |r_s|^2}, \tag{3.69}$$

and

$$m_{34} = -m_{43} = 2\,\frac{\mathrm{Re}(r_p)\,\mathrm{Im}(r_s) - \mathrm{Im}(r_p)\,\mathrm{Re}(r_s)}{|r_p|^2 + |r_s|^2}. \tag{3.70}$$

From equation 3.57 the following equations can be derived

$$\mathrm{Re}\,\frac{|r_p|}{|r_s|} = \tan\Psi_p, \tag{3.71}$$

$$\mathrm{Re}\,\frac{r_p}{r_s} = \tan\Psi_p \cos\Delta_p, \tag{3.72}$$

$$\mathrm{Im}\,\frac{r_p}{r_s} = \tan\Psi_p \sin\Delta_p. \tag{3.73}$$

Finally, the Mueller matrix of an orthorhombic or higher symmetry sample with optical axes aligned along the laboratory system reads

$$M = \frac{|r_p|^2 + |r_s|^2}{2} \begin{bmatrix} 1 & -\cos 2\Psi & 0 & 0 \\ -\cos 2\Psi & 1 & 0 & 0 \\ 0 & 0 & \sin 2\Psi \cos \Delta & \sin 2\Psi \sin \Delta \\ 0 & 0 & -\sin 2\Psi \sin \Delta & \sin 2\Psi \cos \Delta \end{bmatrix}. \quad (3.74)$$

3.2.5 Dielectric Function of Anisotropic Bulk Samples

We restrict our considerations to homogeneous, non-magnetic materials. The dielectric tensor describes the most general response of the material. In non-absorbing materials the tensor elements ϵ_{ij} are real. Energy conservation requires that $\epsilon_{ij} = \epsilon_{ji}$, i. e. the tensor is symmetric. This means also that it is always possible to find a cartesian coordinate system (x, y, z) such that the dielectric tensor is diagonal. The (x, y, z) directions for this selection define the principal dielectric axes

$$\epsilon_{ij}(\omega) = \begin{bmatrix} \epsilon_{xx}(\omega) & 0 & 0 \\ 0 & \epsilon_{yy}(\omega) & 0 \\ 0 & 0 & \epsilon_{zz}(\omega) \end{bmatrix}. \quad (3.75)$$

In case of uniaxial materials to which trigonal, tetragonal and hexagonal symmetries belong, $\epsilon_{xx} = \epsilon_{yy} \neq \epsilon_{zz}$. For so-called biaxial systems $\epsilon_{xx} \neq \epsilon_{yy} \neq \epsilon_{zz}$. Those are orthorhombic structures. In case of orthorhombic and higher symmetries, the main dielectric axes coincide with the symmetry axes of the crystal. This means as soon as the orientations of the crystal are known, the dielectric tensor will be diagonal in this crystal coordinate system. The orientation of the main dielectric axes does not change with ω or T. They will always lie along the crystallographic axes, but the length of the principal axes can change, i.e. n_x, n_y and n_z. In the orthorhombic case, three independent quantities namely the diagonal elements of the upper tensor must be specified in order to define the full dielectric tensor. In monoclinic systems however, only one principal dielectric axis lies along a crystallographic axis and in triclinic crystals all three orthogonal principal axes are unspecified even if the crystal axes are known. In addition to that, the variation with ω is unspecified too. This has the consequence that a diagonalization of the dielectric tensor is only possible for orthorhombic structures and higher symmetries. Lower symmetries will produce off-diagonal elements.

3.2.6 Experimental Coordinate System and Euler Angles

The Euler angles describe any rotation needed to match the experimental coordinate system with the the optical axes of the sample. The rotations are defined as follows: φ rotates the laboratory system about the z-axis, ϑ about the new x-axis

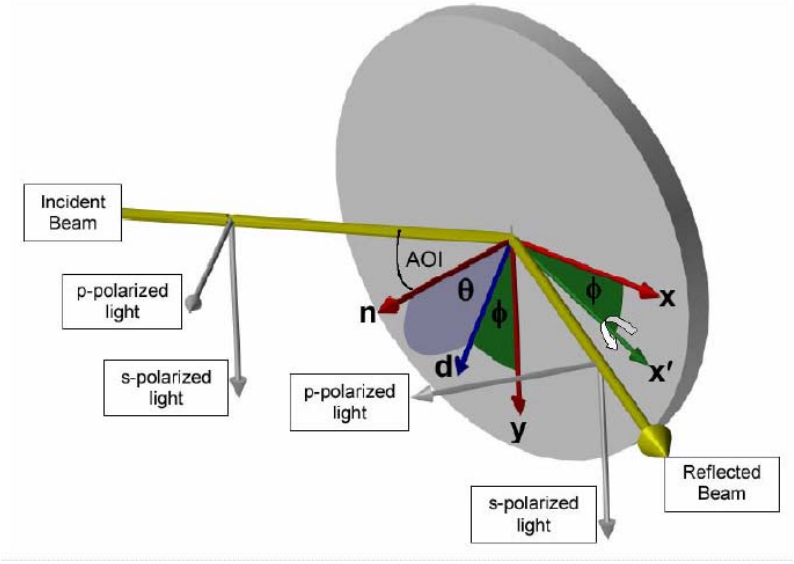

Figure 3.6: Definition of the laboratory system with Euler angles. (Sketch taken from [105].

and ψ about the new z-axis. Assuming normal incidence helps to visualize the experimental coordinate system. The z-axis points along the beam direction normal to the sample plane and into the sample surface. The x-direction lies in the plane of incidence (p-polarization) and the y-direction lies perpendicular to the other two (s-direction). They build a right-handed coordinate system as shown in figure 3.6. If such a rotation is possible, the dielectric tensor can be diagonalized. This is valid for orthorhombic symmetry and higher. If a crystal is oriented in such

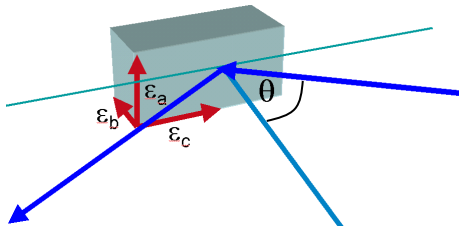

Figure 3.7: Example of measurement configuration of a crystal where two perpendicular surfaces have been prepared. For clarity, the polarization states of the light wave are not shown.

a way that one principal axis is oriented perpendicular to the plane of incidence

and the other one is normal to the surface, the measured dielectric response comes from the tensor projection onto the intersecting line between surface and plane of incidence [106]. The other two components contribute only a little. In figure 3.7 for example, the component ϵ_c is the principal component measured. This approximation is valid if $|\epsilon|$ is moderately large of the order of 10 and for typical angles of incidence of $\theta = 70$. For the above mentioned setup in figure 3.4 the complex pseudodielectric function can be calculated from the matrix elements by using the Fresnel equations

$$\rho_{pp} = \frac{r_{pp}}{r_{ss}} = \left(\frac{\sqrt{\epsilon_{zz} - \sin^2\theta} - \sqrt{\epsilon_{xx}\epsilon_{zz}}\cos\theta}{\sqrt{\epsilon_{zz} - \sin^2\theta} + \sqrt{\epsilon_{xx}\epsilon_{zz}}\cos\theta} \right) \left(\frac{\cos\theta + \sqrt{\epsilon_{yy} - \sin^2\theta}}{\cos\theta - \sqrt{\epsilon_{yy} - \sin^2\theta}} \right) \tag{3.76}$$

where θ is the angle of incidence. The dielectric function can thus be determined by ellipsometric measurement of the complex reflection ratio ρ

$$\epsilon = \epsilon_{xx} = \epsilon_{yy} = \epsilon_{zz} = \sin^2\theta + \sin^2\theta \tan^2\theta \left(\frac{1-\rho}{1+\rho}\right)^2 \tag{3.77}$$

In the next chapter, the experimental setups of Fourier transform spectroscopy and ellipsometry are described with focus on the ellipsometric setup.

4 Experimental Setup

4.1 Spectroscopic Methods

There are several approaches to measure the linear response of a material. These can be divided into three fundamental methods. The first uses monochromatic radiation and the electrodynamic response is measured as a function of frequency. Measured quantities are amplitude and phase of the response as for example is done in ellipsometry. The other two techniques use white light sources tha. The methods can be separated into time-domain and Fourier-spectroscopy. Time domain spectroscopy uses short pulses with defined rising time and measures the time-dependent response of the system. The upper limit of this technique is fixed by the inverse rising time and thus the main working region lies between 10^{-6} up to 10^{9} Hz, i.e. rising times of nano-seconds.

Within the frame of this thesis, Fourier transform spectroscopy and ellipsometry were used to investigate the optical properties of transition metal oxides. Since the focus of this work was to set up the new experimental technique of ellipsometry in our group, the following description will concentrate on fundamentals of ellipsometry and only a short presentation of Fourier transform spectroscopy is given.

4.2 Fourier Transform Infrared Spectroscopy (FT-IR)

FT-IR spectroscopy has gained much importance in optical spectroscopy with the development of fast processing computers. Compared to conventional grating spectrometers where the spectrum $S(\omega)$ is measured at each frequency ω one after the other, [1] in FT-IR spectroscopy all frequencies are measured simultaneously. This involves a lot of mathematical operations such as Fourier transformation and phase corrections. Apart from the data processing computer, the most important device in FT-IR spectrometers is the interferometer, usually a Michelson interferometer.

[1] Here we use the wavenumber $\omega = 1/\lambda$ in cm^{-1} which is commonly used in optical spectroscopy.

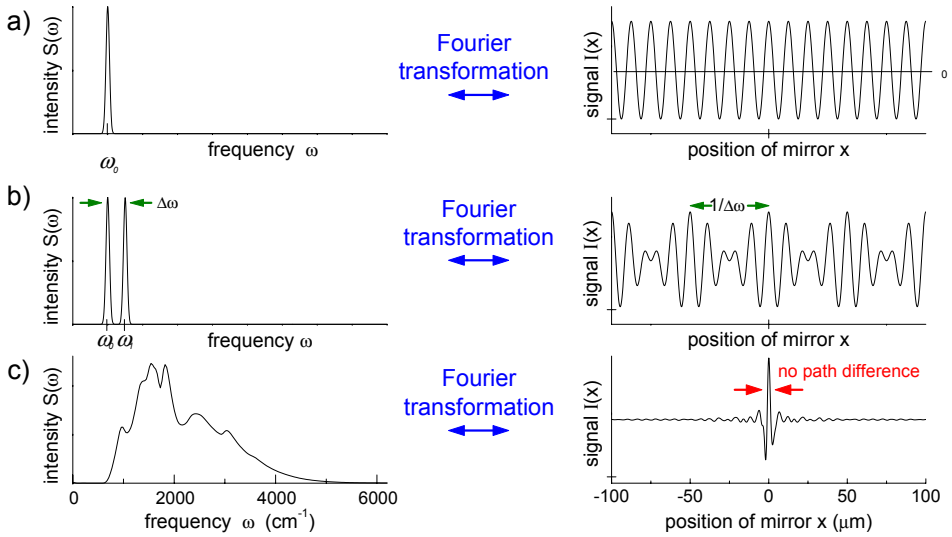

Figure 4.1: Examples of spectra (left) and corresponding interferograms (right) (a) one monochromatic line, (b) two monochromatic lines and (c) broadband spectrum of polychromatic source, taken from [35] and [107]

.

Michelson Interferometer

The radiation of a white-light source is separated by a beam splitter into two interfering rays. Those two beams are reflected by two mirrors one of which is movable, producing variable path differences $\delta = 2$ x where x is the distance of the movable mirror with respect to the fixed mirror. For $\delta = 0, \lambda, 2\lambda$ this yields constructive interference of the two beams and for $\delta = \lambda/2, 3/2\lambda...$ this leads to destructive interference. An intensity pattern as seen in figure 4.1 (a) is measured in case of monochromatic light. The response of the system is measured as a function of the path difference which means the interferometer changes the frequency dependence S(ω) into a space-dependence of the measured intensity I(x). Those quantities are related to each other by a Fourier transformation. The task is to measure the intensity of the detector signal $I(x)$ against the position x of the movable mirror. The main problem exists in the determination of the actual position of the fixed mirror. For this reason, an additional monochromatic light source (He-Ne Laser) is used. The laser beam passes the interferometer and produces an interferogram as shown in figure 4.1 (a)

The intensity I(x) then is given by the following relation $I(x) = S(\omega)\cos(2\pi x/\lambda_0)$ and this equation leads to the position x if λ_0 is known. S(ω) is the intensity of the spectral line at wave number ω_0. In the case of a polychromatic light source,

the intensity can be expressed by an integral over all frequencies:

$$I(x) = \int_0^\infty S(\omega)\cos(2\,\pi\omega x)d\,\omega. \tag{4.1}$$

However, the interferogram $I(x)$ of the polychromatic light source is digitalized by switching on the detector each time the interferogram of the monochromatic reference laser passes through zero, leading to an interferogram that is only known at N discrete, equidistant points, $x_n = n\,\Delta x$. This yields to $S(\omega)$ given only at discrete $\omega_k = k\,\Delta\omega$. Then, $I(n\Delta x)$ and $S(k\Delta\omega)$ are connected by a discrete Fourier [107] and equation4.1 becomes a sum over the sampling points N:

$$I(n\,\Delta x) = \sum_{k=0}^{N-1} S(k\,\Delta\omega)e^{-(2\,\pi nk/N)}. \tag{4.2}$$

For $n = 0$ the exponential function in the equation 4.2 is 1 and the intensity at the so-called white-light-position, I(0) is the sum over all N spectral intensities, divided by N. In other words, the maximum of the interferogram represents the average intensity of the spectrum. As depicted in figure 4.1 (b) it is necessary to measure a path difference of at least x = $1/\Delta\omega$ to resolve two discrete frequencies with distance $\Delta\omega$ since the interferogram of two adjacent spectral lines shows a periodic modulation that is repeated after a distance $1/\Delta\omega$. The smaller the distance $\Delta\omega$, the larger the path difference. For example to reach a resolution of $\Delta\omega = 0.1\,\mathrm{cm}^{-1}$ the movable mirror has to move 6 cm. Other aspects of data processing like zero-filling and aliasing are described in detail in [35, 107]. A big advantage of Fourier spectroscopy is the fast working speed. All frequencies can be measured within seconds (Fellget-advantage). A good signal to noise ratio is achieved by averaging many scans. The Fourier spectrometer in our group works best in the infrared region due to intensity lack of available sources in the low-frequency region (Planckt's law) and strong influence of mechanical instabilities on the beam path in the short wavelength region. The following table lists the spectral range covered by optical spectroscopy. There is a smooth crossover between neighboring regions.

spectral region	wavenumbers	wavelength	frequency	Energy
FIR	10 - 500	1 mm - 20 μm	0.3 - 15 THz	1.2 - 60 meV
MIR	500-5 000	20 - 2 μm	15 - 150 THz	60 - 600 meV
NIR	5 000-12 500	2 μm - 800 nm	150 - 375 THz	0.6 - 1.5 eV
VIS	12 500-25 000	800-400 nm	375-775 THz	1.5 - 3.1 eV
UV	25 000-100 000	400- 1 nm	775 - 3 000 THz	3.1 - 12 eV

Table 4.1: Spectral ranges in optical spectroscopy with typical units.

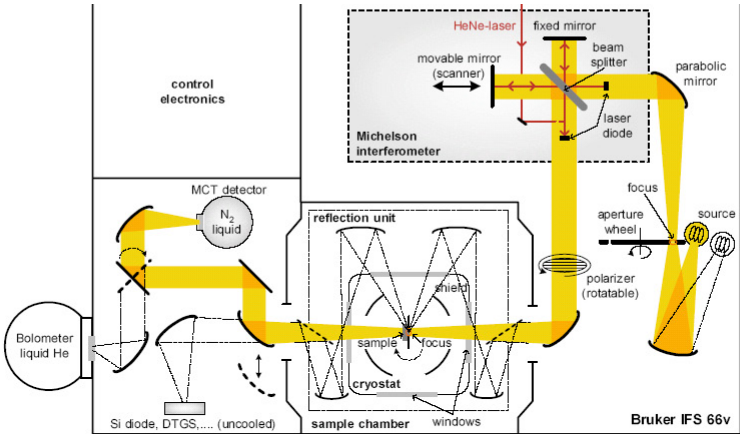

Figure 4.2: Schematic picture of the Fourier transform spectrometers used in our group.

.

4.2.1 Experimental Setup

A typical FT-IR setup is depicted in figure 4.2 Two Bruker IFS 66v/S Fourier transform spectrometers are available in our group. Both spectrometers are equipped with exchangeable light sources, detectors and beam splitters covering an energy range from 10 meV to 3 eV. In addition to that, the spectrometers are equipped with liquid He-flow cryostats that enable measurements in a temperature range from 10 - 800 K. The setup can be used for transmittance or reflectance measurements by inserting or taking out the so-called reflection unit, see figure 4.2.

Reflectance and Transmittance Measurements

To get information on the electrodynamic properties of a sample, each measurement has to include a reference measurement containing information on the characteristic spectral distribution of the light source, beam-splitter, detector, etc. In transmittance setup, an empty aperture is used and in reflectance, the reference is a gold or aluminium mirror. The transmittance $T(\omega)$ and reflectance $R(\omega)$ of the sample is calculated as follows

$$\begin{aligned} T(\omega) &= \frac{S(\omega)_{\mathrm{sam}}}{S(\omega)_{\mathrm{ref}}} \\ R(\omega) &= \frac{S(\omega)_{\mathrm{sam}}}{S(\omega)_{\mathrm{ref}}} R(\omega)_{\mathrm{ref}}, \end{aligned} \tag{4.3}$$

where $R(\omega)_{\mathrm{ref}}$ is the known reflectance of the reference material (Au, Al) and $S(\omega)_{sam}$ and $S(\omega)_{ref}$ are the sample and reference spectra.

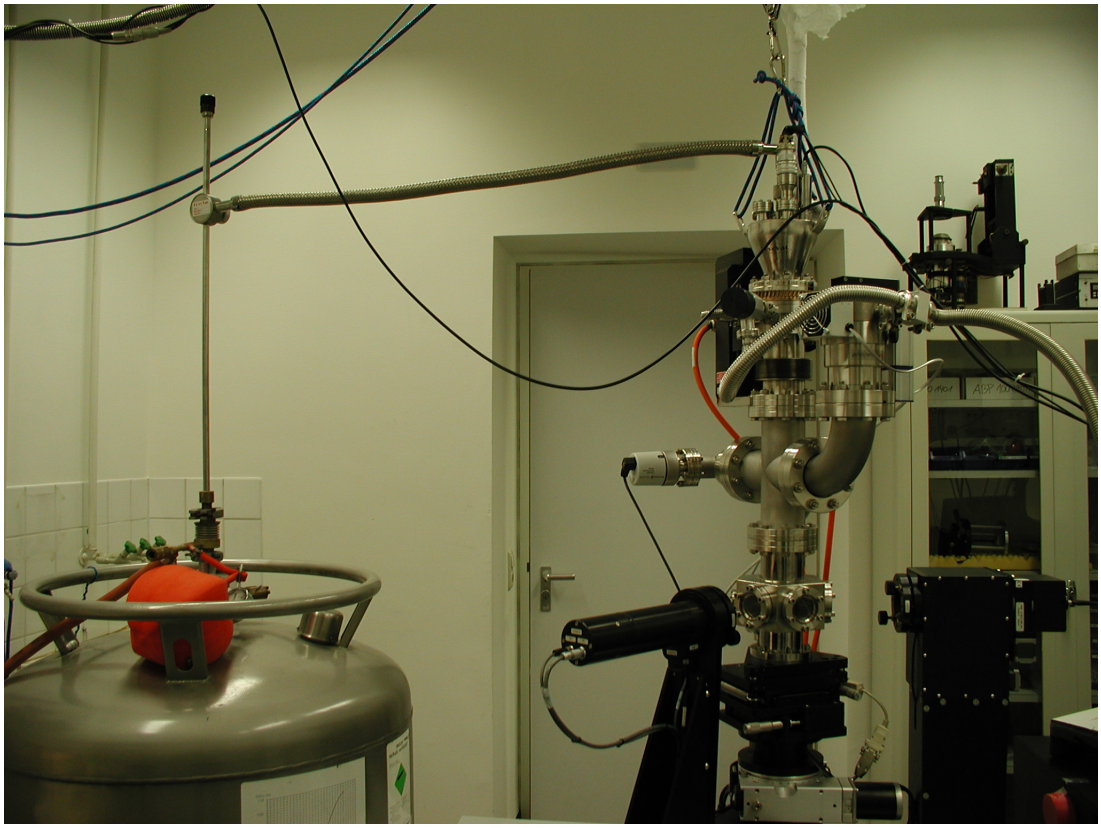

Figure 4.3: Woollam VASE Ellipsometer with liquid He-flow UHV cryostat on the sample stage connected to liquid He-Dewar.

4.3 Ellipsometry

Within the frame of this thesis, the Woollam Ellipsometer WVASE (**W**oollam **V**ariable **A**ngle **S**pectroscopic Ellipsometry) setup with rotating analyzer (RAE) configuration has been used. It is equipped with exchangeable setups for room-temperature measurements and low-temperature measurements with a liquid-Helium flow cryostat(KONTI cryostat, Cryovac). The complete setup includes a broad band light source (Xe-lamp, 190 nm - 2000 nm, USHIO, Hamamatsu), double-grating monochromator, an optical fiber, a sample stage, an analyzing polarizer and a twin-detector. The setup with cryostat is shown schematically in figure 4.3. Several optical fibers with different diameters are available. We usually worked with the 200 μm UV fiber. Since the fiber shows an optical absorption in the range of 0.86-0.92 eV, the experimental data of this region are skipped automatically and a straight line is generated. At the exit of the monochromator right before entering the fiber, a chopper wheel is placed to filter out room light at the detector. After the polarizer, a MgF_2 Berek waveplate is placed working as

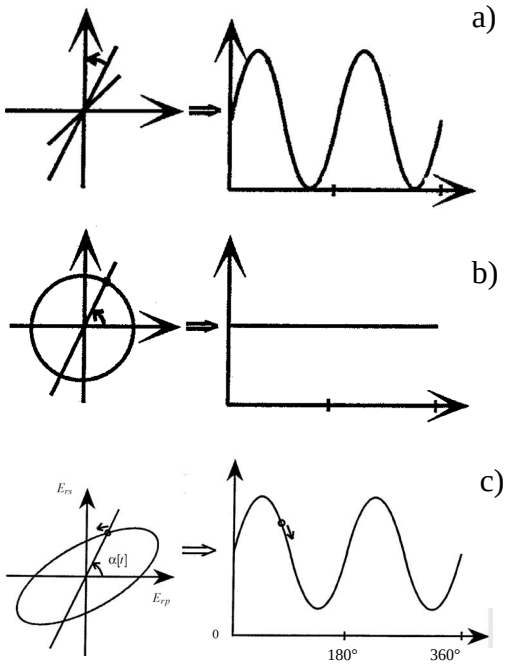

Figure 4.4: Detector signal of a) linearly, b)circularly and c) elliptically polarized light after passing a continuously rotating analyzer.

a retarder. It induces a well defined phase shift Δ_r between 0° and 90°. It is recommended to impose a retardation of 90° as will be described in the next section. Several angles of incidence can be measured between 20° to 90° with the room temperature setup. With the cryostat most measurements were carried out at an angle of incidence of 70°±5°. In the following, the principal data acquisition procedure is described in the Jones and later in the Mueller matrix formalism, followed by a description of low-temperature measurements with a cryostat. Moreover, an exemplary data acquisition and modeling examples is given.

4.3.1 Rotating analyzer

In the rotating analyzer configuration, a modulated intensity is measured at the detector as shown in figure 4.4. The Fourier coefficients of the signal which are related to the ellipsometric angles Ψ and Δ are calculated. The signal at the detector for different polarization states after passing a rotating analyzer is described by:

$$\mathrm{V(t)} = \mathrm{V_0} + a\cos(2\omega t) + b\sin(2\omega t) \tag{4.4}$$

where V(t) is the signal at the detector measured by the voltage. The measured quantities are the normalized Fourier coefficients of the signal $\alpha = \frac{a}{\mathrm{V_0}}$ and $\beta = \frac{b}{\mathrm{V_0}}$.

In Jones formalism the action of a reflecting sample and optical devices on the light beam can be formulated as a multiplication of Jones matrices. The state of polarization at the detector is:

$$E_D = \begin{bmatrix} 1 & 0 \\ 0 & 1 \end{bmatrix} \times \begin{bmatrix} \cos A & \sin A \\ -\sin A & \cos A \end{bmatrix} \times \begin{bmatrix} r_{pp} & 0 \\ 0 & r_{ss} \end{bmatrix} \times \begin{bmatrix} \cos P & -\sin P \\ \sin P & \cos P \end{bmatrix} \times \begin{bmatrix} 1 \\ 0 \end{bmatrix} E_i, \tag{4.5}$$

and after multiplication follows:

$$E_D = \begin{bmatrix} r_{pp} \cos P \cos A + r_{ss} \sin P \sin A \\ 0 \end{bmatrix}. \tag{4.6}$$

The measured quantity at the detector is proportional to the squared component of the electrical field vector. After some substitutions using cosine functions the intensity will be

$$\begin{aligned} I_D \propto & \tfrac{1}{2} |r_{pp}|^2 \cos^2 P + \tfrac{1}{2} |r_{ss}|^2 \sin^2 P \\ & + \tfrac{1}{2} \left(|r_{pp}|^2 \cos^2 P - |r_{pp}|^2 \sin^2 P \right) \cos 2A \\ & + \tfrac{1}{2} 2\, Re\left(r_{pp}\, r_{ss}^*\right) \cos P \sin P \sin 2A, \end{aligned} \tag{4.7}$$

and by comparing with equation 4.4 we can identify α and β

$$I_D = V_0 \left(1 + \alpha \cos 2A + \beta \sin 2A\right). \tag{4.8}$$

It follows

$$\alpha = \frac{|r_p/r_s|^2 - \tan^2 P}{|r_p/r_s|^2 + \tan^2 P}, \tag{4.9}$$

$$\beta = \frac{2\, Re(r_p/r_s) \tan P}{|r_p/r_s|^2 + \tan^2 P}, \tag{4.10}$$

and using the substitution $\rho = \frac{r_{pp}}{r_{ss}} = \tan \Psi\, e^{i\Delta}$ α and β will become

$$\alpha = \frac{\tan^2 \Psi - \tan^2 P}{\tan^2 \Psi + \tan^2 P}, \tag{4.11}$$

$$\beta = \frac{2 \tan \Psi \cos \Delta \tan P}{\tan^2 \Psi + \tan^2 P}. \tag{4.12}$$

This relates the ellipsometric parameters Ψ and Δ to the measured Fourier-coefficients α and β. Inversion leads to

$$\tan \Psi = \sqrt{\frac{1+\alpha}{1-\alpha}}\, |\tan P| \tag{4.13}$$

and

$$\cos \Delta = \frac{\beta}{\sqrt{1-\alpha^2}} \frac{\tan P}{|\tan P|}. \tag{4.14}$$

To achieve a good signal to noise ratio, a high number of rotations of the analyzer have to be used and the average intensity at the detector should be as high as possible which is the case for circularly polarized light. For circularly polarized light α and β go to zero. If we consider equations 4.11 and 4.12, it follows that for $\alpha = 0$ the polarizer angle P must be equal to Ψ, and for $\beta = 0$ the phase difference must be $\Delta = \frac{\pi}{2}$ which corresponds to circularly polarized light. Δ may be varied by changing the angle of incidence. Near the Brewster angle where r_{pp} is almost zero, Δ is near $\frac{\pi}{2}$. Therefore it is advisable to measure several angles of incidence around the Brewster angle such that $\Delta \approx \frac{\pi}{2}$ can be measured for all different wavelengths. In any case it may be useful to measure different angles of incidence in order to discern possible surface layers because the optical path changes with angle of incidence.

Accuracy and Calibration Procedure

much attention has to be paid to the calibration procedure and accuracy of the ellipsometric system to ensure accurate optical constants or layer thicknesses of investigated samples. The latter can be verified by measuring a reference sample like SiO_2 on Si wafers. However, the precision of ellipsometer systems is often better than the tolerance of the supplied reference standards. Therefore it is a good idea to check the ellipsometer in straight through position in air for which the ellipsometric parameters are by definition $\Psi = 45°$ and $\Delta = 0°$. This accuracy test however does not guarantee accurate ellipsometric data on general samples, but a good starting point to check the ellipsometric system. Before the the ellipsometer can acquire data, a calibration script supplied by the J.A. Woollam company is run in our group. The aim is to determine the true values, i.e. the absolute position of the polarizer and analyzer axes denoted with P_S and A_S representing the angular difference between the dial reading P for polarizer and analyzer A and plane of incidence. Moreover, the relative attenuation η of the A.C. signal to the D.C. component due to signal processing electronics must be quantified. The Woollam RAE Ellipsometer uses a regression calibration method described in detail in [108].

4.4 Data Acquisition and Modeling

It is recommended to determine the unknown optical properties of bulk samples outside a cryostat first, because the effect of cryostat windows on the polarization state mix with the sample Δ-offset which makes a special calibration procedure necessary (see next section). Moreover, data can be acquired over a large range of angles of incidence and orientations by using a rotation unit, allowing for the measurement of well defined sample orientations by rotating about the surface

normal. To account for surface effects, those measurements were carried out repeatedly after re-polishing the surface. Since most of the samples are opaque in the spectral range investigated, intensity reflection measurements with p-polarized or s-polarized light were accomplished. Moreover, reflectance measurements from FT-spectroscopy were used as a reference.

4.4.1 Cryostat Measurements

Within the frame of this thesis a liquid-Helium flow cryostat was put into operation which enables measurements at temperatures between 15 K to 600 K. Due to the extreme surface sensitivity of the ellipsometric technique, ultra high vacuum (UHV) is recommended. Our setup reaches configuration reaches a vacuum of 10^{-8} mbar after one day. It turned out however, that this vacuum is not good enough to avoid the creation of thin ice layers during low-temperature measurements due to remaining H_2O vapor in the cryostat [95]. Therefore a bake-out procedure was chosen. For this purpose, heating wires are wrapped around the cryostat flanges. The temperature for bake-out is 400 K. The sample mounted on the cold finger inside the cryostat is heated up, too to avoid depositions of dirt from the inner cryostat surface on the sample surface. It turned out that after two days bake out and one day cool down, it is possible to reach a vacuum of 10^{-10} mbar. The samples are cooled down to 10 K first and then heated up slowly. If the heating current is too high the sample and the cold finger will issue vapor while being heated which could lead to the breakdown of the vacuum.

Window-Effects

If a cryostat is used, special care has to be taken of the effects of the entrance and exit windows on the measurement results. Strain can affect the polarization state of the light beam which should not be mixed with the effects of the sample. One way to deal with the problem is to use strain-free windows. However, we used WVASE script supplied by the J.A. Woollam company that accounts for the polarizer and analyzer azimuths as described before and the window effects, separating them into in-plane and out-of-plane effects. The out-of-plane effects or Ψ offset will be determined during the calibration process. The in-plane effects however, mix with the samplet's ellipsometric Δ parameter. Therefore, a reference sample (in our case a silicon wafer) has to be measured without windows to determine surface layers and an adequate model has to be built. The measured data are then fitted to the model, only varying the surface thickness. This can be checked afterwards for accuracy. The window-fitting procedure has to be carried out each time the windows have been changed and in our case every time after bake out.

This section shall give an insight into the data analysis procedure in ellipsometry. It is arranged to lead through the dispersion-model based multi-sample data analysis of generalized ellipsometry data measured within the frame of this thesis.

4.4.2 Extracting the Complex Dielectric Function

For ideal isotropic bulk samples it would in principle be possible to directly invert n and k from the measured Ψ and Δ values with equation 3.57 and the Fresnel equations. However, this is an idealization that is difficult to achieve for bulk samples unless they are cleaved in-situ. Otherwise there will always be native oxide-layers, surface roughness or adsorption of dirt due to processing. For more complicated bulk structures with unknown and/or multiple surface layers or gradients in optical constants, a more advanced data analysis is necessary. As it turns out, it can be a quite difficult task to find a unique solution for the optical constants if there are so many unknowns. Unique means that only one combination of fit parameters will lead to the best solution (smallest Mean Squared Error (MSE)). One problem here is that parameter correlations occur, e.g. optical constants and film thickness are not independent from each other. It is, for example, not possible to define the film thickness of a thin film film on a glass substrate by one VASE measurement only. Additional information from transmittance data must be added for de-correlation of the fit parameters. Another possibility is to simultaneously fit repeated measurements of one sample. In general, a parametric dispersion model is used to calculate n and k or ε_1 and ε_2 as a function of wavelength. The most famous examples is the Lorentz oscillator model that has the advantage of being Kramers-Kronig consistent. Another dispersion model is the Cauchy model which, however, is valid only for transparent materials. The WVASE offers many more models to account for any special case like Tauc-Lorentz which is used for oscillators in the gap region. It is also possible to use a sum of Gauss functions to describe the dataset.

Another, however not Kramers-Kronig consistent fit procedure is to define the optical constants of a bulk sample in the transparent region with a Cauchy model, by set $k = 0$ and then fit for n. Then with this starting value, a point by point fit is started.

Anisotropic data acquisition

The samples investigated within the frame of this thesis are of orthorhombic symmetry and therefore the dielectric function along all three crystallographic directions has a different complex value. In this case, attention has to be paid to the correct orientation in the measurement process. In principle, it is possible to use the isotropic measurement technique if the samples are aligned correctly along the ellipsometric system since the Jones Matrix then becomes diagonal as described

in the previous chapter. In our group however, we used the general Mueller matrix formalism in order to check for depolarization effects or misalignment which would be signaled by non-zero off diagonal elements. In the general Mueller matrix measurement procedure of the J.A. Woollam company, all single Mueller matrix elements are measured by using different polarizer and retarder positions for each wavelength. For uniaxial samples (e.g. tetragonal or hexagonal symmetry) two independent Mueller matrices have to be measured, i.e. two orthogonal crystallographic directions and optically biaxial crystals (e.g.orthorhombic symmetry) require 3 independent measurements. In our case only the first three rows of the Mueller Matrix are accessible since our system is not equipped with a compensator. The full calculation is derived in the appendix.

How to build a biaxial model

The biaxial model of the WVASE software was designed to model the optical constants of a biaxial crystal and allows to fit two of the Euler angles at the same time. Fitting for all three angles leads to parameter correlation. If the unknown optical

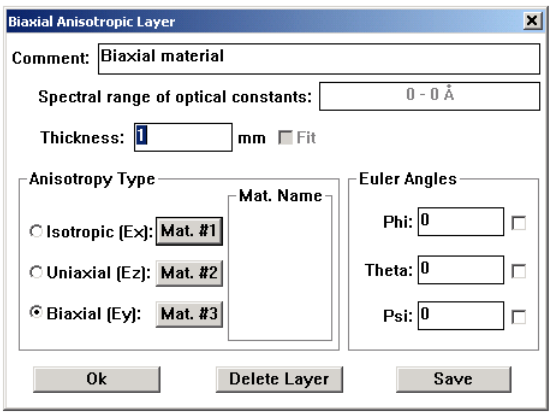

Figure 4.5: Biaxial layer to build a multi-model fit

constants of a biaxial bulk sample shall be determined, we need three material files, as depicted in figure 4.5 denoted with Mat. #1, Mat. #2 and Mat. #3. We used Kramers Kronig consistent Lorentz oscillator models as dispersion-functions for n and k (see figure 4.6). For determining start values for the fit parameters we make use of the above mentioned approximation, that in certain measurement configurations, only one element of the diagonal dielectric tensor contributes most, as was already described by Drude (cite) and later by Aspnes [106]. In a setup like in figure 3.7 the main contribution of the dielectric tensor comes from ε_c. This means we have to measure at least 2 perpendicular surfaces to get information on

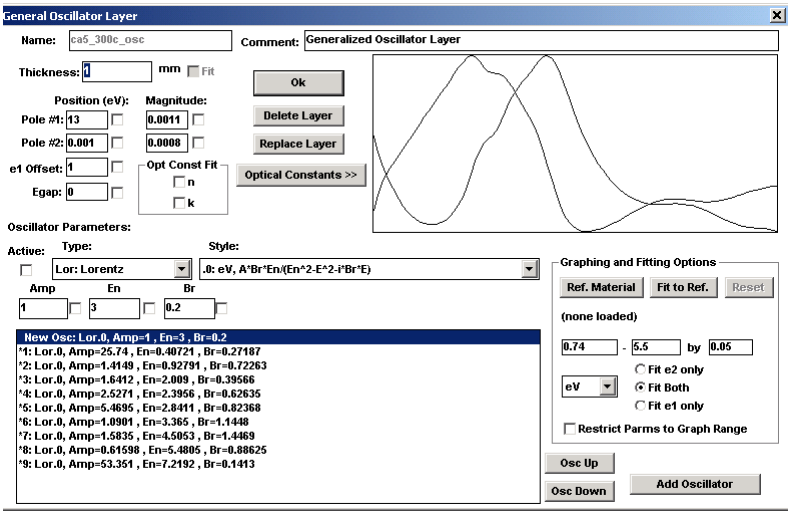

Figure 4.6: Dispersion model based material file. In this case, a Lorentz oscillator model.

all three axes. The idea is to measure the Mueller matrix of the reflectance setup in figure 3.7 and then invert the measured data following equation 3.74 as if we would measure an isotropic sample. The ellipsometric parameters can be inverted with equation 3.57. This leads to a tabulated set of n and k values that can be used as a reference file in the general oscillator layer. We now have an estimate of the optical constants along the one axis. The same is done for the other two material files. One problem with the starting point is that surface layers are neglected in the reference files. The next step is to build up a multi-model fit. In this, all ellipsometric measurement configurations and sample orientations can be fit simultaneously. In our case we used up to 10 data sets including ellipsometric and intensity reflectance types. For each data set a biaxial layer has to be created, taking into account the measurement configuration by adapting the Euler angles. The Material files #1, #2 and #3 are coupled to all those layers. The goal is to find a unique solution to all data sets with the simplest possible model.

4.5 Sample Preparation

Single crystals of the spin-ladder compounds were prepared and characterized by X-ray diffraction by U. Ammerahl and P. Ribeiro. Before sample polishing the orientation was checked in the Laue camera [2]. In case of $Sr_{14}Cu_{24}O_{41}$ the single crystal was investigated with a single-crystal diffractometer. The samples have been

[2] The Laue pictures were were analyzed by orientexpress

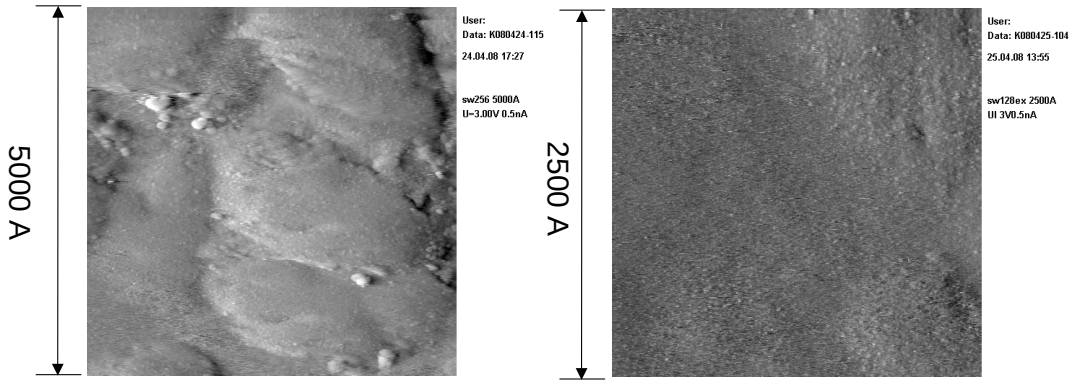

Figure 4.7: STM pictures of $Sr_9Ca_5Cu_{24}O_{41}$. The left panel shows the polished surface before Xe-ion sputtering and the right panel after sputtering. The surface roughness is of the order of 100 Å.

lapped with a 3 micron Al_2O_3 water suspension (Logitech) and thereafter polished to optical grade with 0.5 micron SiO_2 polishing suspension SF1 (Logitech). The surface was checked in a polarization microscope. For low-temperature measurements, the samples were cleaned in several ultrasonic baths with acetone (3 min.), ultrapure water (3 min.), methanol (3 min.), and again ultrapure water (3 min.). After the last ultrasonic bath, the sample is put on the Cu cold finger of the cryostat and fixed with silver paint. When dealing with bulk samples, one is confronted with the problem of undefined surface layers from oxidation or contamination. If the optical properties of the bulk sample and the surface layer (and its thickness) are unknown, then it is not possible to find out the true optical constants with one VASE measurement due to parameter correlation as described before. It is necessary to prepare the same surface several times, or measure other samples with the same optical constants, and to take into account intensity transmittance or reflectance spectra. Another influence on the optical properties of the sample is strain put on the sample during the polishing process. The surface might then show other optical properties compared to natural unpolished surfaces. However, in most cases, polishing is needed to ensure high intensity of the reflected beam. In case of rough surfaces, the light is reflected in different directions leading to deviations from the supposed angle of incidence.

4.5.1 Polishing

Figures 4.10 and 4.9 show VASE data of repeated measurements outside the cryostat after repeated sample preparation. The first measurement was done with standard lapping + polishing procedure as described above. The ellipsometric measurements were carried out directly after cleaning and preparation. In order

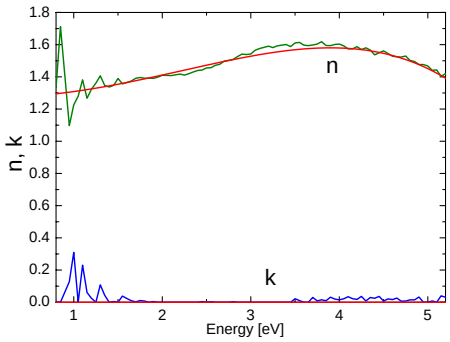

Figure 4.8:
Optical constants of the Cauchy model describing the surface layer. The red lines are n and k values that follow from the Cauchy dispersion model (assuming $k = 0$) and the green and blue data show the values after fitting for n and k.

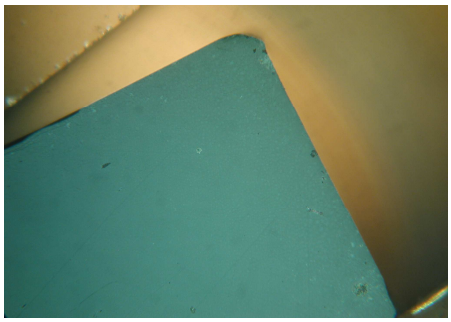

Figure 4.9:
Microscope picture (32x) of $Sr_9Ca_5Cu_{24}O_{41}$. It shows the ab plane after Xe-ion sputtering.

to learn about the influence of surface preparation, in one case the sample was only re-polished. The details of preparation are listed in table 4.2. It is clearly observable that the repeated measurements do not fall together. In case of the ac-plane the variation is only moderate, whereas strong discrepancies are observed in the case of the ab surface. It is not easy to find out about the origin of these effects but we assume that unknown surface layers exist that vary in thickness with each sample preparation. Moreover, the ab surface was much smaller than the ac surface which makes alignment difficult. In one case we did a measurement of the sample surface that was cleaned by Xe-ion sputtering and used this surface as a reference. To identify the bulk properties of the material all repeated measurements were fitted in one multi-model analysis with up to 10 data sets. Then room-temperature data inside and outside the cryostat were fitted in one model. The surface layers were simulated by a Cauchy model assuming a non-absorbing material (see Fig. 4.8). We found layer thicknesses of 1.6 to 1.8 nm inside the cryostat and 3 nm outside the cryostat. The following figure shows the n and k values of the Cauchy model.

4.5.2 Cleaving

In the case of $Sr_6Ca_8Cu_{24}O_{41}$ and $SrCuO_2$ we used the technique of cleaving to measure a sample without any further polishing or cleaning. The spin ladders cleave perpendicular to the b axis. However, the resulting surface can show steps and only small reflecting parts. Therefore the intensity at the detector may become

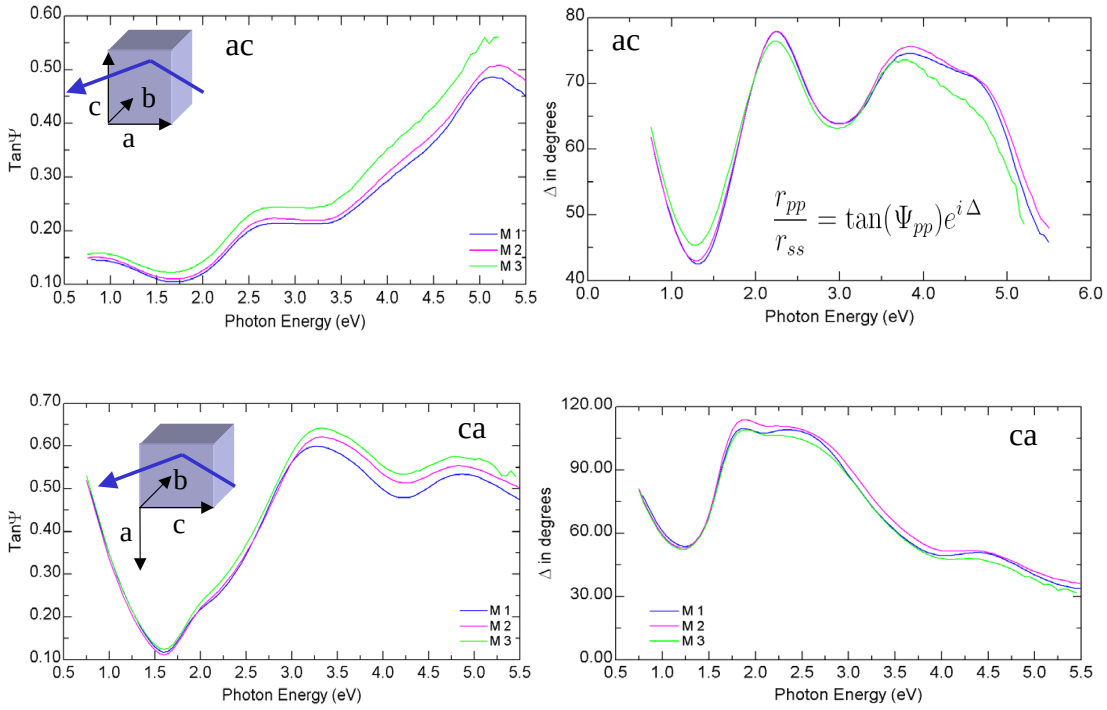

Figure 4.10: Repeated ellipsometric measurements of the *ac* surface of $Sr_9Ca_5Cu_{24}O_{41}$ for two different orientations and after repeated sample preparation. The data were acquired without cryostat.

Surface	Measurement	Preparation
ac/ca	M1 (blue)	lapped + polished
ac/ca	M2 (magenta)	lapped + polished
ac/ca	M3 (green)	re-polished
ab/ba	M1 (blue)	lapped + polished
ab/ba	M2 (magenta)	re-polished
ab/ba	M3 (green)	lapped + polished
ab/ba	M4 (red)	lapped + polished + Xe-ion-sputtering

Table 4.2: Table of repeated sample preparations for $Sr_9Ca_5Cu_{24}O_{41}$ (see Figs. 4.10 and 4.11).

a problem. Moreover, it is difficult to control the size of the parts that break away and the sample can be destroyed. Our sample broke into two equally sized pieces and the *ac* surfaces turned out to show little steps which however were reflecting well enough to be used in a VASE measurement. Although the intensity at the detector was quite low, we achieved satisfying results by doing many measurements at each wavelength (up to 1000 revolutions per measurement). The data were acquired at room temperature without cryostat, and also one low-temperature

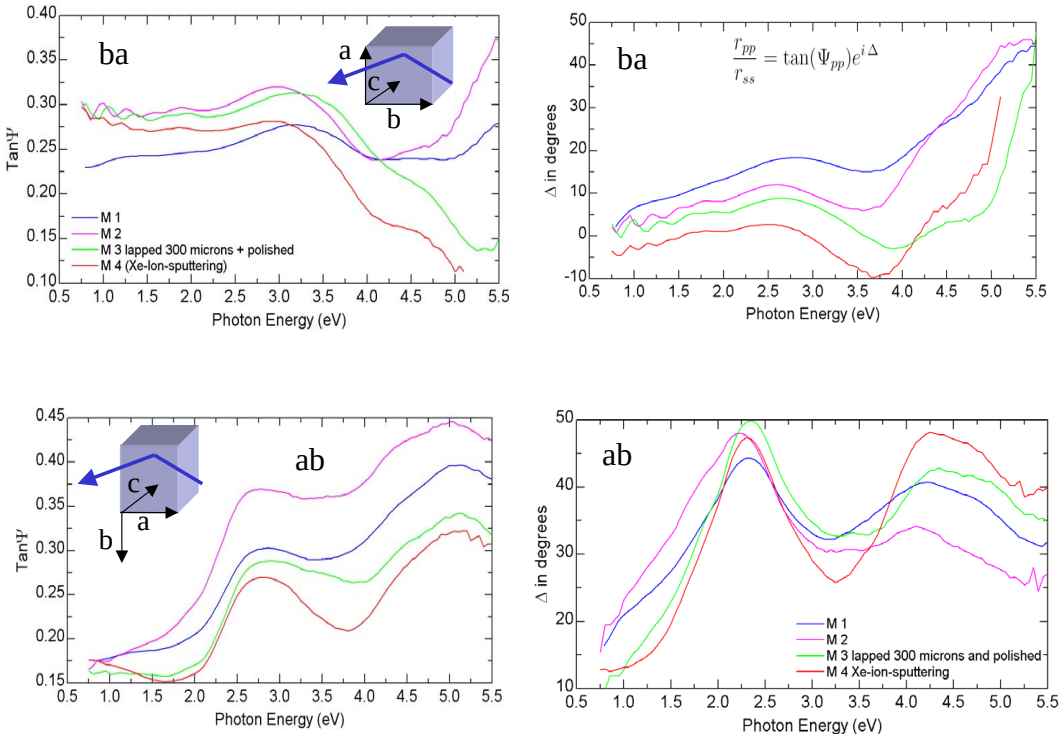

Figure 4.11: Ellipsometric measurements of the *ab* surface of $Sr_9Ca_5Cu_{24}O_{41}$ after repeated standard sample lapping and polishing and in one case after Xe-ion sputtering. The data were collected at room temperature.

measurement along the *c* axis was done to check the temperature dependence. After that the data were modeled in a multi-model fit with polished samples.

In Fig. 4.12 and ellipsometric parameters of the polished and cleaved surface are compared. It can be stated that the surface layers or strain effects due to polishing do somewhat affect the line shape, e.g. the shoulder at 2.0 eV is better resolved at low temperatures in the cleaved sample. This comparison however shows that we indeed observe bulk properties of the sample in both cases. We assumed different models for the surface like the Cauchy dispersion model and surface roughness layer. The best fit was reached for a model that assumes no surface layer for the cleaved samples and 2 to 7 nm Cauchy surface layer on the polished samples. To check for the temperature dependence, also a model fit without any surface layers on top was carried out. It turned out that the relative temperature dependence stays the same. However the total spectral weight can vary.

In Figure 4.13, the optical conductivity data along the c axis (chain/ladder-direction) is shown for $Sr_{14}Cu_{24}O_{41}$ as a function of temperature. The upper panel shows the result of a multi sample analysis of repeated measurements where the best fit was achieved when assuming a non-absorbing, so-called Cauchy-model surface layer on top. We assumed 3-5 nm layer thickness. The lower panel shows

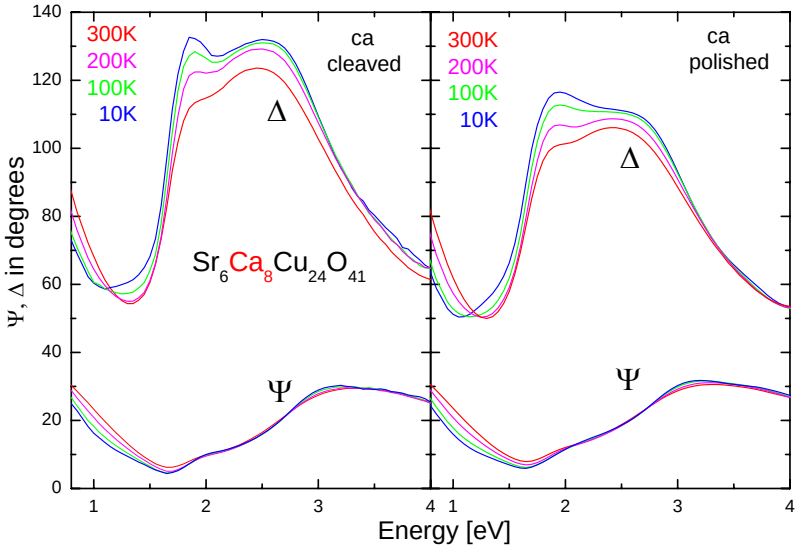

Figure 4.12: Ψ and Δ values of the *ac* surface of $Sr_6Ca_8Cu_{24}O_{41}$ as a function of temperature. The left panel shows data of the cleaved surface. The right panel shows the polished surface.

the result if no surface layer is assumed. Obviously, a surface layer strongly affects the spectral weight of the excitations especially the strong excitation at 3.8 eV. The peak positions are affected too but only slightly. They shift to slightly lower energies by 0.5 eV. The qualitative temperature dependence is not affected. Moreover, we definitely observe bulk properties of the samples which has been proven by comparison of the cleaved sample in case of x=8. In Fig. 4.14 digitalized optical conductivity data of $Sr_{14}Cu_{24}O_{41}$ by Osafune *et al.* [86] are shown which were derived by Kramers-Kronig transformation of normal-incidence reflectance data. Our optical conductivity data from the pseudo-dielectric function from the anisotropic multi-sample with 3-5 nm Cauchy-layer are plotted into the graph for comparison. The results of our ellipsometric measurements on the spin ladder compounds $(La,Sr,Ca)_{14}Cu_{24}O_{41}$ are presented in chapter 5.

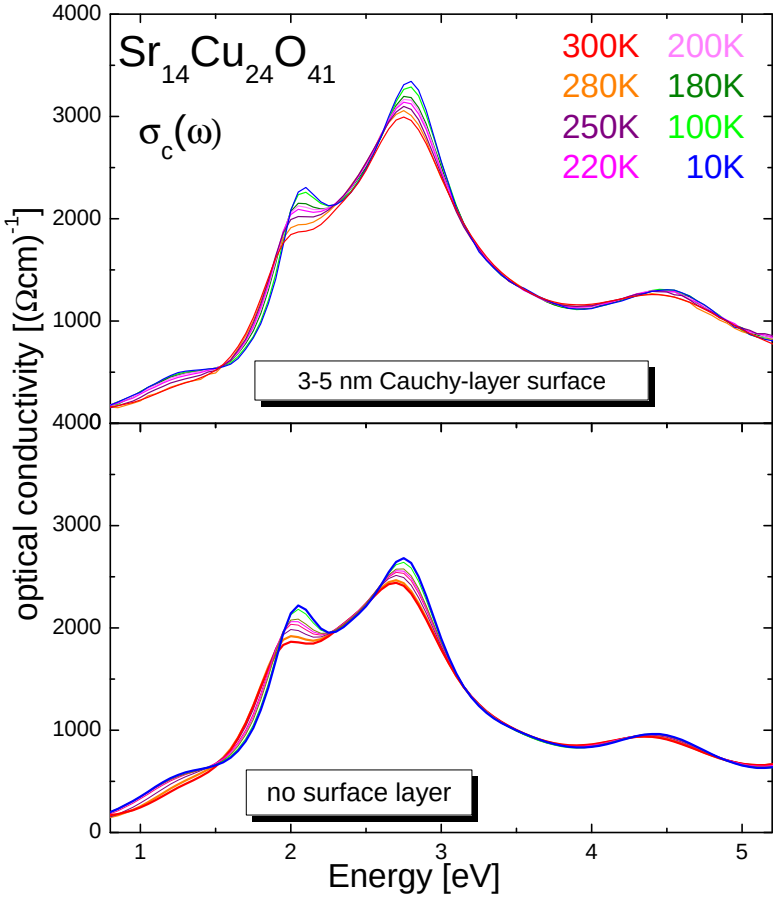

Figure 4.13: Optical conductivity data from ellipsometric measurements for $Sr_{14}Cu_{24}O_{41}$ (x=0) along the chain or ladder direction (c). The upper panel is the result of a multi-sample analysis of repeated measurements leading to a non-absorbing surface layer of 3-5 nm on top of. Those were kept constant at low temperatures. The second panel shows the results for a model without any surface layer to show the effect of surface layers on peak positions and spectral weight.

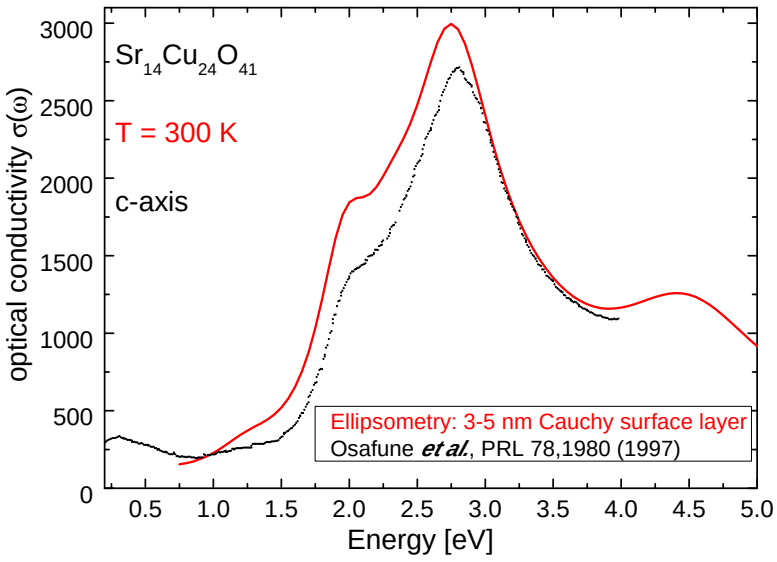

Figure 4.14: Real part of the optical conductivity of $Sr_{14}Cu_{24}O_{41}$ at T = 300 K by ellipsometry and comparison with digitalized optical conductivity data from Osafune *et al.* [86].

5 Ellipsometry and Fourier Spectroscopy on $(La,Sr,Ca)_{14}Cu_{24}O_{41}$

5.1 Physics of $(La,Sr,Ca)_{14}Cu_{24}O_{41}$

Ellipsometric measurements were carried out in the energy range between 0.8 and 5 eV in order to investigate the nature of electron-hole excitations as a function of hole doping, Ca substitution and temperature. The optical conductivity was calculated from $\varepsilon_1(\omega)$ and $\varepsilon_2(\omega)$ determined by ellipsometry for $La_{5.2}Ca_{8.8}Cu_{24}O_{41}$ (LCO) with 0.2 holes per formula unit (f.u.) and the hole-doped compounds (6 holes per f.u.) $Sr_{14-x}Ca_xCu_{24}O_{41}$ with x = 0 (SCO), 5, and 8 (SCCO).

Optical conductivity data calculated from reflectance data between 10 meV - 2 eV from Kramers-Kronig transformation were combined with the ellipsometric data to derive the optical conductivity over the complete energy range comprising low-energy and high-energy excitations. In addition, the spectral-weight transfer was analyzed as a function of temperature and Ca substitution. The aim of this work is to get more insight into the charge-carrier dynamics as a function of temperature and doping.

Crystal Structure of $Sr_{14-x}Ca_xCu_{24}O_{41}$ (SCCO)

The crystal structure of LCO and SCCO is orthorhombic and consists of alternating layers of CuO_2 chains and Cu_2O_3 ladders that are sandwiched by Sr and Ca ions which belong to the ladder subunit (see Fig. 5.1). The structure is incommensurate, namely there is a slight mismatch in lattice constants of ladders and chains along the chain direction [38].

In $Sr_{14}Cu_{24}O_{41}$ (SCO) for example, the lattice constant c_C of the chain subunit is 2.749 while c_L is 3.931 for the $Sr_2Cu_2O_3$ subcell containing the ladders [38]. However, a large average unit cell can be found with a lattice constant $c^* = 27.501$ which is equivalent to $10 \times c_C$ and $7 \times c_L$. As illustrated in figure 5.2, the chains are formed by edge-sharing CuO_4 plaquettes leading to a nearly 90° ferromagnetic (FM) Cu-O superexchange coupling. In this case the O $2p_\sigma$ orbital hybridizing with the Cu 3d orbital is almost orthogonal to the neighboring Cu 3d orbital,

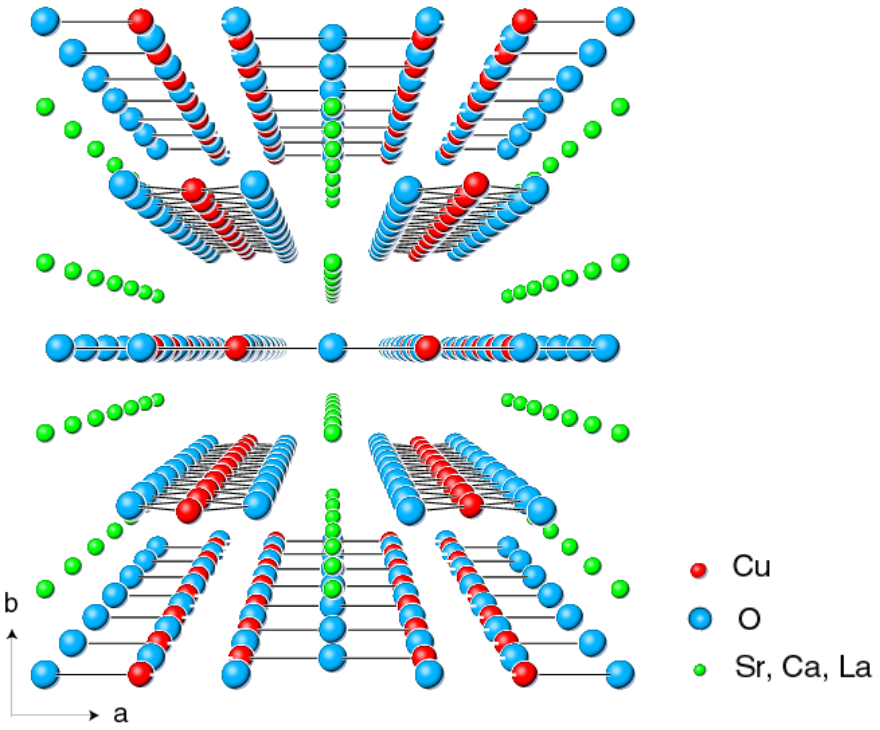

Figure 5.1: Crystal structure of LCO and SCCO. The chain and ladder subsystems are stacked along the crystallographic b direction. The layers are sandwiched by Ca, La, and Sr ions.

hence charge-carrier hopping along the chains is suppressed. The ladder legs and rungs are formed by corner-sharing CuO_4 plaquettes with strong antiferromagnetic (AF) superexchange coupling. Hopping along those directions is favored. Between two ladders, a weak ferromagnetic coupling due to edge-sharing plaquettes plus frustration leads to a very weak coupling among two neighboring ladders.

Electronic structure of $Sr_{14-x}Ca_xCu_{24}O_{41}$: charge-density waves vs. superconductivity

$Sr_{14-x}Ca_xCu_{24}O_{41}$ is inherently doped with six holes per formula unit. For x = 0 the system shows semiconducting behavior and upon substitution of Sr by isovalent Ca the conductivity rises [9–11], see Fig. 5.3. The rise in conductivity with Ca substitution was interpreted in terms of a redistribution of holes from chains to ladders [9, 86, 90]. Optical conductivity data as well as DC conductivity data show a strong anisotropy between a and c direction [11], e. g. charge-carrier propagation parallel to the legs of the ladder is about 10 times higher than along the a direction which is parallel to the rungs. This means propagation between

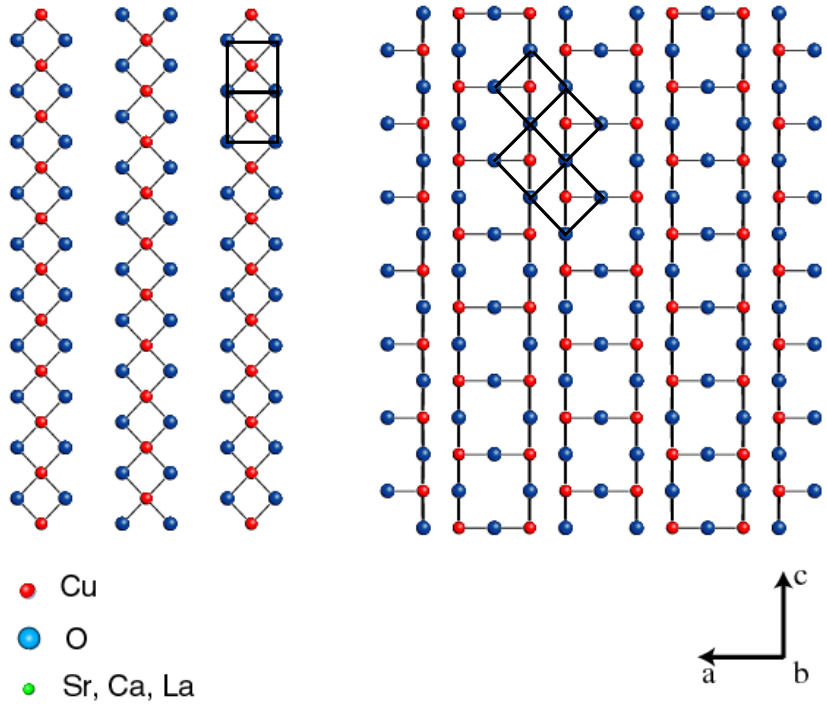

Figure 5.2: Top view of chain and ladder units. The crystallographic c direction is defined along the legs or chains, respectively. The a direction is defined along the ladder rungs. The corner-sharing or edge-sharing CuO_4 building units are highlighted by black squares.

neighboring ladders is strongly suppressed. In 1992, Dagotto *et al.* [5] predicted d-wave superconductivity for the slightly hole-doped two-leg spin ladder emphasizing the analogy to the 2D cuprates. In the hole-doped case, the physics is described within the t-J model. In the strong-coupling limit $J_\perp \gg J_\parallel$, the ground state at half filling consists of a set of spin singlets on each rung of the ladder. A spin gap of the order of $J_\perp$ is predicted [5]. In case of doping of two holes, it is magnetically favorable to break only one singlet, placing the two holes close to each other. At the same time, one has to consider the Coulomb repulsion between the holes and that the kinetic energy is enhanced for a pair. However, in a certain parameter range, the pair-binding tendency dominates. The hole-pair binding energy is of the order of $J_\perp$. The discovery of superconductivity in SCCO for x>13.6 under high pressure [12] was interpreted as a confirmation of Dagottot's theory.

In the high-T_C cuprates, it can come to a competition between superconductivity and charge-ordered phases that are regarded as instabilities of the normal phase. For example, in the 2D planes of the HTSC materials a stripe-ordered phase competes with superconductivity [109]. In principle, there are three mechanisms

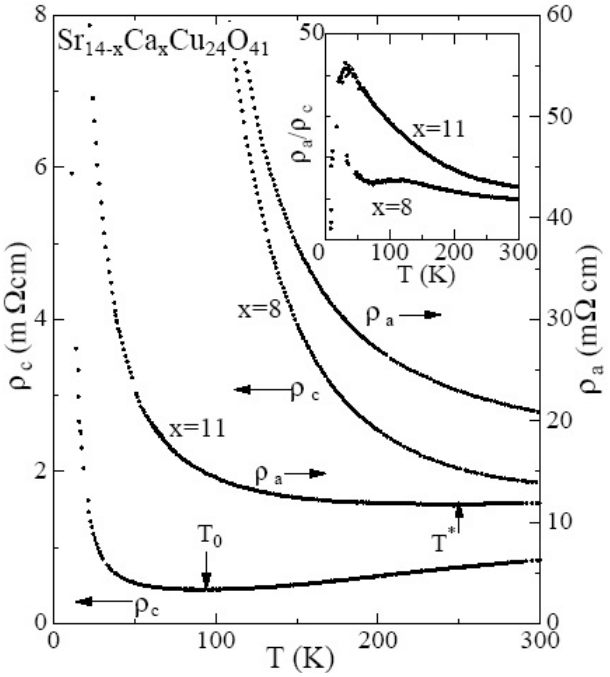

Figure 5.3: Temperature and doping dependence of the DC resistivity of $Sr_{14-x}Ca_xCu_{24}O_{41}$. The resistivity is strongly anisotropic, i. e., along the chain and leg direction c it is an order of a magnitude smaller than along the a or rung direction. For x = 11, the samples show metallic behavior at elevated temperatures in both directions.[11].

that stabilize a charge-density wave (CDW). Those are a) long-range Coulomb interaction (or intersite interaction if long-range Coulomb interaction is screened as in the copper oxides [110]), b) a Peierls instability [19], or c) charge-stripe formation in the single-band t-J model [5]. Apart from superconductivity, signatures of charge ordering and charge-density waves have been reported in SCCO by several experiments that are summarized here. Still, the exact nature of these states is unresolved. It seems however, that it is directly related to the distribution of holes in the chain and ladder subsections.

The question where the holes are located is discussed very controversially in the literature and new investigations [113] are puzzling. On the one hand, an early investigation of $Sr_{14-x}Ca_xCu_{24}O_{41}$ by polarized x-ray absorption spectroscopy (XAS) reported that most of the 6 holes reside in the chains for x=0 and that there is only a slight transfer with Ca doping [114]. On the other hand, an analysis of the spectral-weight transfer in the optical conductivity $\sigma(\omega)$ with Ca substitution by Osafune *et al.* [86] found a larger transfer of holes from ladders to chains with Ca substitution, explaining the decrease in resistivity with rising x. In $Sr_{14}Cu_{24}O_{41}$

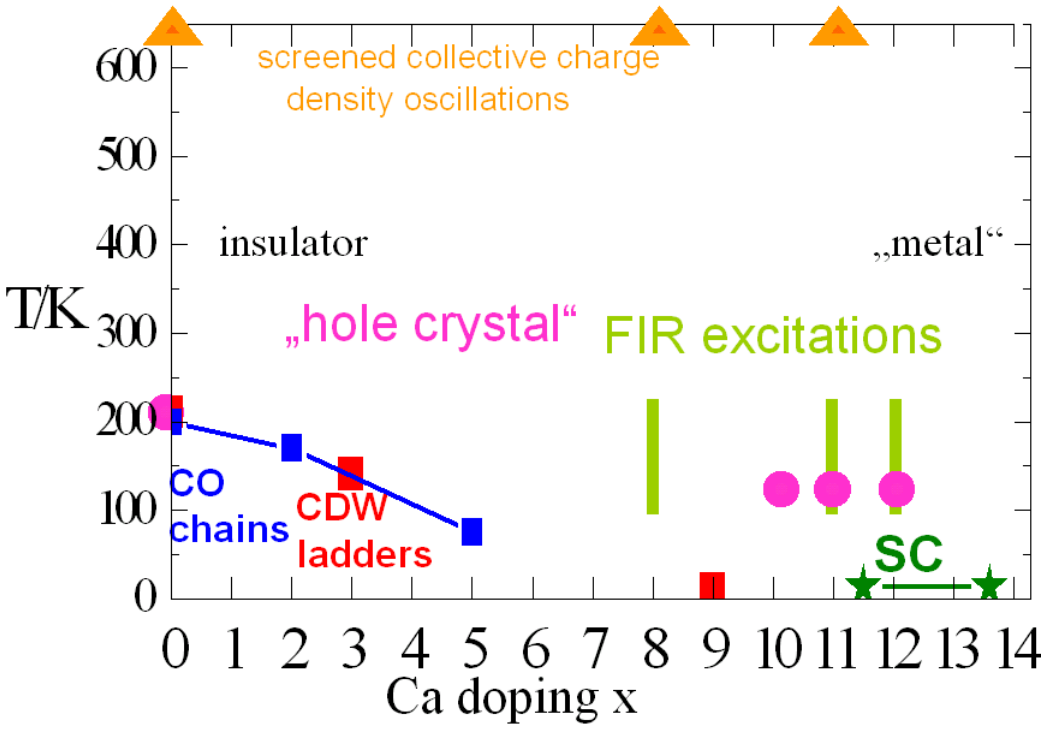

Figure 5.4: Qualitative phase diagram giving an overview of experimental results in $Sr_{14-x}Ca_xCu_{24}O_{41}$ as a function of Ca substitution. We begin on the left side with x=0 in the insulating region. In SCO (x = 0) charge ordering (CO) was reported [10, 111] for the *chain* subsystem with a charge-ordering temperature of 220 K. Moreover, a charge-density wave has been reported [15] in the *ladders* of SCO with comparable transition temperature. The CO (blue squares) and CDW (red squares) phases are suppressed with rising Ca content. Recently a RIXS study [17, 18] reported a hole-crystal (HC) for x = 0 ($T_C \sim 200$ K), and also for high Ca contents at x = 10, 11, and 12 (pink dots). In the "metallic" region, superconductivity (SC) under pressure was reported [12] (green stars). The green vertical bars signal the doping levels where a still unresolved broad excitation in the FIR absorption spectra along the a (rung) direction [11, 20] is observed. In addition to that, charge density oscillations were reported by [13, 112] at high temperatures in low and high doping levels (orange triangles).

($x = 0$) signatures of charge ordering were reported by inelastic neutron scattering [115–117] at temperatures below T=200 K. This charge ordering was assigned to the *chain*. The doped holes were supposed to be in Zhang-Rice singlet states. In this picture, spin dimers are created by AF coupling of Cu spins via Zhang-Rice singlets. Evidence for a dimerized state was provided by measurements of the magnetic susceptibility where a spin gap was reported [10, 111]. This observa-

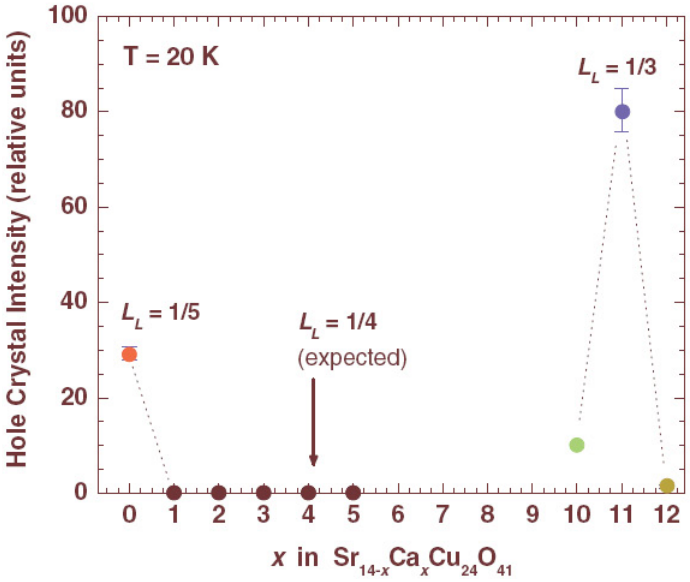

Figure 5.5: Intensity of hole-crystal scattering in $Sr_{14-x}Ca_xCu_{24}O_{41}$ for $x = 0, 1, 2, 3, 4, 5, 11$, and 12 [18]

tion is in contrast to the behavior of the 1D $S = 1/2$ Heisenberg chain where no spin gap is expected in the undoped case, as described in the previous chapter. Measurements of the thermal expansion also supported a charge-ordering scenario [118]. Recently, a re-investigation by XAS spectroscopy [113] depicts a quite different picture. Herein, it is claimed that the number of holes in the ladders is $n_L = 2.8$ and in the chains $n_c = 3.2$ for $x = 0$ at room temperature. This is in strong contrast to the widely accepted assumption that most of the holes reside in the chains for $x = 0$. In the new scenario, the holes are distributed nearly equally among the two subsystems. For $x = 11$, it is claimed that most of the holes reside in the ladder subunit with $n_L = 4.4$ and $n_c = 1.6$ [113]. It shall be noted that the experimental data of [114] and [113] look basically the same, however, the interpretation is different. If this new result holds, many interpretations of the system may have to be revised. Moreover, a study by resonant soft x-ray scattering (RSXS) showed signatures of a hole crystal (HC) in the *ladders* and not the chains with commensurate wave vector $l_L = 1/5$ for $x = 0$ [17]. This picture is supported by transport measurements [13, 14] and Raman scattering [13, 112]. A second RSXS study [18] investigated a large number of Ca levels of $Sr_{14-x}Ca_xCu_{24}O_{41}$ with x = 0,1,2,3,4,5,11, and 12. This study shows signatures of a HC for $x = 0, 10, 11$, and 12 with a commensurate wave vector $l_L = 1/5$ for $x = 0$ and $l_L = 1/3$ for x= 10,11, and 12. The resonance at $x = 11$ is the strongest among them, as seen in figure 5.5. In contrast to Raman scattering results [112], no hole crystal was found in the intermediate doping region, $1 \leq x \leq 5$. A quali-

tative phase diagram of the observed low-energy excitations and ground states is given in Fig. 5.4.

In the case of SCCO, the CDW is referred to as a hole crystal [18] to stress that it is driven by the Coulomb interactions on Cu sites only. The observation of the CDW has inspired Wohlfeld *et al.* [119] to formulate a *d-p* multiband charge-transfer model for the Cu_2O_3 ladder planes of SCCO. It was solved by using the Hartree-Fock approximation. The revised hole distribution [113] for the ladders, $n_h = 1.20$ (number of holes per Cu ion) for $x = 0$, $n_h = 1.24$ for $x = 4$, and $n_h = 1.31$ for $x = 11$ were confirmed. The number 1.20 for x = 0 stands for 1 hole (half filling) + 0.2 holes per Cu ion. The total number of holes in the ladder part of the unit cell can then be calculated by $14 * 0.2 = 2.8$ (14 Cu ions in the ladders and 10 Cu ions in the chain of the unit cell). The calculated CDW periodicity agrees with the experimentally observed one and supports the Coulomb interaction as the driving force [119]. For example, from the measured hole-crystal wave vector of $l_L = 1/5$ (or $\lambda_{HC} = 5 * l_L$) the number of holes per ladder amounts to $14/5 = 2.8$. It is stressed by Wohlfeld *et al.* that the *t-J* model might not be the appropriate model to explain charge-order in the ladders. It is pointed out that the multiband charge-transfer model is more appropriate to describe the physics of the spin ladders because a single Cu_2O_5 ladder has not the D_{4h} symmetry of the CuO_2 planes. This makes the Zhang-Rice derivation of the *t-J* model [43] arguable [119]. In addition, the spin ladders are coupled through on-site Coulomb interactions between holes in different O(2p) orbitals that could lead to new phenomena. The Cu_2O_5 unit cell consists of 2 Cu $3d_{x^2-y^2}$ orbitals

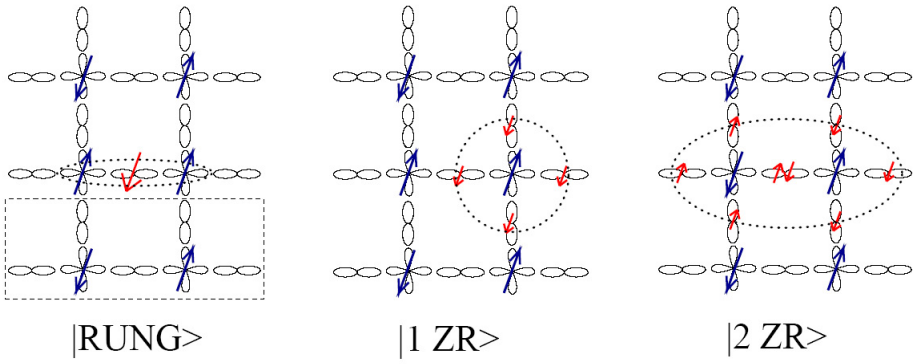

Figure 5.6: Schematic description of a Cu_2O_5 ladder unit with different states for bound holes. The red arrows denote spins of doped holes [119].

(denoted with *d* [119]) on two legs of one ladder, one rung or bridge orbital O $2p_\sigma$, two $2p_\sigma$ orbitals on the legs, and two O $2p_\sigma$ orbitals on the outer part of the rungs (see Fig. 5.6).

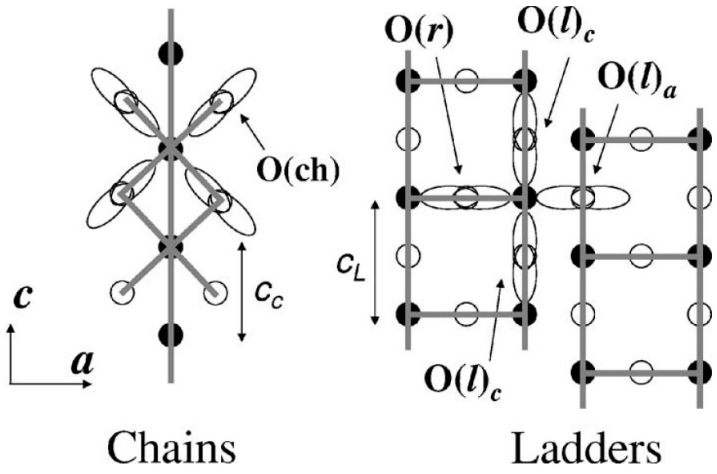

Figure 5.7: Sketch of the ladder and chain subunits in SCCO. In the ladder, three different oxygen sites are identified [113] whereas the oxygen sites in the chains are equivalent.

5.2 Optical Conductivity by Ellipsometry

As described before, ellipsometric measurements on the biaxial crystals on 2 perpendicular surfaces, (010) and (100) or (001) were carried out. Those surfaces were rotated about the surface normal by various angles. The samples were lapped and polished by the described procedure. In one case we measured a cleaved sample on (010) surface. The data acquisition procedure is the so-called general Mueller-matrix mode, provided by the J.A. Woollam company. In this acquisition procedure, several polarizer and retarder positions are measured to determine the full Mueller matrix. The samples were aligned in such a way that the Mueller matrix shows only diagonal elements. Non-zero off-diagonal elements give insight into depolarization or window effects. Those data were analyzed in a multi-model and multi-sample fit to evaluate the complex dielectric function $\varepsilon(\omega)$ or optical conductivity $\sigma(\omega)$ for example.

In this section the optical conductivity $\sigma_1(\omega)$ is presented for the compound $La_{5.2}Ca_{8.8}Cu_{24}O_{41}$ (LCO) with 0.2 holes per formula unit (f.u.) and the hole-doped compounds (6 holes per f.u.) $Sr_{14-x}Ca_xCu_{24}O_{41}$ with x = 0 (SCO) and x = 5, and 8 (SCCO). The measurements were carried out at temperatures between 10 K and 300 K along 4 different crystallographic directions to get information on the optical conductivity of the three principal axes. The change in the absorption spectra of undoped and hole-doped compounds as well as of the different Ca dopings should give an insight into the character of the excitations. To further evaluate the individual excitations within the spectra, we assume that the spectrum can be described by a sum of Lorentz oscillators [91]:

$$\varepsilon(\omega) = \varepsilon_\infty + \sum_j \frac{\omega_{p,j}^2}{\omega_{0,j}^2 - \omega^2 - i\gamma_j\omega} \tag{5.1}$$

where the parameters $\omega_{0,j}$, $\omega_{p,j}$, γ_j, and ε_∞ represent peak frequency, plasma frequency, damping of the jth oscillator and the dielectric constant at infinite frequency, i.e., well above the measured region. The spectral weight of one Lorentz oscillator is related to the square of the plasma frequency as follows:

$$N_{eff} = \frac{2mV}{\pi e^2} \int_0^\infty \sigma_1(\omega) d\omega = \frac{mV\omega_p^2}{4\pi e^2}. \tag{5.2}$$

Here, m is the effective mass of the electron ($m = m_e$), V is the volume of the unit cell per Cu [1] ion that contributes to this particular oscillator, e is the electron charge, ω_p the plasma frequency, and $\int_0^\infty \sigma_1(\omega)d\omega$ is the spectral weight. The advantage of equation 5.1 is its Kramers-Kronig consistency. In our case, we will see, however, that the optical spectra show band structure and excitonic effects rendering a fit with a pure Lorentz model difficult. Sometimes a Gauss function or a Tauc-Lorentz function at the band edge better describe the shape of the absorption features.

Fig. 5.8 shows the real part of the optical conductivity of the hole-doped compounds along the b direction, $\sigma_b(\omega)$, perpendicular to the layers of chains and ladders (compare Fig. 5.1). All spectra look basically the same, there is one high-energy absorption feature with its center above 5 eV which is more or less temperature independent. For LCO no absorption is observed in this energy range.

Figures 5.9 and 5.10 show the optical conductivity $\sigma_a(\omega)$ along the rung direction, and $\sigma_c(\omega)$ along the chain and ladder direction, for LCO (upper panel) followed by the the results for SCO (x = 0) and SCCO (x = 5, 8). At first sight, $\sigma_a(\omega)$ shows two major absorption peaks between 2 and 5 eV in all four compounds which do not strongly change with Ca content or hole doping. $\sigma_c(\omega)$ shows up to four major absorption peaks between 1 to 5 eV, (labeled A, B, C, and D) this time with a pronounced dependence on hole doping, temperature and Ca content. In accordance with DC measurements [9–11] and our own reflectance measurements, a Drude weight from free-carrier contribution is observed with rising Ca content in $\sigma_a(\omega)$ and more pronounced in $\sigma_c(\omega)$. Figure 5.11 gives an overview on $\sigma_a(\omega)$ and $\sigma_c(\omega)$ for all different Ca dopings at T = 10 K and T = 300 K.

The comparison nicely shows that in principle, very similar absorption peaks are observed in $\sigma_a(\omega)$ (left panel) or $\sigma_c(\omega)$ (right panel). A strong change happens with hole doping (from LCO to SCO). For example, the intensity of peak **C** around 2.8 eV in $\sigma_c(\omega)$ is much lower in the undoped LCO (black line) than in the

[1] For SCCO V = 1/24 (a * b * c) with $a = 11.456$, $b = 13.361$, $c = 27.487$

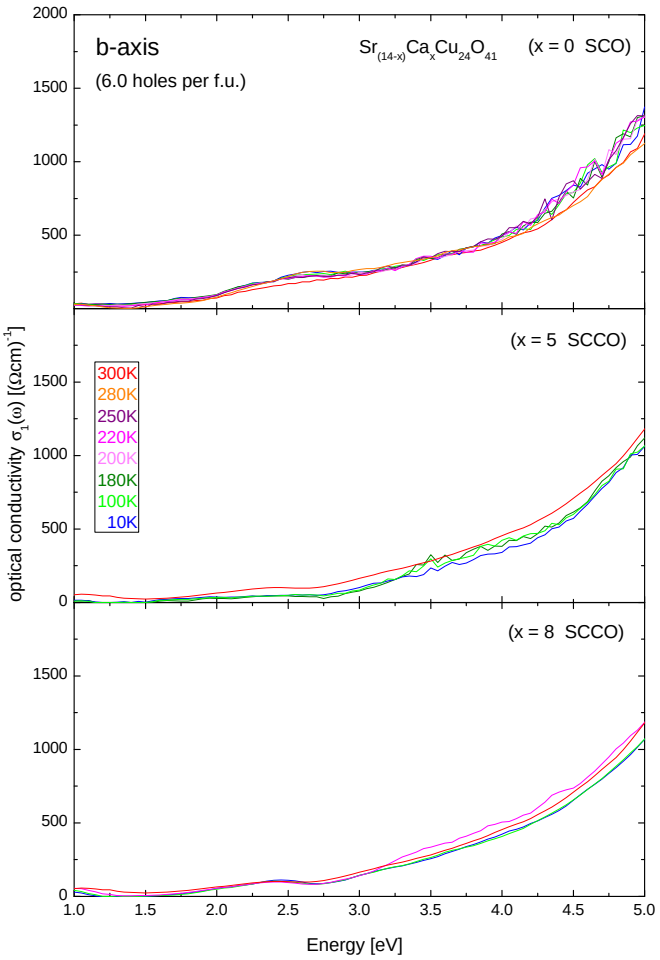

Figure 5.8: Temperature dependence of the optical conductivity of $Sr_{14-x}Ca_xCu_{24}O_{41}$ for (x=0, 5, and 8) parallel to the stacking direction b, perpendicular to the chains and ladders.

SCCO compounds (blue for x = 0, magenta for x = 5, and orange for x = 8). The high-energy absorption between 4 and 5 eV is sharper in LCO but situated at lower energy than in the hole-doped regime. Moreover, all hole-doped compounds show a much more pronounced temperature dependence in $\sigma_c(\omega)$. Especially the shoulder peak **B** around 2.0 eV in $\sigma_c(\omega)$ is strongly affected by changes in temperature or Ca content.

5.2.1 Drude-Lorentz fit

A quantitative determination of the change in spectral weight of the individual excitations requires a more detailed investigation. Therefore, a Drude-Lorentz fit

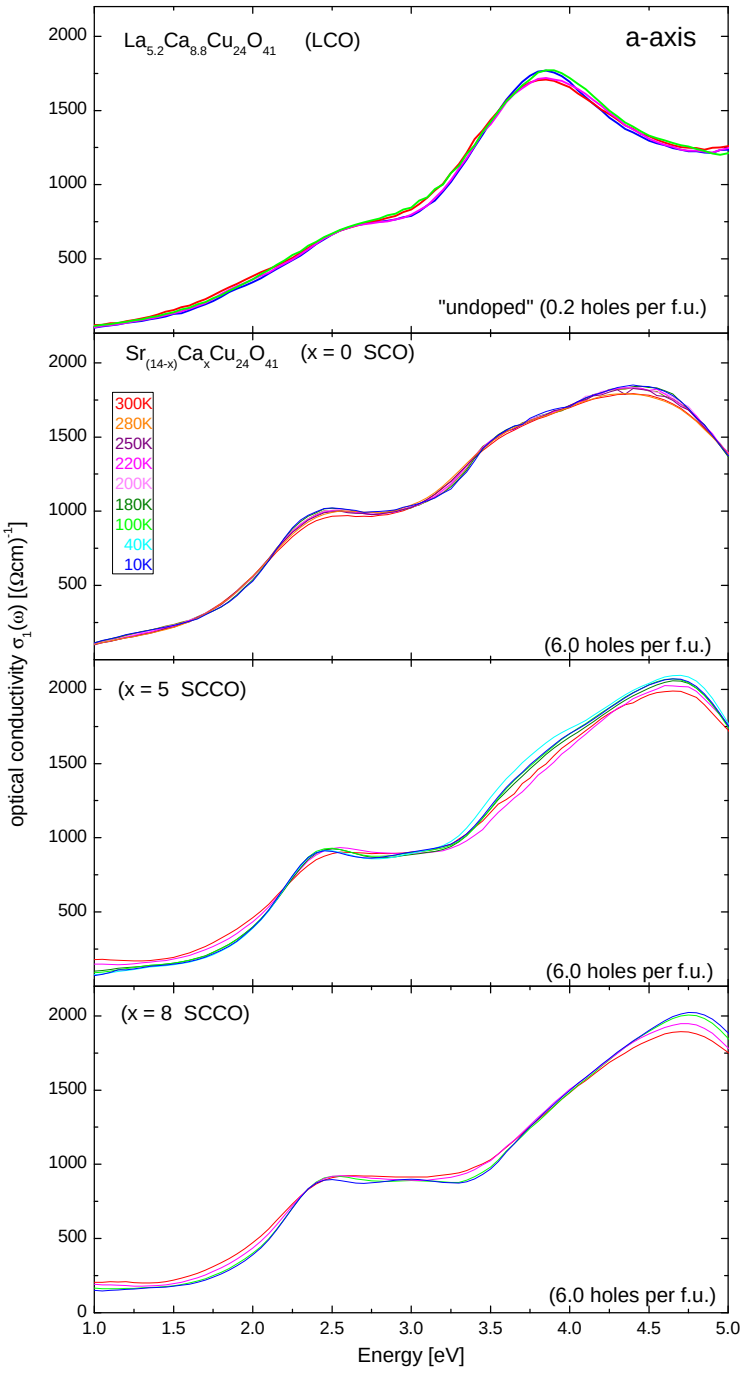

Figure 5.9: Temperature dependence of the optical conductivity of $(La,Sr,Ca)_{14}Cu_{24}O_{41}$ parallel to the rung direction of the ladders (a direction)

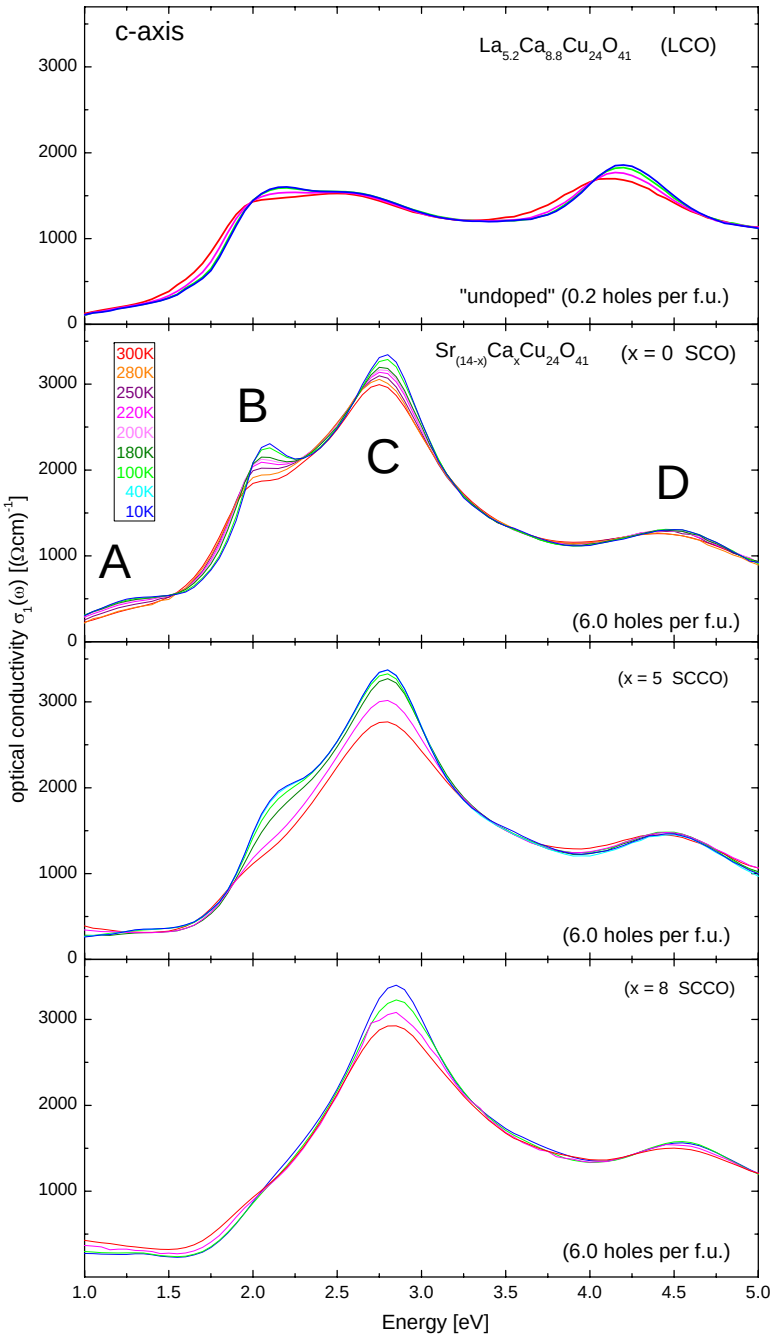

Figure 5.10: Temperature dependence of the optical conductivity of $(La,Sr,Ca)_{14}Cu_{24}O_{41}$ along the chain or ladder direction (c).

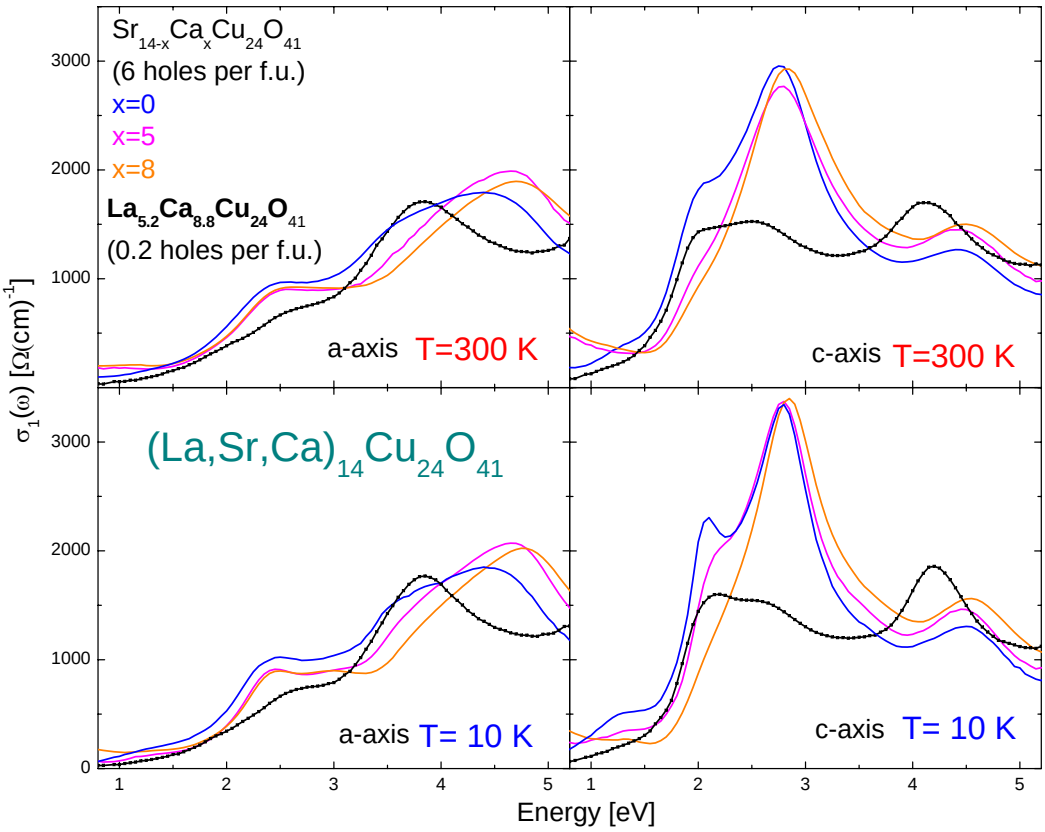

Figure 5.11: Optical conductivity spectra $\sigma(\omega)$ parallel to a and c of $(La,Sr,Ca)_{14}Cu_{24}O_{41}$ at T = 300 K and T = 10 K are plotted together to compare the excitation spectra of insulating and hole doped compounds.

is carried out and the parameters ω_p^2 (as a measure of the spectral weight), the peak frequency, ω_0, and the broadening γ are listed for the main excitations as a function of temperature and doping. Fig. 5.12 shows exemplarily the Drude-Lorentz fit at 10 K and 300 K for SCO along the a axis. Since no pronounced temperature dependence is observed, we do not list the fit parameters as a function of temperature. In Fig. 5.12 we show that at least three Lorentzians centered at 2.4 eV, 3.6 eV, and 4.5 eV (T = 10 K) are needed to describe the spectrum of SCO along a. Next, the Drude-Lorentz fit for the optical conductivity along c for all compounds is shown in Fig. 5.13. In our first approach, six Lorentz oscillators were used to fully describe the data. This is shown in Fig. 5.14. A high number of Lorentz oscillators of course describes the data very well. However, then the parameters (ω_0, γ, and ω_p) will be strongly correlated, which renders a clear statement concerning temperature dependence of the parameters difficult. Therefore, a

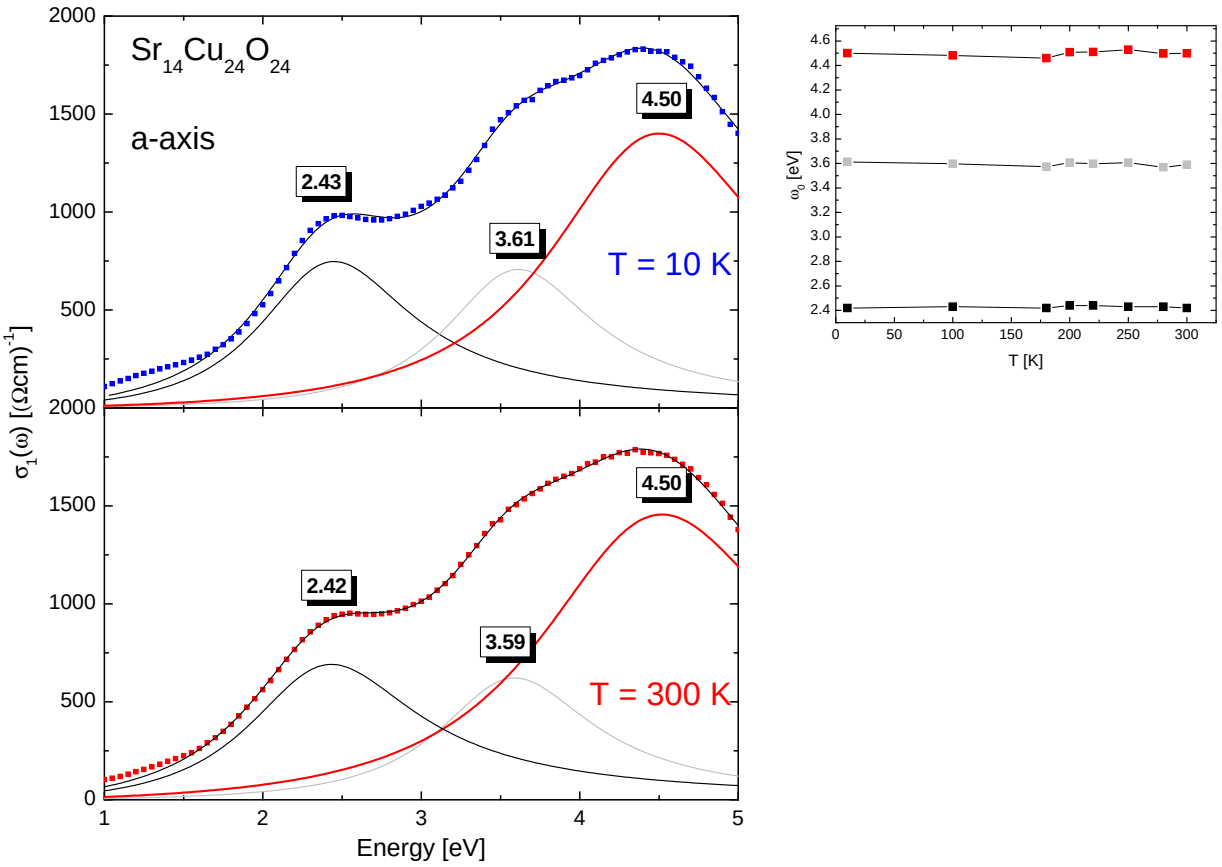

Figure 5.12: Optical conductivity spectra $\sigma(\omega)$ parallel to a (rungs) of $Sr_{14}Cu_{24}O_{41}$ at T = 10 K and T= 300 K with Lorentz-oscillators fitted to the spectrum. The panel on the right shows the peak positions of the three absorption peaks as a function of temperature.

minimal model was assumed for the analysis of $\sigma_c(\omega)$ with four Lorentz oscillators (labelled A,B,C, and D) for the main absorption peaks in the spectrum as shown in Fig. 5.13. Four oscillators describe the spectrum well and parameter correlation is minimized. Table 5.1 lists the peak frequencies ω_0 found by the Drude-Lorentz fit at T = 10 K in $\sigma_a(\omega)$ and $\sigma_c(\omega)$ for all compounds. Still, it turns out that an exact determination of the spectral weight shift of the individual excitations with a Drude-Lorentz fit is difficult because of the non-Lorentzian shape of the peaks. The reason for this are band structure or excitonic effects. Moreover, the parameters are still slightly correlated. Therefore, we additionally integrate over the conductivity following the partial sum rule to evaluate the shift in spectral weight with temperature (see below).

Starting with the high-energy excitations, we are now comparing the positions

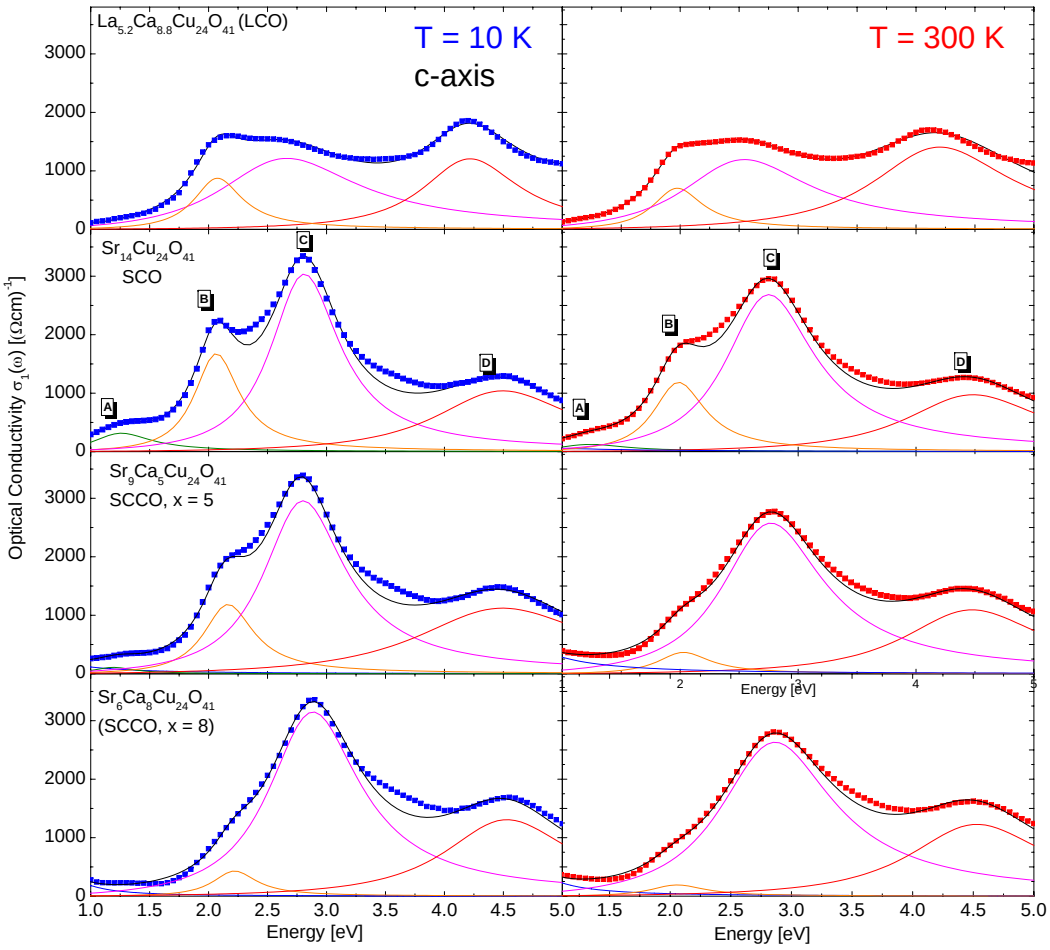

Figure 5.13: Optical conductivity $\sigma(\omega)$ parallel to c of all compounds at T = 10 K and T = 300 K with a minimal Lorentz-oscillator model fitted to the spectrum.

of our observed peaks with the model predictions of Moskvin *et al.* [60, 71, 78] and experimental results in the 1D and 2D systems summarized in chapter two. In both spectra $\sigma_a(\omega)$ and $\sigma_c(\omega)$, we observe one high-energy excitation between 4.2 and 4.8 eV in all compounds (see Fig. 5.11). The fact that we see this excitation in both directions at similar energy suggests the identification with a one-center exciton. This is supported by the similar findings in the 1 D and 2 D structures as summarized in chapter two. Next, we focus on the much discussed energy range of the lowest interband excitations between 1.5 to 3.5 eV. As our summary of experimental and theoretical results in chapter two shows, there is no consensus if the lowest excitation is a one-center or a two-center excitation or if it is a $p-d$ or $d-d$ transition. In the cluster model of Moskvin et al. the lowest-lying

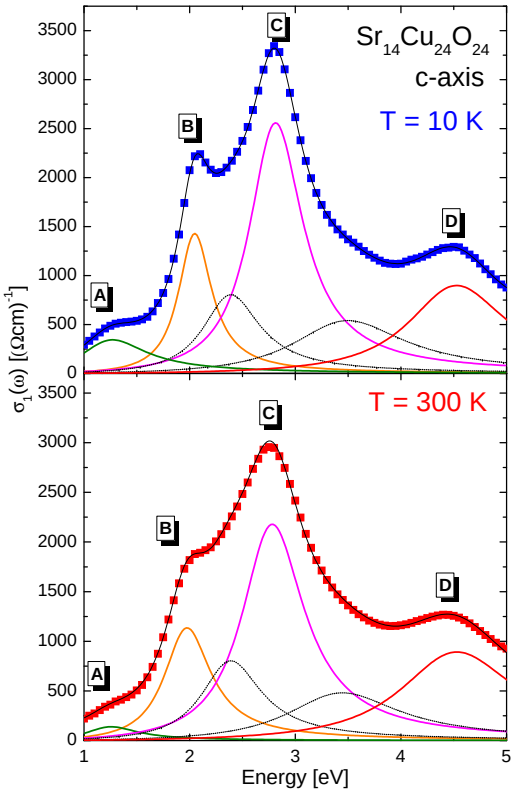

Figure 5.14: Optical conductivity spectra $\sigma(\omega)$ parallel to c of SCO at T = 10 K and T = 300 K with a Lorentz-oscillator model fitted to the spectrum. Six Lorentz oscillators perfectly describe the spectrum. However parameter correlation is strong.

excitation is assigned to a one-center $p-d$ excitation $b_{1g} \rightarrow e_u(\pi)$. Moskvin *et al.* calculated the OCE energy for 1D and 2D systems and find them between 2.0 - 2.2 eV with only a small spectral weight. In our data, peak **B** in $\sigma_c(\omega)$ (see Fig. 5.13 and table 5.1) could be a candidate for this excitation. However, for a one-center excitation there should be no difference between chains, ladders or crystallographic directions. Therefore, it should be visible in the spectrum of $\sigma_a(\omega)$ as well. However, we do not observe a pronounced peak at 2.0 eV in $\sigma_a(\omega)$ but only a broad absorption peak around 2.4 eV (see Fig. 5.9). In addition to that, we do not observe an absorption feature around 2.0 eV for polarization perpendicular to the chains in the 1D zigzag chain $SrCuO_2$ (investigated in chapter 6). This leads us to the statement that peak **B** cannot be assigned to a one-center excitation. The $d-d$ transition is also ruled out because of the strong intensity of our peaks[2].

[2] A $d-d$ excitation is optically forbidden but could be observed with small intensity however, due to symmetry breaking.

	LCO	SCO (x = 0)	SCCO (x = 5)	SCCO (x = 8)
	0.2 holes per f.u.	6 holes	6 holes	6 holes
***a* axis**				
ω_{01} [eV]	2.52	2.43	2.43	2.46
ω_{02} [eV]	3.81	3.61	3.78	4.01
ω_{03} [eV]	-	4.50	4.67	4.84
***c* axis**				
ω_0**A** [eV]	-	1.26	1.24	-
ω_0**B** [eV]	2.08	2.08	2.14	2.22
ω_0**C** [eV]	2.67	2.79	2.79	2.89
ω_0**D** [eV]	4.19	4.50	4.50	4.54

Table 5.1: Peak positions of the major absorption features in σ_a and σ_c for four different compounds at T=10 K.

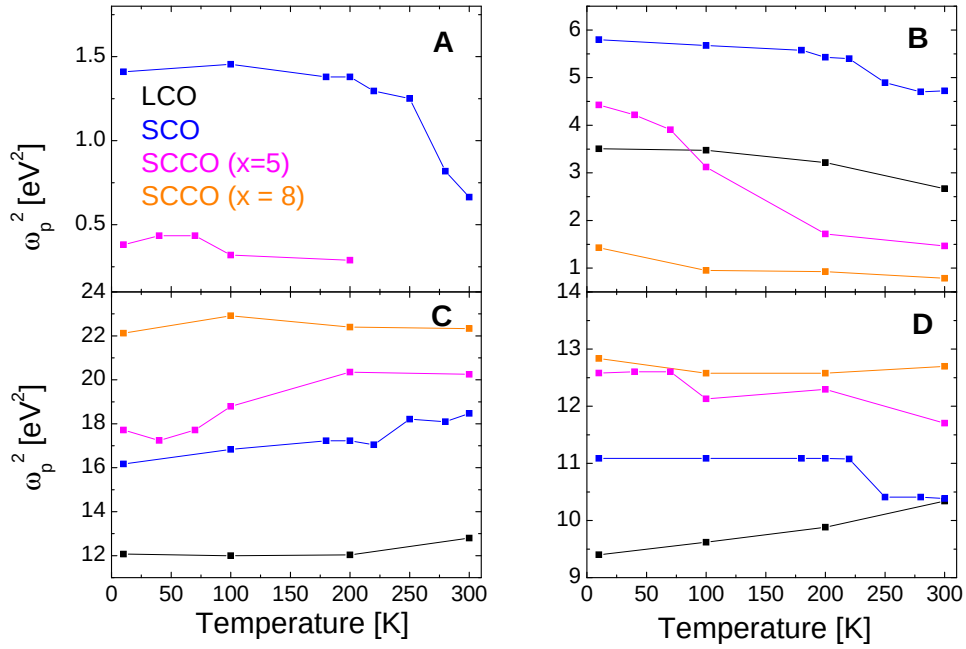

Figure 5.15: Fit parameter ω_p^2 (measure of the spectral weight) from Lorentz-model for peaks A, B, C, and D in LCO and SCCO (x = 0, 5, and 8) as a function of temperature.

Another candidate for the lowest interband excitation is the two-center exciton $b_{1g} \rightarrow b_{1g}$ or ZN exciton. As shown in chapter two, this exciton was reported to lie between 1.7 to 2.5 eV. For this excitation, charge-carrier hopping is crucial.

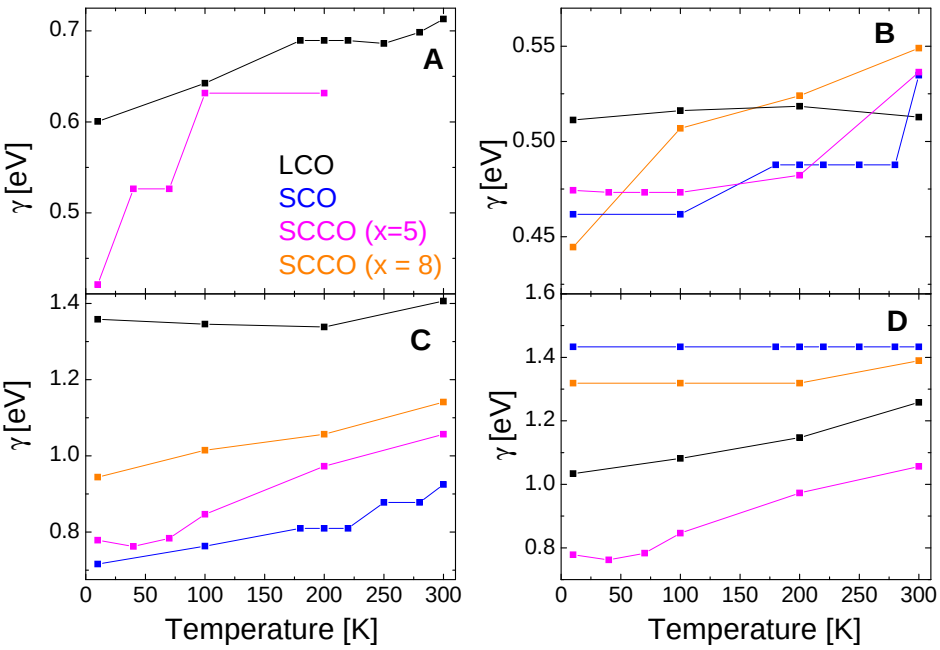

Figure 5.16: Fit parameter γ (measures the peak broadening) from Lorentz-model for peaks A, B, C, and D in LCO and SCCO (x = 0, 5, and 8) as a function of temperature.

Therefore, it is not expected for the (edge-sharing) chains in our compounds (due to suppressed charge-carrier hopping in edge-sharing chains) but for the corner-sharing legs of the ladders in $\sigma_c(\omega)$ and the corner-sharing rungs in $\sigma_a(\omega)$. Looking at our spectra, we identify the above mentioned broad peak at 2.4 eV in $\sigma_a(\omega)$ and a double peak structure in $\sigma_c(\omega)$ between 2.0 and 2.9 eV (**B** and **C**). Is it possible that these peaks all belong to the same excitation? As we found out, the development of spectral weight with temperature and Ca substitution supports this idea. The spectral-weight redistribution with temperature and Ca content is most striking in the double-peak structure (**BC**) of $\sigma_c(\omega)$ in the hole-doped compounds. We know that the hole-doped compounds show a metallic behavior with rising Ca content (also observed in DC resistivity of SCCO, see Fig. 5.3) and with rising temperature along the chain direction. This growing metallicity can also be observed in the far-infrared optical conductivity of SCCO (see Fig. 5.22) where a Drude contribution from free charge carriers grows in one compound with rising temperature (see x = 0 in Fig. 5.30) and with rising Ca content (x = 0 to x = 8). This effect is more pronounced in c than along a. Interestingly, the spectral-weight shift within the *interband* excitation spectrum in $\sigma_c(\omega)$ is related to the change in metallic behavior. How can this be understood in an excitonic picture? The ZN exciton consists of a bound state of a doubly occupied site and

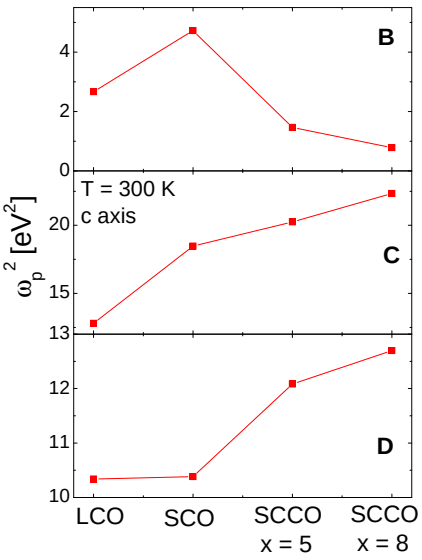

Figure 5.17: Comparison of oscillator strength ω_p^2 for peaks A, B, C, and D in all compounds for T = 300 K and T = 10 K.

a Zhang-Rice singlet state as depicted in Fig. 2.12 of chapter two. It extends over two sites and is bound by Coulomb attraction. A rising metallic behavior could lead to a screening of the Coulomb attraction. This effect should be mirrored by a loss in spectral weight of this particular excitation. As a matter of fact, this is exactly what we observe for excitation **B** (most prominent for SCO). Where does the spectral weight go? The answer is given by the following analysis of the Drude-Lorentz fit parameters. As we will see, the spectral weight is transferred to higher energy, namely to peak **C**. The effect is the same for rising temperature in one compound (see SCO in Fig. 5.10) as well as rising Ca substitution (x = 0 to x = 8). This temperature dependence of the fit parameters of **B** and **C** will be discussed in more detail further below and an interpretation of the double-peak structure is given. Before doing this, we investigate peak **A** below the gap at 1.24 eV, that is only observed in $\sigma_c(\omega)$ of two compounds. We clearly identify it in the hole-doped compounds for x = 0 and for x = 5 at low temperatures. In the spectra of the more metallic sample (x=8), we only find a Drude contribution in this energy range at all temperatures. Excitation **A** shows a strong temperature dependence. It is suppressed with rising temperature and simultaneously a Drude weight comes up. In Fig. 5.15 the results for the fit parameter ω_p^2 are shown as a function of temperature. ω_p^2 is a measure of the spectral weight of the individual oscillators as described above. Peak **A** clearly loses spectral weight with rising temperature and this is most pronounced for x = 0. For x = 5 it could not be observed at T = 300 K. The temperature at which peak **A** is suppressed,

hints to a correlation between the temperature at which the charge ordering in the systems breaks up [111]. Peak **A** could therefore be interpreted in terms of an excitation of pinned charge carriers in the charge-ordered regime. The investigation of the fit parameter ω_p^2 of peak **B** also shows a correlation to the charge-ordering temperatures for x = 0 and x = 5. In SCO, a remarkable decrease sets in above 220 K and in x = 5 the noticeable decrease sets already in above 50 K . In both compounds signatures of charge ordering have been found in the chains with transition temperatures around T=200 K for SCO and 50 K for x = 5 ([111] see introduction to this chapter). This also supports the idea that peak **B** is affected by the growing metallic behavior. In case of excitation **C** an increase in spectral weight is observed at the same time, leading us to the conclusion that the double peak structure **B C** belongs to the ZN excitonic resonance (peak **B**) and the corresponding continuum (peak **C**). In this context it is important to mention that the term "ZN exciton" has been derived from cluster calculations. In these calculations it is not possible to distinguish a truely bound exciton from a resonance within the continuum. In an extended solid, exciton formation will give rise to a double-peak structure, the upper peak representing the continuum, and the lower one the bound state. However, if the attractive interaction is not strong enough to form a truely bound exciton, one expects an excitonic resonance within the continuum plus the original continuum peak at higher energy. In $\sigma_a(\omega)$ we only observe one broad peak around 2.4 eV which we assign to the ZN continuum, too. In Fig. 5.17 the dependence of ω_p^2 as a function of hole doping and Ca content is shown for excitations **B**, **C**, and **D** at T= 300 K. Peak **B** loses weight with Ca content, **C** and **D** gain weight with rising Ca content.

5.3 Kramers-Kronig transformation

In this section, we combine far- and mid-infrared reflectance data from previous Fourier transform spectroscopy measurements [120] with our ellipsometric results of ε_1 and ε_2 in order to evaluate the spectral-weight transfer in the *c*-axis over the complete energy region between 10 meV to 5 eV. The development of spectral weight could give an insight into the complex interplay between low and high-energy excitations and the strong temperature dependence of the optical spectra of the spin ladders. To achieve this, a Kramers-Kronig transformation has to be performed on the reflectance R by extrapolation to $\omega \rightarrow 0$ and to high frequencies as described in chapter 3. We only discuss the *c*-axis because σ_a does not show a strong temperature dependence. We used a Drude-Lorentz model to simultaneously fit FT reflectance data and ellipsometric ε_1 and ε_2. However, it turned out to be difficult to combine these data in the overlap region around 0.75 eV (6050 cm^{-1}) as shown in Fig. 5.18 (upper left panel). The absolute values of R in the mid-infrared region are too low to match the ellipsometric result. We suppose that

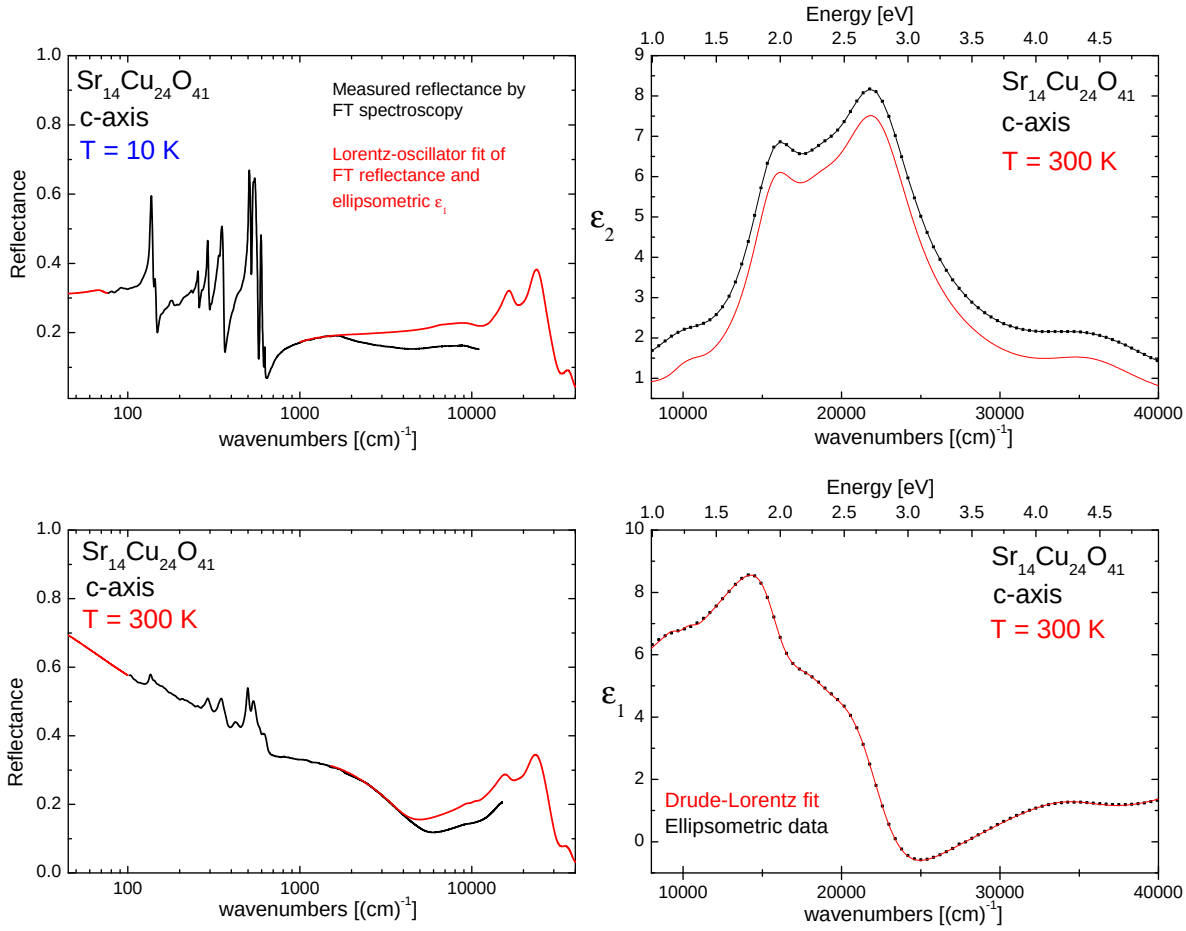

Figure 5.18: Left panels: The black curves represent results of FT reflectance measurements for x = 0 at 10 K (upper panel) and 300 K (lower panel). The red curves represent extrapolations of the reflectance data on the basis of the simultaneous fit of R and ellipsometric ε_1. The right panel shows ellipsometric ε_1(lower panel) and ε_2 (upper panel) with the corresponding fit data (red line). ε_2 was not included into the fit. The fit perfectly describes ε_1. In case of ε_2 the line shape is reproduced by the fit, however the absolute value shows an offset.

this offset has more than one reason. In ellipsometry, we are facing the problem of unknown surface layers that influence the absolute value of ε_2 and in reflectance measurements we are confronted with possible intensity loss due to stray scattering. To illustrate this, we show in Fig. 5.19 different results for the reflectance of $Sr_{14}Cu_{24}O_{41}$, measured at room temperature by three different groups. All data sets have different absolute values. Another reason for this offset could be a different oxygen stoichiometry of the samples. We do, however, not know the exact

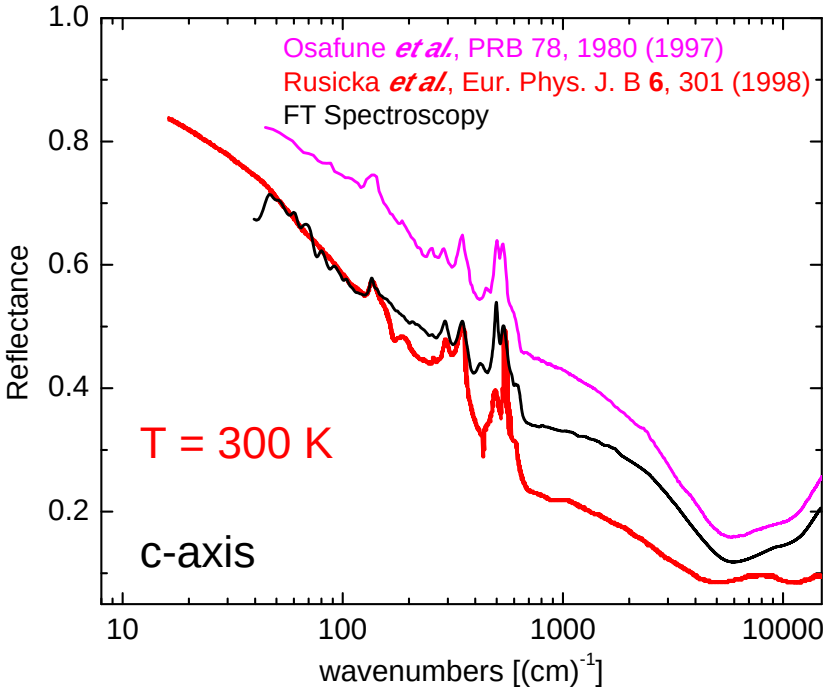

Figure 5.19: Comparison of three different reflectance data sets of the same compound (x = 0) measured at room temperature. The black curve represents our FT data, the red and pink curves represent digitalized data of Rusicka *et al.* [121] and Osafune *et al.* [86], respectively. The origin of these offsets is not clear. A possible explanation could be a variation in oxygen stoichiometry.

answer. It turned out that a very good result for a Kramers-Kronig consistent fit was finally obtained by simultaneously fitting R and ellipsometric ε_1 and in case of x = 0 of transmittance. It delivered a very good description of absolute values and line shapes of R from far to mid-infrared region and of ellipsometric ε_1 as seen in Fig. 5.18. It also provided a very good description of ε_2 concerning line shape, however the absolute value of ε_2 from Kramers-Kronig transformation 0.7 below ε_2 from ellipsometry. This difference on one hand could be a Kramers-Kronig problem due to extrapolation of the data above 5 eV, on the other hand the ellipsometric data may be slightly too high due to e.g. a surface layer. The deviation in ε_2 directly translates into a lower σ_1 from Kramers-Kronig transformation compared to ellipsometry as shown in Fig. 5.20 where we included digitalized σ_1 from Eisaki *et al.* [88] which has an even lower absolute value. The inset in the upper panel of Fig. 5.20 shows optical conductivity data at 10 K that we derived by FT-transmittance and reflectance measurements [35] showing that σ_1 from Kramers-Kronig transformation is close to this result. Since the combination

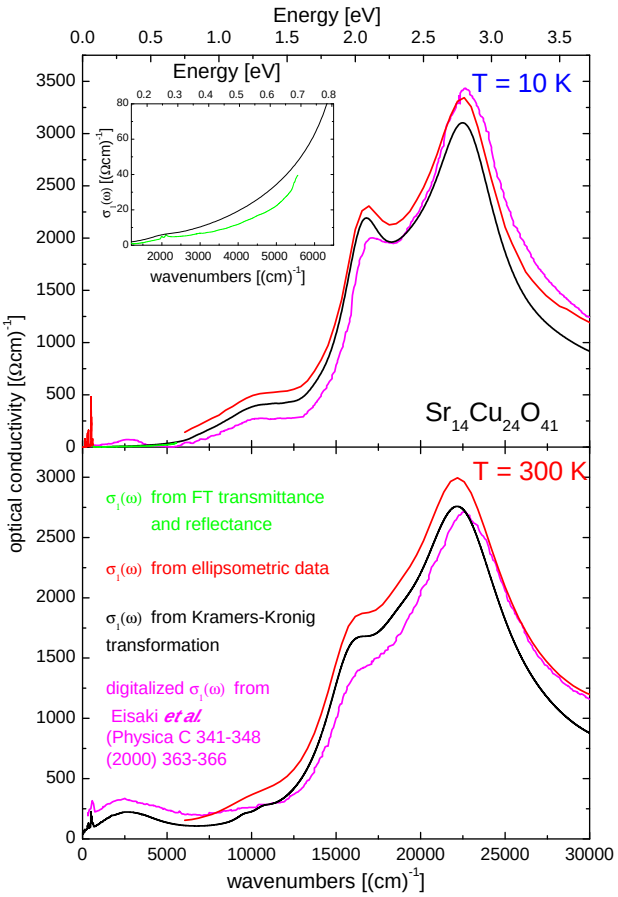

Figure 5.20: Optical conductivity of x = 0 by Kramers-Kronig transformation (black line) at T = 10 K (upper panel) and T = 300 K (lower panel). The red curve represents $\sigma_1(\omega)$ from ellipsometry and the pink line shows digitalized $\sigma_1(\omega)$ of Eisaki *et al.* [88]. At 10 K we used optical conductivity data from transmittance measurements as a reference (green curve, see also inset in the upper panel).

of FT transmittance and reflectance measurements is a very accurate technique, we come to the conclusion that our fitting procedure leads to the best solution for our problem. To reach a consistent description, we used the same fitting routine for all doping levels. Fig. 5.21 shows a combination of the measured reflectance data and the above described fit of R for all measured samples at T = 10 K and T = 300 K. At low temperatures, only x = 0 shows insulating behavior with the phonon spectrum clearly visible in the far-infrared region. The other compounds show already a plasma edge signaling free charge carriers confirming the growing metallic behavior with rising Ca substitution. At room temperature even x = 0

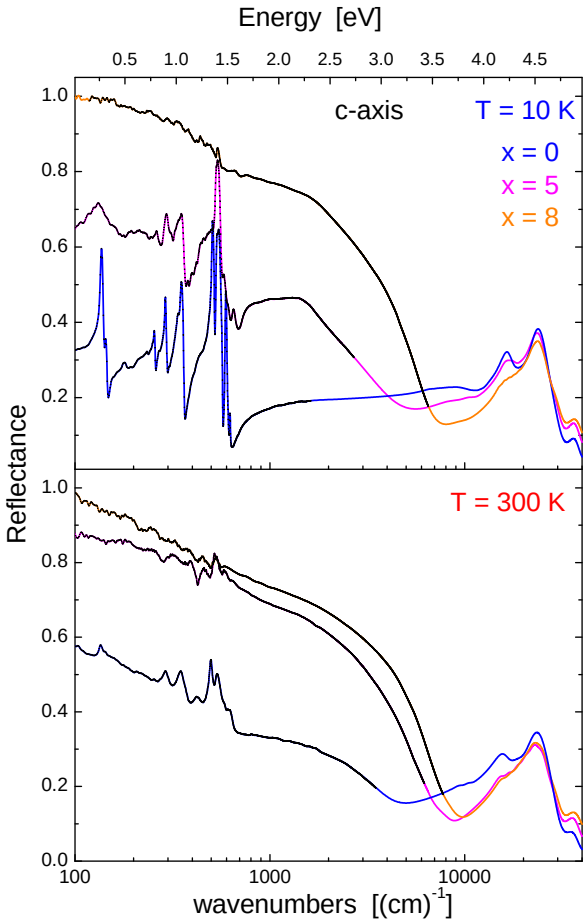

Figure 5.21: Reflectance data for x = 0, 5, and 8 (black lines) and fitted data for x = 0 (blue line), x = 5 (pink line), and x = 8 (orange line) at T = 10 K (upper panel) and T = 300 K (lower panel) as a result of the combined fit of measured reflectance and ellipsometric ε_1 and ε_2. The measured data were extrapolated above 2000 - 5000 cm^{-1} as shown for x = 0 at 300 K in the lower panel.

develops a plasma edge representing metallic behavior although the DC resistivity shows semiconducting behavior. Osafune *et al.* [86] interpreted this by localization of charge carriers at low frequencies ($\omega \rightarrow 0$) and a recovering of metallic behavior at optical frequencies. A shift in plasma edge is observed with growing Ca content. Fig. 5.22 shows the results for $\sigma_1(\omega)$ from Kramers-Kronig transformation for all compositions (left panel). The right panel shows the spectral weight transfer that we find by integrating over $\sigma_1(\omega)$ up to $\hbar\omega = 5\,\text{eV}$ and calculating the effective electron-number per Cu ion $N_{eff}(\omega)$ with equation 5.2. $N_{eff}(\omega)$ is proportional to the number of electrons involved in the optical excitation up to $\hbar\omega$.

Lets start with the discussion of the temperature dependence of $\sigma_1(\omega)$ and x =

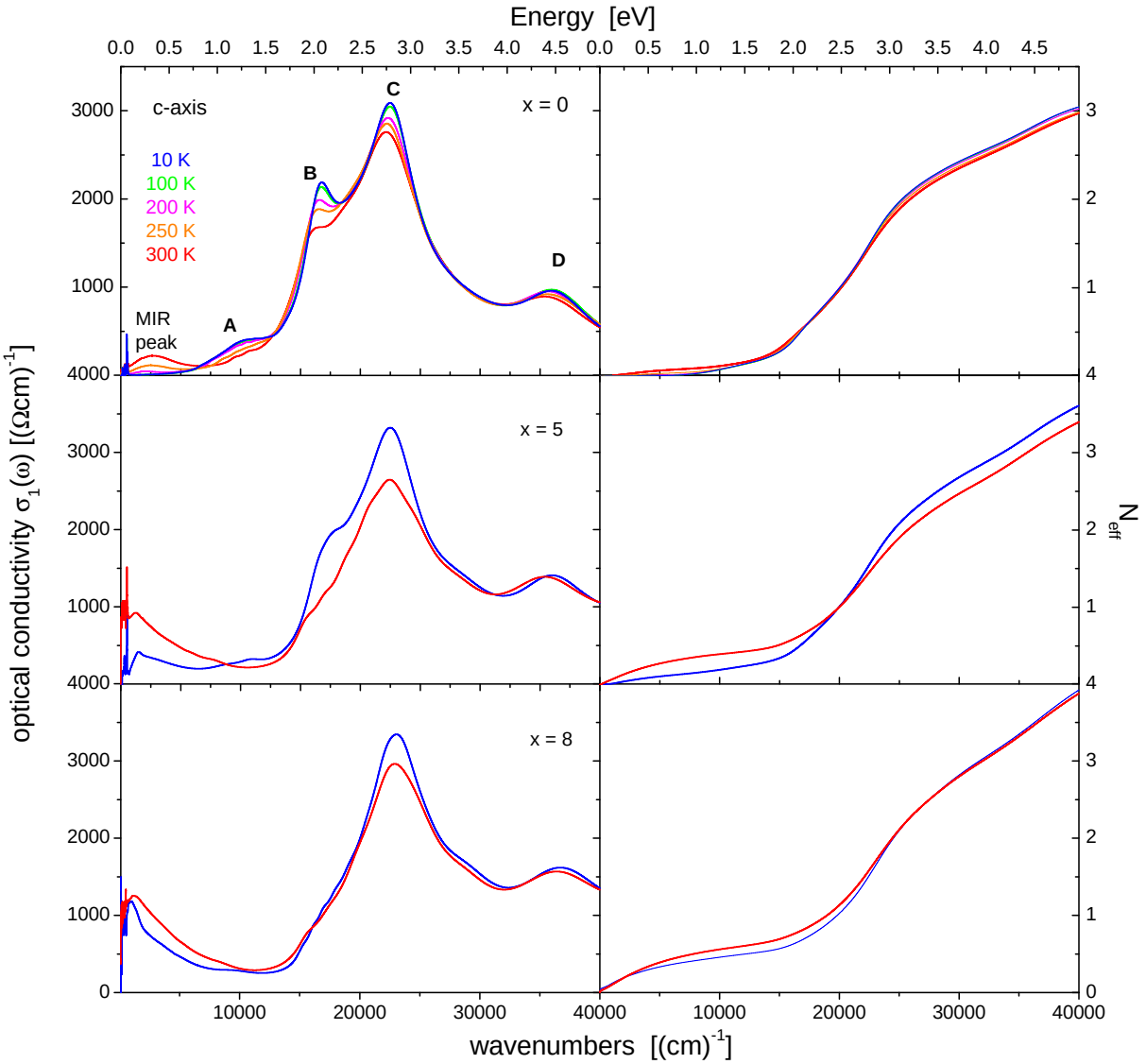

Figure 5.22: Optical conductivity $\sigma_c(\omega)$ from Kramers-Kronig transformation for x = 0, 5, and 8 as a function of temperature up to 5 eV (left panels). The right panels show the effective charge carrier number per Cu ion N_{eff} as a function of energy and temperature.

0 (see left upper panel of Fig. 5.22). In the low-energy region, we observe a broad peak sometimes referred to as the mid-infrared peak around 0.3 eV or 2500 cm^{-1} that is very pronounced at T = 300 K and suppressed at low temperatures. At the same time, an excitation of similar shape centered around 1.2 eV or 10000 cm^{-1}

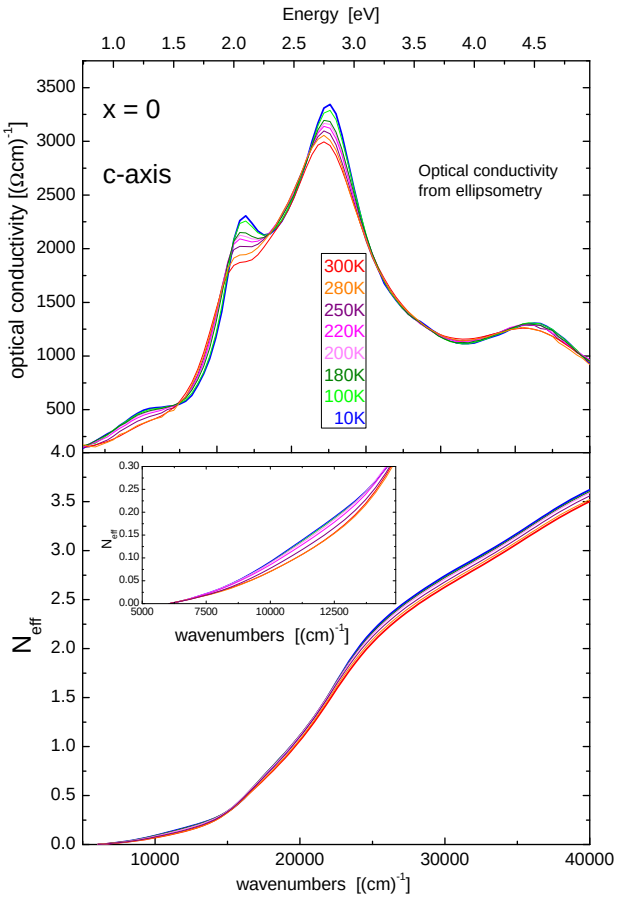

Figure 5.23: Optical conductivity of x = 0 from ellipsometry at different temperatures (upper panel) and N_{eff} (lower panel).

shows the opposite temperature dependence. It grows while the low-energy feature vanishes. This second feature at 1.2 eV corresponds to peak **A** that we have already observed in the ellipsometric spectra. The next higher peaks correspond to peaks **B** and **C** where we found a spectral weight shift from **B** to **C** with rising temperature by a parameter fit to the ellipsometry data. From x = 0 over x = 5 to x = 8 we observe that peak **A** and **B** are suppressed and a Drude weight evolves. The right panels show N_{eff} as a function of energy and temperature for x = 0, 5, and 8. In case of x = 0 we observe a temperature dependence of N_{eff} below 2 eV. Then, between 2.1 eV and 3 eV N_{eff} does not strongly depend on temperature. However, above 3 eV, a temperature dependence is observed again that we do not yet understand. To exclude an error due to the Kramers-Kronig transformation, we show ellipsometric $\sigma_1(\omega)$ for x = 0 with the corresponding spectral weight integral. It shows a similar temperature behavior at high energy.

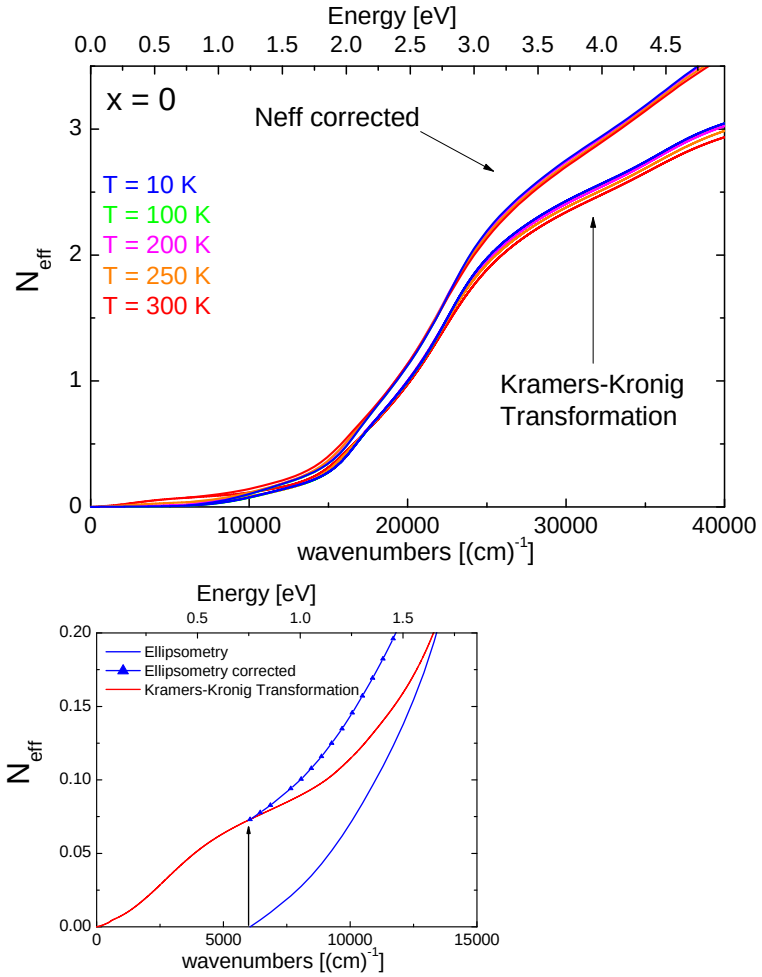

Figure 5.24: Offset correction of ellipsometric N_{eff} for x = 0.

To compare both methods, we have to shift the ellipsometric spectral weight at 0.75 eV by the value acquired below that energy. The result is shown in Fig. 5.24 for x = 0 and in Fig. 5.25 for x = 5 and x = 8. The shifted integrals of ellipsometric N_{eff} lie higher than the Kramers-Kronig result as expected but they show a much smaller temperature dependence at high energy. In principle, one expects that spectral weight is shifted from the CT region to lower frequencies, but not to higher frequencies, i.e. one expects that N_{eff} should be independent of temperature at high frequencies. Above, we have seen that at 10 K the absolute value of ε_2 obtained by Kramers-Kronig transformation is in good agreement with the reliable result obtained by transmission and reflection. In comparison, the ellipsometric data was too high, suggesting a systematic error, e.g., in the analysis of the surface. However, we still expect that accuracy is very high as far as tem-

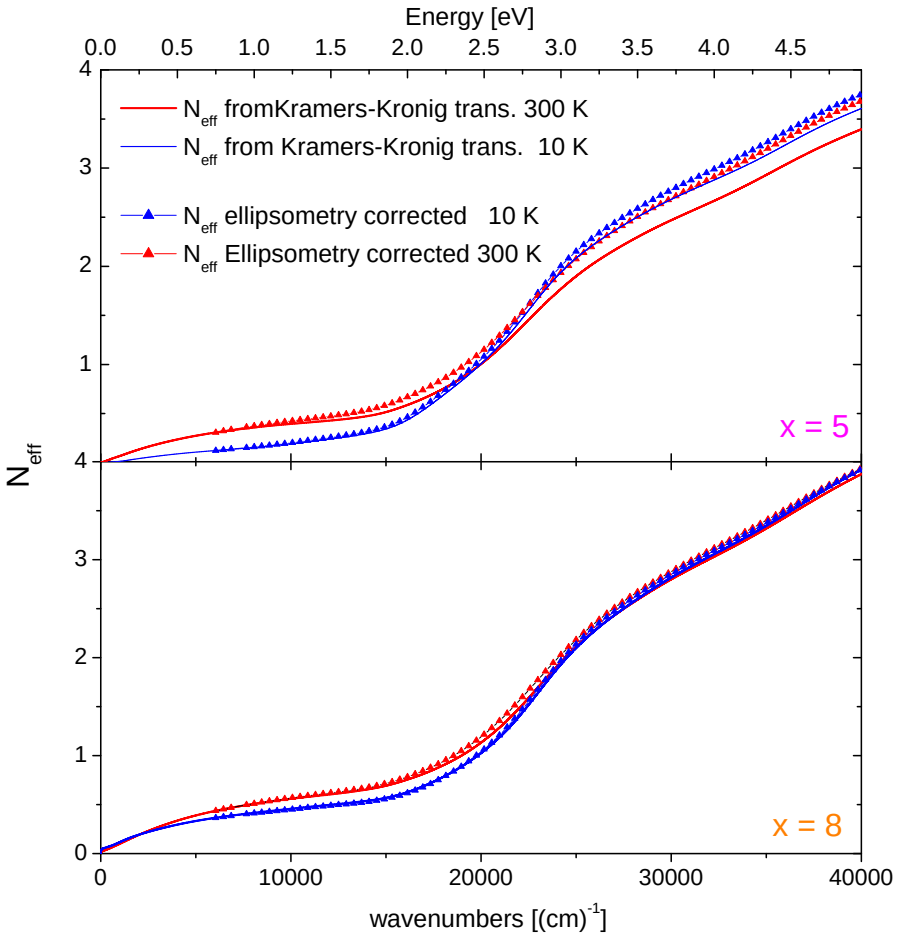

Figure 5.25: Offset correction of N_{eff} for x = 5 and x = 8.

perature is concerned. We thus are convinced that the procedure described above - using N_{eff} from ellipsometry above 0.75 eV and shifting it to the value derived by Kramers-Kronig transformation at 0.75 is the most reliable one. This way we find that N_{eff} is almost independent of temperature above 3 eV not only for x = 0 but also for x = 8 (see Figures 5.24 and 5.25. In the next step we have a closer look at the changes in spectral weight with temperature. Therefore, we have calculated the difference σ_1 (10 K) - σ_1 (T > 10 K) for several temperature intervals up to room temperature. Fig. 5.26 shows the result for x = 0. This comparison nicely shows the change of the excitation spectrum. We see the suppression of peaks **A** and **B** with temperature. From $\Delta\ \sigma$ we calculate $\Delta\ N_{eff}$. Again, we combine the Kramers-Kronig result with ellipsometry by shifting the ellipsometric value by the offset value of the low-energy part. This is shown exemplarily in the upper panel of Fig. 5.27 for x = 0. We see that$\Delta\ N_{eff}$ crosses zero at 2.1 eV in the

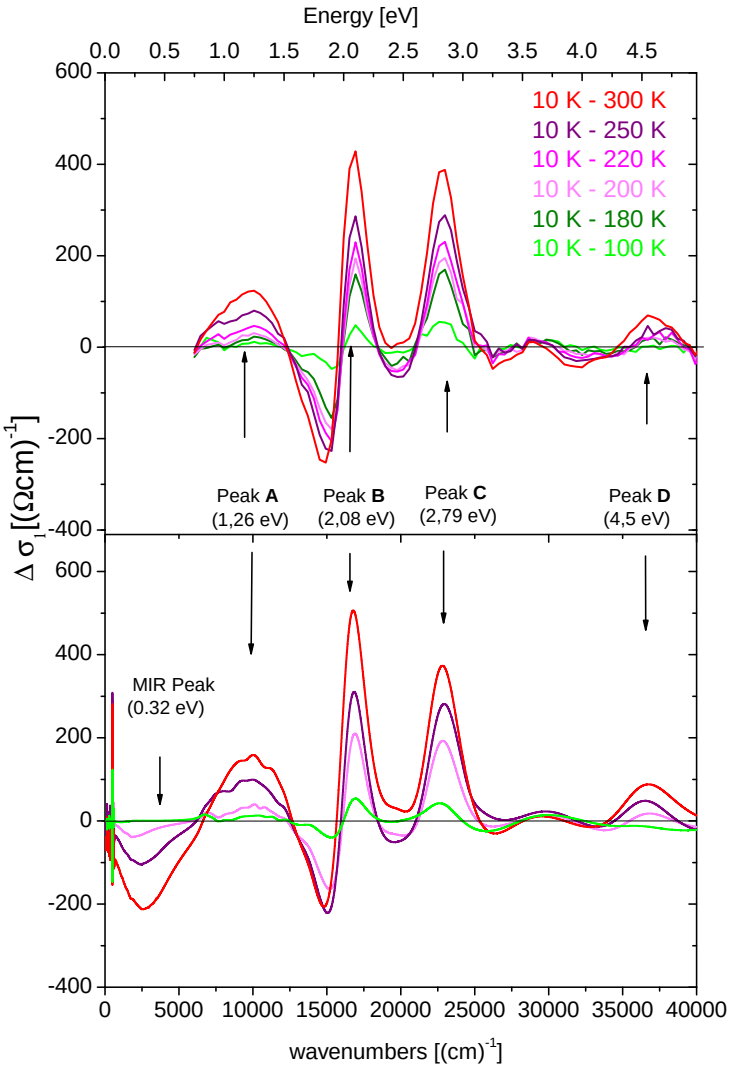

Figure 5.26: Upper panel: Change of optical conductivity from ellipsometry of x = 0 at different temperatures $\Delta\sigma_1$(4 K) - $\Delta\sigma_1$(300 K), $\Delta\sigma_1$(4 K) - $\Delta\sigma_1$(250 K), $\Delta\sigma_1$(4 K) - $\Delta\sigma_1$(200 K), and $\Delta\sigma_1$(4 K) - $\Delta\sigma_1$(100 K). Lower panel: $\Delta\sigma_1$ from Kramers-Kronig transformation.

Kramers-Kronig spectral-weight curve and at 2.7 eV in the shifted ellipsometric result, reflecting the growing low-temperature spectral weight of peak **B**, and N_{eff} stays positive and constant above 3 eV. For x = 0, Δ N_{eff} (10 K - 300 K) at 3 eV is 0.05. This corresponds to a deviation of N_{eff} about 2%. We think that this is roughly the accuracy of our approach, i.e., it is very difficult to say whether this really corresponds to a shift of some spectral weight to higher energies. In any

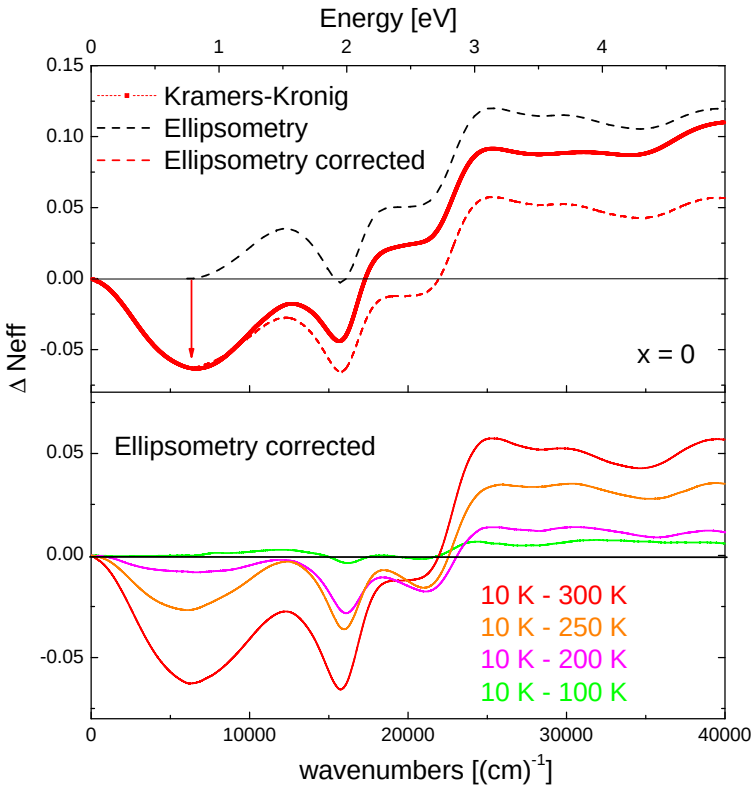

Figure 5.27: Δ N_{eff} (10 K - 300 K) of x = 0 from Kramers-Kronig transformation and N_{eff} from ellipsometry shifted by the low-energy offset (upper panel). The lower panel shows the shifted ellipsometric N_{eff} for x = 0 at different temperatures.

case, the dominant effects of temperature are observed below 3 eV.

This is evident from the plots of σ_1 (4 K) - σ_1(300 K) or from Δ N_{eff} for x = 0, 5, and 8 in Figures 5.28 and 5.29. Finally, we address the dependence of N_{eff} on Ca content x. Fig. 5.30 shows the optical conductivity and N_{eff} for all compositions x at room temperature and at 10 K including the shifted ellipsometric results. If we look at the spectra at 10 K (upper right panel of Fig. 5.30), we see that N_{eff} grows from x = 0 to x = 8 below around 2 eV. Between 2.1 eV and about 3 eV, N_{eff} is not strongly dependent on x. However, above 3 eV, N_{eff} of x = 8 lies above N_{eff} of x = 5 and x = 0 indicating the evolution of a high-energy excitation with higher Ca-content. We again observe that this high-energy deviation of our spectra gets smaller in case of the shifted ellipsometric curves but does not vanish.

In summary, it can be stated that the combination of the two measurement techniques of ellipsometry and FT-spectroscopy provided valuable insight into the temperature dependence of low- and high energy excitations in the optical con-

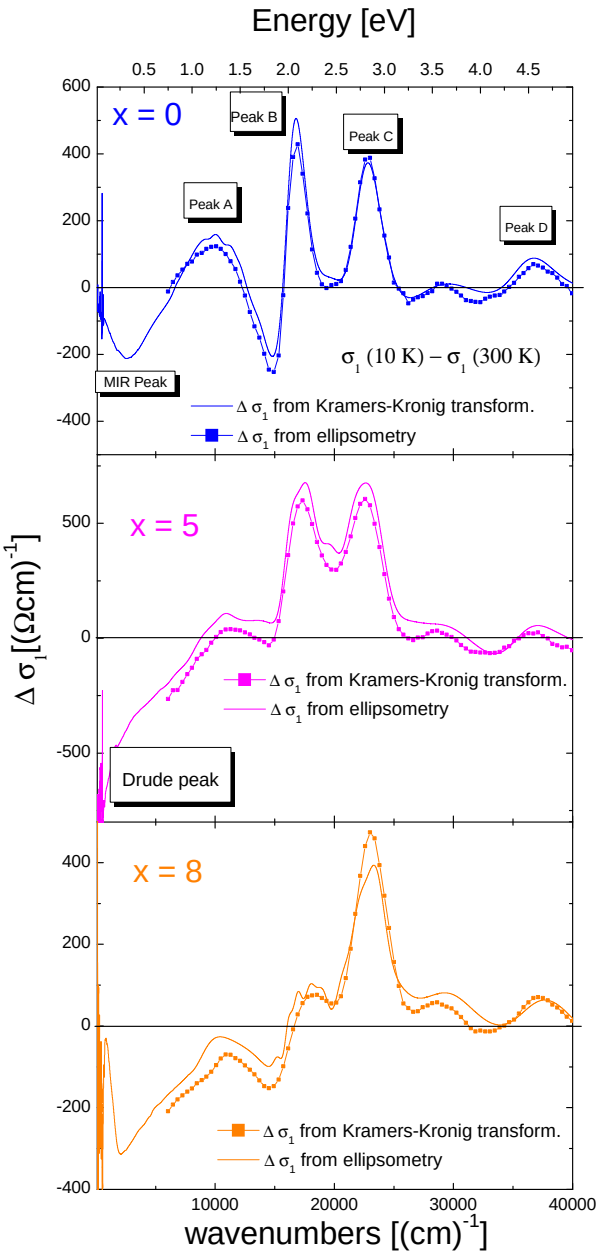

Figure 5.28: Comparison of $\Delta\sigma_1$(4 K) - $\Delta\sigma_1$(300 K) from Kramers-Kronig transformation and ellipsometry for x = 0, 5, and 8.

ductivity of the spin ladders. It shows that a thorough investigation of all effects on the measurement results like sample quality, stoichiometry, surface layers, and systematic effects is important. In spite of the quite difficult task and various

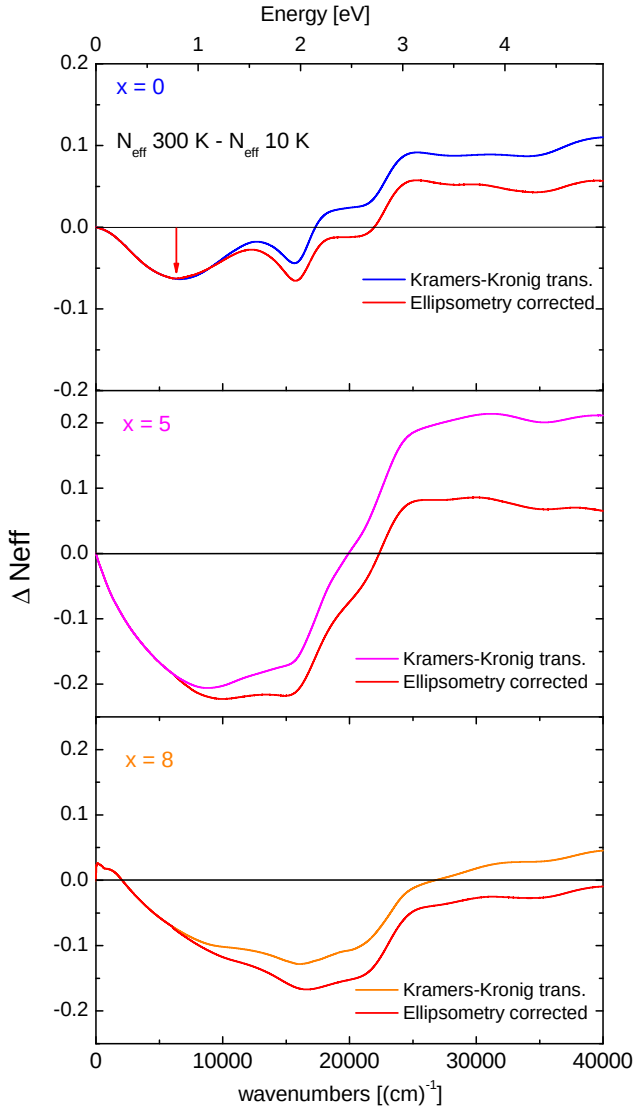

Figure 5.29: Δ N_{eff} (10 K - 300 K) of all compositions including Kramers-Kronig result and shifted Δ N_{eff} from ellipsometry.

problems encountered, we were able to present a systematic overview of optical conductivity data over a broad energy range as a function of temperature and Ca substitution and were able to perform a spectral weight analysis. We found new evidence for the excitonic character of the lowest interband excitation in the spin ladders and a spectral weight transfer from the CT region to low energy with rising temperature. The spectral-weight analysis over the complete energy range by Kramers-Kronig transformation still shows uncertainties making a clear state-

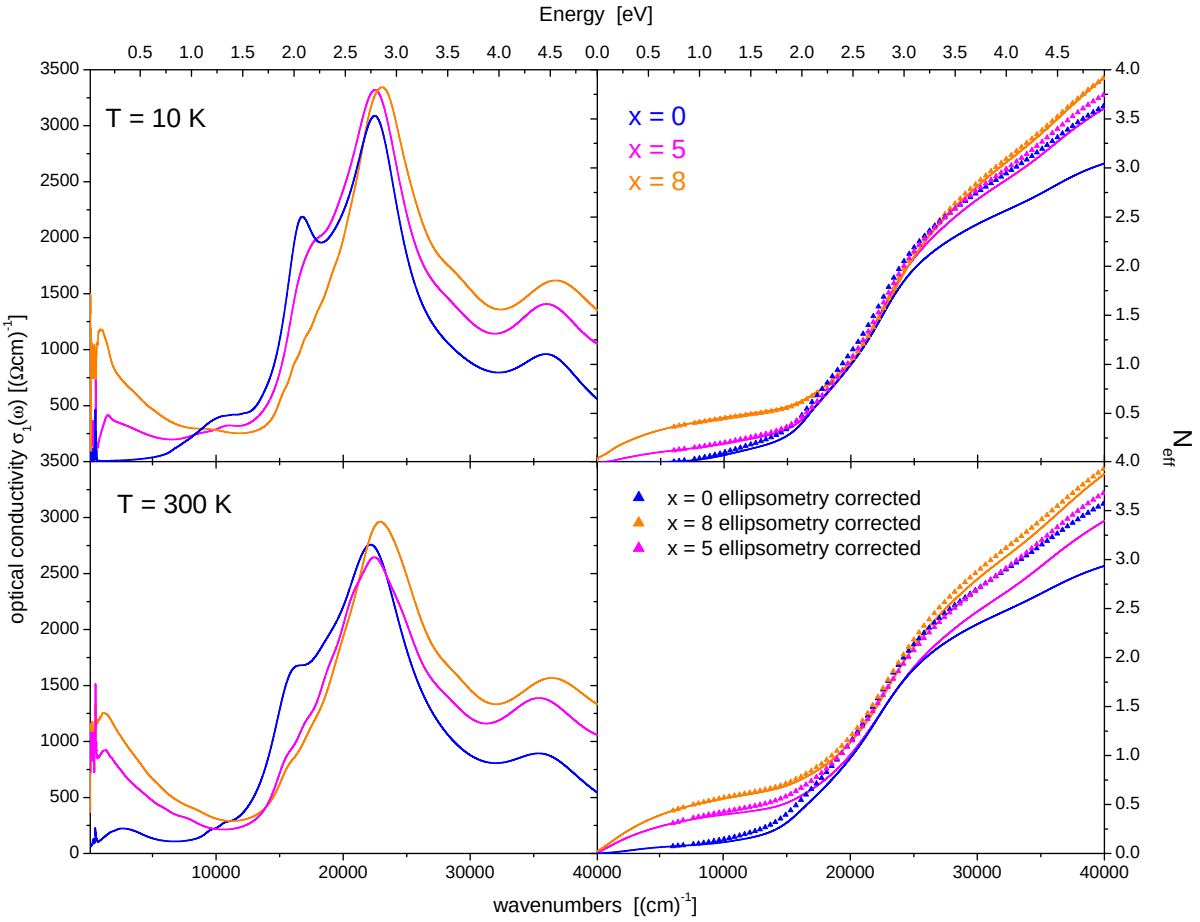

Figure 5.30: Optical conductivity for all doping levels at T = 10 K (upper panel) and T = 300 K and the the spectral weight shift with Ca substitution (right panels). We included N_{eff} from ellipsometry corrected by the low-energy offset.

ment about a possible spectral weight shift to higher energy difficult. This has to be investigated further.

6 Ellipsometry on $SrCuO_2$

6.1 Physics of $SrCuO_2$

Crystal Structure

$SrCuO_2$ is an ideal realization of a 1D $S = 1/2$ Heisenberg chain. It is build up by corner-sharing CuO_4 plaquettes that are connected via the edges to the neighboring squares, forming zigzag chains along the c direction as depicted in Fig. 6.1. It has an orthorhombic unit cell with $Cmcm$ or D_{2h}^{17} space group. The lattice constants are $a = 3.577$, $b = 16.335$, and $c = 3.914$

Electronic Structure

The electronic structure of $SrCuO_2$ was first investigated by Popovic *et al.* using several optical techniques as ellipsometry, (unpolarized) reflectance measurements, polarized optical absorption, and photoreflectance [122]. The experimental results were combined with a tight-binding calculation resulting in an energy gap of 1.42 eV along the chains (c direction) and 1.77 eV perpendicular to the chains (a direction) at room temperature. Furthermore Popovic *et al.* state that the system, in

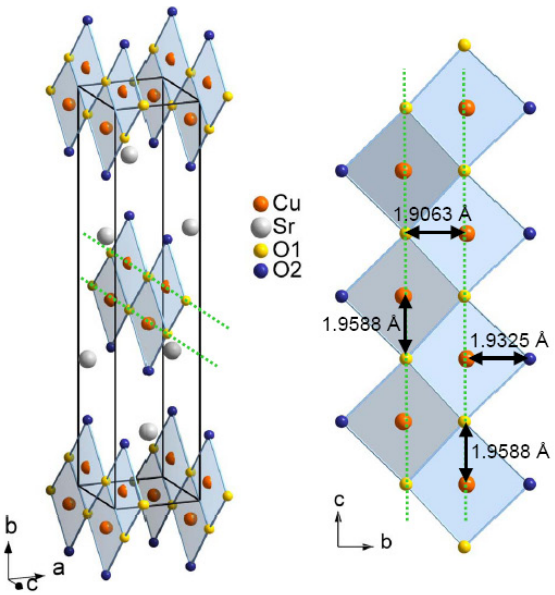

Figure 6.1:
Crystal structure of $SrCuO_2$.

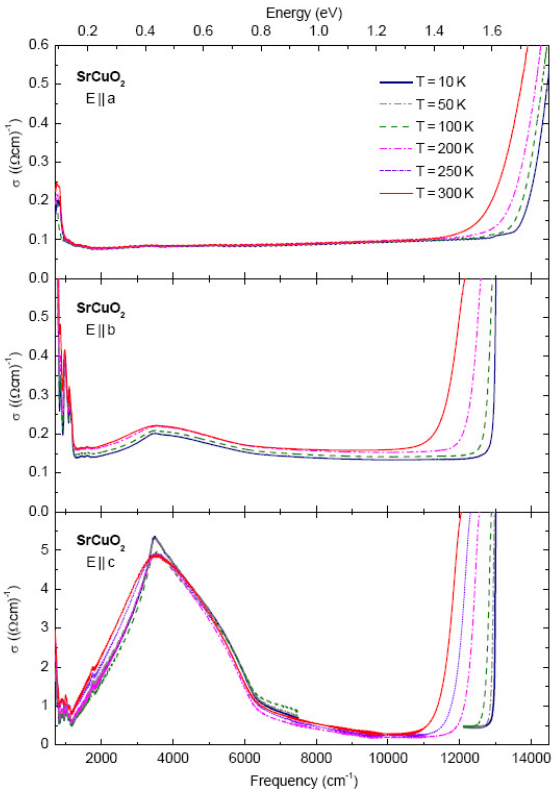

Figure 6.2:
Temperature dependence of the real part of the optical conductivity $\sigma(\omega)$ calculated from reflectance and transmittance data [123] in our group.

contrast to the 2D cuprates, is no charge-transfer insulator but a Mott-Hubbard insulator. This would imply that the lowest lying excitations are of Cu-Cu-type. In [87] the gaps are assigned to indirect ($E||c$) and direct ($E||a$) correlation-gap transitions. The authors claim that this scenario is supported by absorption measurements [122] that do not show a temperature dependence of the gap for $E||c$. Such a variation of the gap with temperature would be typical of a charge transfer-insulator due to changing Cu-O distance. The absorption spectra along the a axis however, show a temperature dependence and there it is assumed that the Cu-O hybridization cannot be neglected. Comparing our results with those of Popovic *et al.*, we conclude that the crystallographic axes were mixed up in their investigation, as will be shown in the following.

In our group, optical transmittance and reflectance measurements were carried out on $SrCuO_2$ as a function of temperature [123]. The optical conductivity $\sigma(\omega)$ was calculated directly from $R(\omega)$ and $T(\omega)$ as described in chapter 3.

Figure 6.2 shows the spectra along all three crystallographic directions. The values of the gap along a and c at room temperature, $\Delta^a_{opt} = 1.72\,\text{eV}$ and $\Delta^c_{opt} = 1.46\,\text{eV}$ were determined by the onset of electronic transitions in the transmittance spectra. Moreover, a distinct temperature dependence is observed along all three crystallographic directions as shown in Fig.6.2 [123].

Holon-antiholon continuum in the 1D corner-sharing chain $SrCuO_2$

In the corner-sharing chain compound $SrCuO_2$, spin-charge separation has been reported [21, 22] by ARPES. In ARPES, a hole is created by removing an electron completely. The created hole then decays into a spinon and a holon resulting in two distinct peaks in ARPES spectra. Those results have been confirmed by inelastic neutron scattering [124] and RIXS [125]. In optical spectroscopy and EELS, charge is conserved since one removes one electron from one site and puts it on another. This creates a hole and a doubly occupied site. In terms of spin-charge separation, the hole decays into a holon (e^+) and a spinon whereas the doubly occupied site decays into an antiholon (e^-) and a spinon. Recently, the energy and momentum dependence of the low-energy charge excitations in $SrCuO_2$ were investigated in a combined study of optical spectroscopy, RIXS and DDMRG calculations by Kim *et al.* [23] (see Fig. 6.3). In contrast to previous theoretical investigations [126]

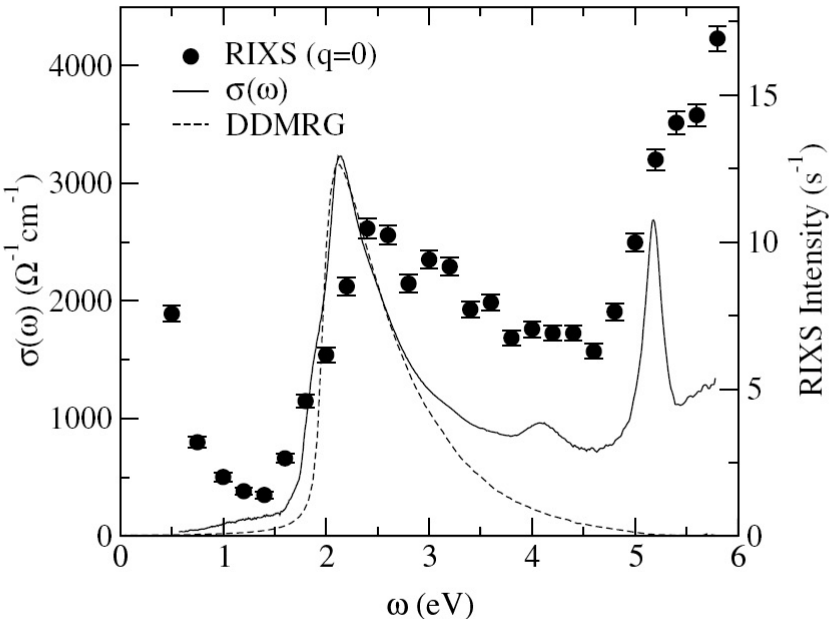

Figure 6.3: Optical conductivity data of $SrCuO_2$ by Kim *et al.* [23] together with DDMRG results and RIXS data.

where an exciton was proposed at the zone boundary, no exciton formation is reported by Kim *et al.*[23] anywhere in the Brillouin zone. As to Kim *et al.*, the excitation spectrum consists of a holon-antiholon continuum with a pronounced resonance closely above the gap. [23], see Fig. 6.3 Kim *et al.* [23] used a DDMRG approach on the basis of the one-band half-filled 1D extended Hubbard model

with nearest-neighbor repulsion V.[1] Optical conductivity data of $SrCuO_2$ along the c direction (derived from reflectance and Kramers-Kronig transformation) were used to fix the parameters of the model. They found $t = 0.435$, $V/t = 1.3$, and $U/t = 7.8$. The calculated optical conductivity is in good accordance with the measured data for the low-energy excitation with onset around 1.7 eV as seen in Fig.6.3. The model of Kim *et al.* supplies a value of $J = 0.24$ that is compared with the value from neutron scattering [124] of $J = 0.226$ eV. A very similar value of $J = 0.227$ eV has also been found by optical spectroscopy in our group [123].

6.1.1 Experimental Details

Single crystals of $SrCuO_2$ were grown by P. Ribeiro, C. Hess, and B. Büchner[2][127] using the traveling-solvent floating zone method. The crystal quality was checked by x-ray diffraction and polarization microscopy. Before measurement, the crystals were oriented with the Laue-method and then cleaved for ellipsometry. This was done to avoid polishing since the family of $Sr_{1-x}Ca_xCuO_2$ strongly reacts with water and acetone. Although a technique of anhydrous lapping and polishing was developed in our group [123], the problem could not be solved to full satisfaction. Since ellipsometry is a very surface sensitive technique and since the samples easily cleave along (010), we avoided polishing altogether.

Pseudo-Dielectric Function

The pseudo-dielectric function was calculated from ellipsometric Ψ and Δ values. When comparing real and imaginary part of our pseudo-dielectric function along a and c with those of Popovic *et al.* [122], it turns out that the assignment of the optical spectra in [122] is different. Our results show basically the same behavior, however, you must exchange a with c. This is corroborated by x-ray absorption measurements [128] which states that holes mainly reside in planar Cu $d_{x^2-z^2}$ orbitals. This favors hopping in the (bc)-plane and not along a-direction. Therefore, one expects a larger gap in a direction than in c direction.

6.2 Optical Conductiviy of $SrCuO_2$

We calculated the optical conductivity from the dielectric function of a biaxial model fit where we assumed a *dummy* layer for the b axis because we could not prepare the bc or ac surface so far. We compare those values with the results

[1] Of course this is a simplified model. To capture the full theory, a multi-band Hubbard model including Cu $3d$ and O $2p$ orbitals is necessary, which is very challenging.

[2] Institute for Solid State Research, IFW Dresden, 01171 Dresden, Germany

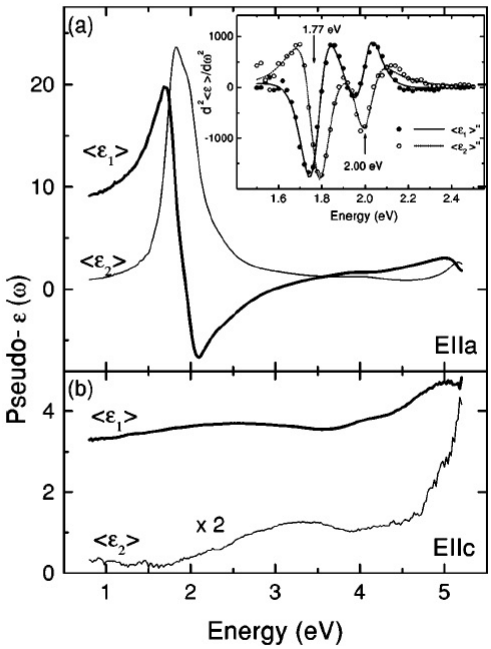

Figure 6.4: Pseudo-dielectric function of $SrCuO_2$ from ellipsometry data of Popovic *et al.* [122].

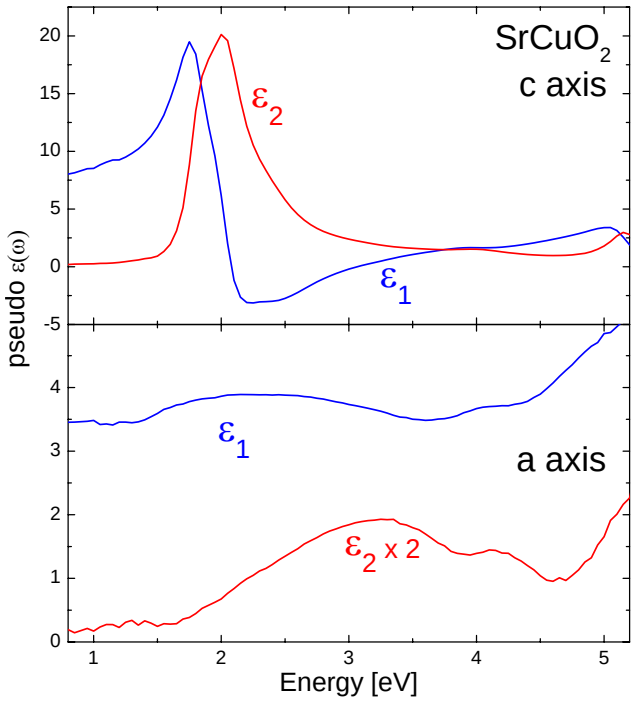

Figure 6.5: Pseudo-dielectric function of $SrCuO_2$ from our ellipsometric data

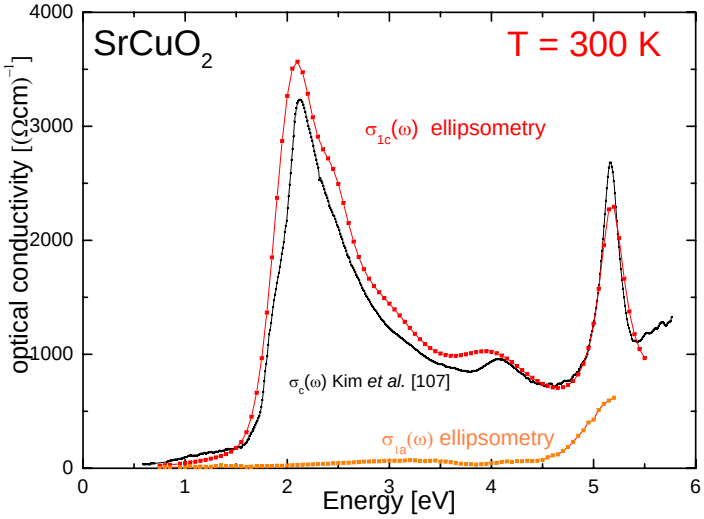

Figure 6.6: Optical conductivity along c and a axes calculated from the dielectric function $\varepsilon_2(\omega)$ from our ellipsometric data. We include the digitalized c axis optical conductivity data of Kim *et al.*.

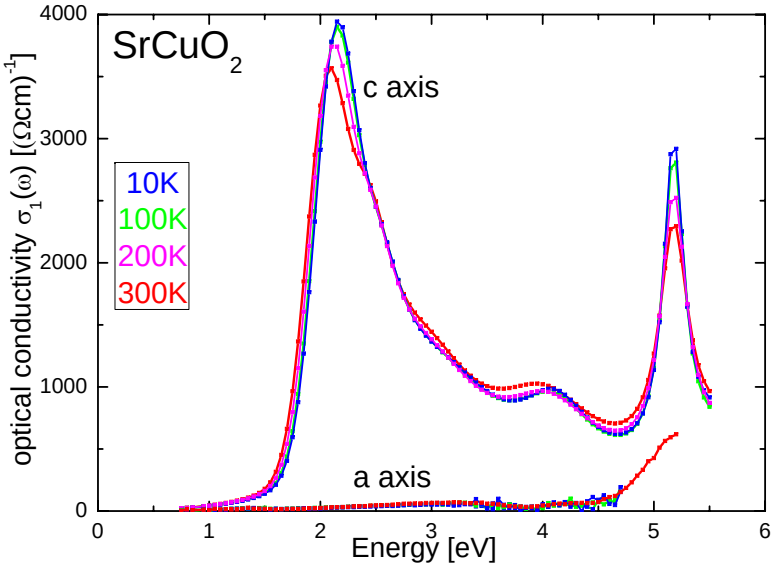

Figure 6.7: Optical conductivity data of SrCuO2 along the c-axis as a function of temperature.

of Kim *et al.*[23] who have measured the reflectance along the c direction and performed a Kramers-Kronig transformation (see Fig. 6.6.

It turns out that our spectrum along c qualitatively and quantitatively matches the one of [23] quite well considering the problem of the missing data for the b axis.

Like in the quasi one-dimensional spin ladder compounds, the optical conductivity $\sigma_c(\omega)$ along the chain direction shows a multipeak structure and a prominent

low energy feature with pronounced temperature dependence. This feature close to the absorption edge at 2.06 eV is identified by Kim *et al.* [23] with a holon-antiholon excitonic resonance. The peak frequency ω_0 found by a Drude-Lorentz

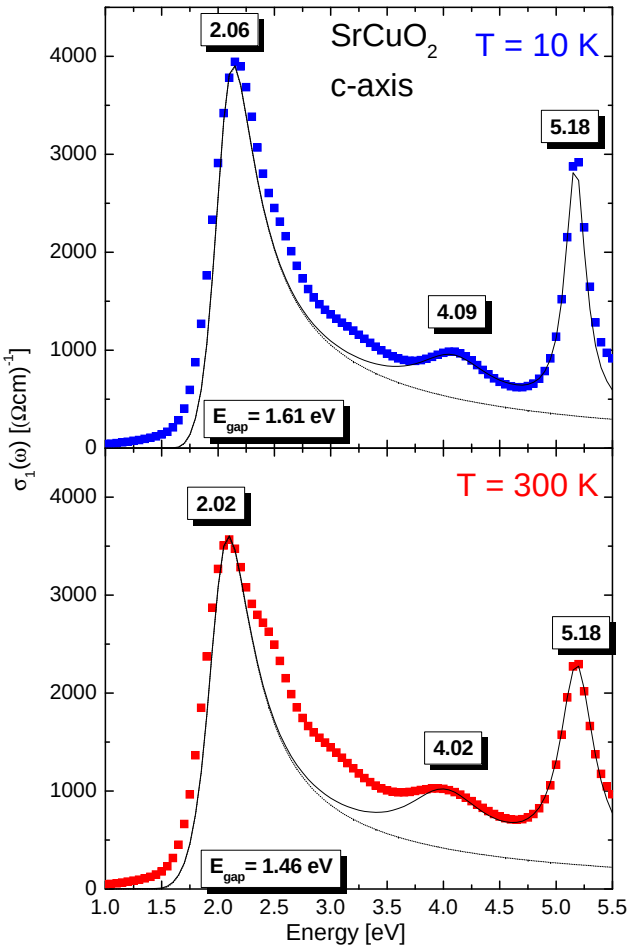

Figure 6.8: Optical conductivity spectra $\sigma(\omega)$ along $c of SrCuO_2$ at T = 5 K and T= 300 K with a minimal Tauc-Lorentz-oscillator fitted to the spectrum.

fit shifts slightly to higher energy by - 40 meV and broadens slightly. As shown in Figure 6.9, the spectral weight is is fully recovered at 2.5 eV. As shown in Fig. 6.8, we used an asymmetric Tauc-Lorentz oscillator to fit the resonance feature to account for the sharp rise of the absorption edge. The values of E_{gap} agree with the results found in FT spectroscopy in our group [123]. In EELS measurements and cluster model predictions of Moskvin *et al.* [60, 78] for the corner-sharing chain Sr_2CuO_3 a peak is found at 2.0 eV for **k** $\parallel$ to the chains which was assigned to a one-center excitation (see table 2.2 in chapter 2). If the excitation belongs to a one-center excitonic resonance or a two-center excitonic resonance is not clear.

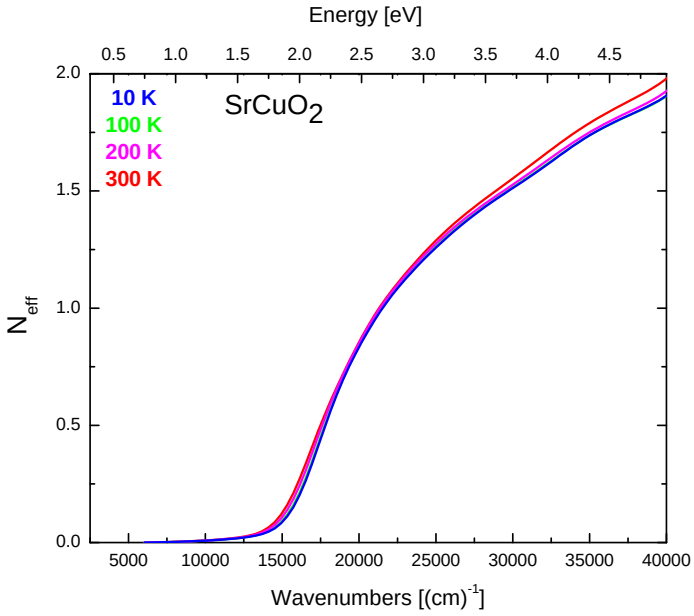

Neff.pdf

Figure 6.9: Effective charge-carrier number per Cu ion N_{eff} of $SrCuO_2$ at T = 10 K and T = 300 K as a function of temperature.

In Fig.6.10 we have plotted together the 10 K data of $\sigma_c(\omega)$ for the undoped spin ladder LCO, the hole-doped spin ladder SCO and $SrCuO_2$ for comparison. In the upper panel we show the measured spectra and in the lower panel we have shifted $\sigma_c(\omega)$ by 0.5 eV to higher energy to compare the peak shape with the one of excitation **C** of the spin ladders that could be identified with a two-center exciton. Regarding the peak energy, the excitonic resonance coincides with the shoulder peak **B**. However, the peak shape is not very similar. The shifted peak however, seems to fit much better to **C**. The only thing which is contradictory here is the comparison with LCO. It is the undoped compound only peak **B** and **D** but not **C** are temperature dependent.

Regarding the peaks at higher energy, we assign the excitation at 4 eV to the high-energy one-center excitation (see table**??**. The very sharp high energy excitation at 5.2 eV is not attributed to a charge-transfer excitation but a transition in Sr because the onset of this excitation is also observed in $\sigma_a(\omega)$ (see Fig. 6.7) which is perpendicular to the Cu-O units and therefore no Cu-O transfer is expected.

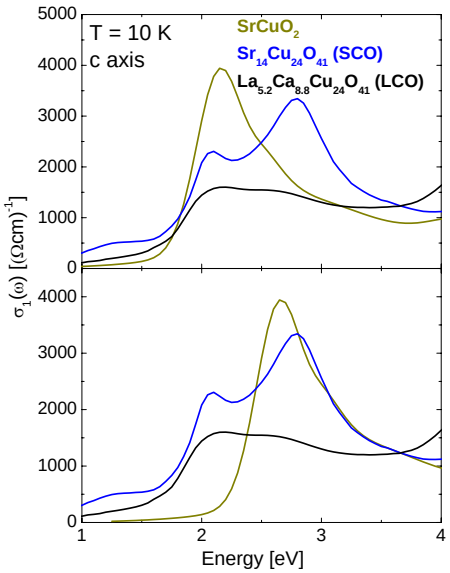

Figure 6.10: σ_c of $SrCuO_2$, $Sr_{14}Cu_{24}O_{41}$, and $La_{5.2}Ca_{8.8}Cu_{24}O_{41}$ at T = 10 K. In the lower panel, the excitonic peak of $SrCuO_2$ was shifted to higher energy by 0.5 eV in order to compare it with the candidate of the ZN exciton in the spin ladders .

7 Conclusions

7.1 Ellipsometry setup

Within the scope of this thesis, a spectroscopic ellipsometer has been put into operation equipped with a UHV liquid Helium flow cryostat to enable low temperature optical measurements down to 10 K in the energy range between 0.8 to 5 eV. After successful installation of the ellipsometer, a systematic investigation of the electronic structure of one-dimensional copper-oxide spin ladders and spin chains was carried out. Ellipsometric optical conductivity data of the biaxial copper oxide compounds $La_{5.2}Ca_{8.8}Cu_{24}O_{41}$ (LCO) with 0.2 holes per formula unit and $Sr_{14-x}Ca_xCu_{24}O_{41}$ for x = 0 (SCO) and x = 5, 8 (SCCO), doped with 6 holes per formula unit, were derived in all three crystallographic axes. We are able to determine the full dielectric tensor of an orthorhombic sample by measuring the Mueller matrix for at least three different orientations of the sample. When measuring unknown bulk samples, the determination of surface layers is crucial. The spin-ladder compounds $(La,Ca,Sr)_{14}Cu_{24}O_{41}$ have a complicated layer structure and it turned out that they are extremely sensitive to polishing and preparation. This means, after repolishing the same surface with the same procedure led to different results in ellipsometric data. Especially the *ab* plane was strongly affected by preparation. However, with many repeated measurements and a multi-sample fit we were able to solve the problem and achieved very good results.

7.2 Investigation of electron hole excitations in spin ladders and spin chains

7.2.1 $(La,Ca,Sr)_{14}Cu_{24}O_{41}$

We present the optical conductivity data from ellipsometry and Fourier-transform spectroscopy on the spin-ladder compound $La_{5.2}Ca_{8.8}Cu_{24}O_{41}$ (LCO) with 0.2 holes per formula unit, and the hole-doped compounds $Sr_{14-x}Ca_xCu_{24}O_{41}$ for x = 0 (SCO) and x = 5, and 8 (SCCO) that are intrinsically doped with 6 holes per formula unit. We investigated the dependence of the interband excitations on temperature and Ca-doping, and we find a multipeak structure in the crystallographic directions a and c. A pronounced temperature dependence in the $\sigma_c(\omega)$

is observed. We used a minimal Drude-Lorentz model to fit the data. The dependence of the individual excitations (i.e. peak frequency, ω_0, oscillator strength, ω_p, and broadening, γ) on temperature and Ca content was evaluated in detail. In $\sigma_a(\omega)$ at T = 10 K, we identify two major absorptions at 2.43 eV and 4.50 eV with negligible temperature dependence that we assign to a ZN-exciton (a bound pair of empty site Cu^+ and a Zhang-Rice singlet state on a neighboring site) and a one-center CT excitation respectively. For x = 0 and T = 10 K we identify four peaks in $\sigma_c(\omega)$ (**A** = 1.26 eV, **B** = 2.08 eV, **C** = 2.79 eV, and **D** = 4.50 eV) which show a strong temperature dependence. In $\sigma_c(\omega)$, the highest excitation **D** at 4.50 eV is assigned to a one-center charge-transfer excitation on one CuO_4 plaquette. It is expected in all compounds in chains and ladders and in both crystallographic directions. This is confirmed by our data. We assign excitations **B** (at 2.08 eV) and **C** (at 2.79 eV) in $\sigma_c(\omega)$ with a ZN-excitonic resonance and the corresponding continuum respectively. This new finding is supported by the evaluation of the Drude-Lorentz fit parameter ω_p because the evolution of the oscillator strength ω_p^2 shows a shift of spectral weight from **B** to **C** with rising temperature from T = 10 K to T = 300 K in case of x = 0. We interpret this change with rising temperature or x in terms of a suppression of the excitonic resonance **B** with growing metallic behavior (x = 0 shows a free charge carrier contribution at room temperature) and a corresponding increase of spectral weight of the ZN continuum. In accordance with this interpretation, we observe a suppression of the excitonic resonance **B** and a rise in spectral weight of **C** in the compounds with higher Ca content which are more metallic. Most strongly this is observed in x = 8 where peak **B** is strongly suppressed even at T = 10 K. Another new excitation not discussed so far in the literature, is found in x = 0 and at T = 10 K at 1.26 eV, in $\sigma_c(\omega)$ only. This excitation **A** is strongly suppressed with rising temperature. It shows a correlation to charge-ordering temperatures observed in the system [111]. Peak **A** is most strongly seen in x = 0 at low temperature, much weaker in x = 5 at T = 10 K and not detectable in the rising Drude contribution of x = 8. To investigate the interesting temperature dependence of the optical spectra further down to low energy, we combined our ellipsometric data with results of far and mid-infrared FT transmittance and reflectance data to perform a Kramers-Kronig transformation over the complete energy range from 10 meV up to 3 eV for all compositions x = 0, 5, and 8 (c axis only). The optical conductivity was derived from a combined Drude-Lorentz fit of FT and ellipsometric data. The integral over $\sigma_c(\omega)$ was evaluated and the effective charge-carrier number per Cu ion N_{eff} was calculated. We observe a strong temperature dependence of the low-energy spectra, too and find a broad low-energy excitation around 0.3 eV, most prominent in x = 0 that is strongest at room temperature and has the opposite temperature dependence compared to peak **A**. The investigation of the change of N_{eff} with temperature showed a spectral-weight transfer from the CT region to the low energy region. Moreover, we also observe a spectral weight shift below 2.5 eV as a

function of x. Namely CT spectral weight is shifted to the low energy region from x = 0 to x = 8. In summary, it can be stated that the combination of the two measurement techniques of ellipsometry and FT-spectroscopy provided valuable insight into the temperature dependence of low- and high energy excitations in the optical conductivity of the spin ladders. It shows that a thorough investigation of all effects on the measurement results like sample quality, stoichiometry, surface layers, and systematic effects is important. In spite of the quite difficult task and various problems encountered, we were able to present a systematic overview of optical conductivity data over a broad energy range as a function of temperature and Ca substitution and were able to perform a spectral weight analysis. We found new evidence for the excitonic character of the lowest interband excitation in the spin ladders and a spectral weight transfer from the CT region to low energy with rising temperature. The spectral-weight analysis over the complete energy range by Kramers-Kronig transformation still shows uncertainties making a clear statement about a possible spectral weight shift to higher energy difficult. This has to be investigated further.

7.2.2 $SrCuO_2$

The results of the optical conductivity $\sigma_c(\omega)$ along the zig-zag chains and $\sigma_a(\omega)$ perpendicular to the chains are presented. The spectrum shows a prominent absorption feature at 2 eV that is assigned to a holon-antiholon excitonic resonance in the literature. Another excitation at 4.2 eV is observed that is assigned to one-center charge transfer excitation similar to those observed in basically all low dimensional copper oxides. A sharp absorption at 5.2 eV is identified with interband transitions in Sr ions because of the sharp feature and the simultaneous observation in $\sigma_a(\omega)$ in the stacking where no Cu-O transitions are expected.

The observations in the 1D spin ladders and chains are very similar and on the basis of our observations of doping and temperature dependence, it might be possible to draw a unified picture perhaps with the support of theoretical investigations, especially in the spin ladder compounds. The understanding of the lowest lying charge transfer excitations in the cuprates is very important for the understanding of high-T_C superconductivity and the physical behavior of correlated electron systems in general. Regarding the spin ladder compounds, it would be very interesting to measure the undoped compound $La_6Sr_8Cu_{24}O_{41}$ (without Ca) to clarify the effect of disorder on the intensity of peak **C** in $\sigma_c(\omega)$. In addition, the determination of the optical conductivity of the edge-sharing compound Li_2CuO_2 in all crystallographic directions and at low temperatures would nicely fit into the systematic investigation started here.

8 Appendix

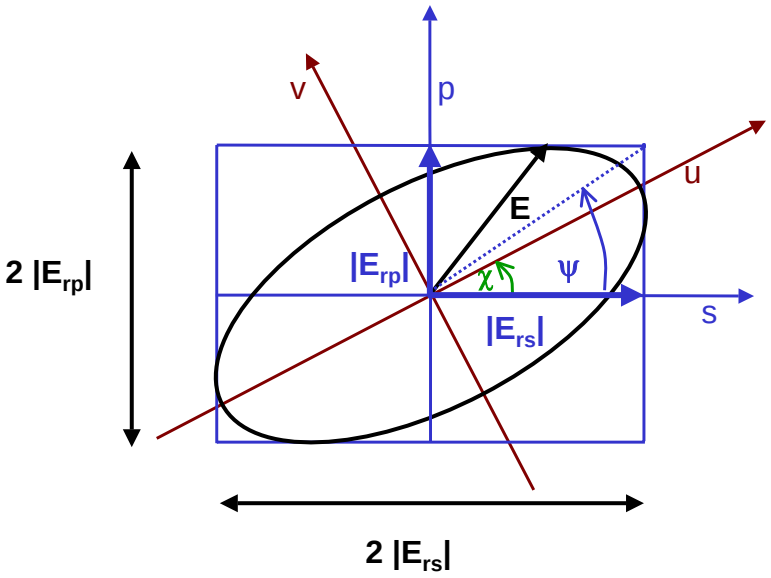

Figure 8.1: Construction of the polarization ellipse with the ellipsometric Parameters.

The polarization ellipse can be constructed from the following relations [96]:

$$\tan 2\chi = \tan 2\Psi \cos\Delta \tag{8.1}$$

$$\sin 2\gamma = \pm \sin 2\Psi \sin\Delta \tag{8.2}$$

$$\tan\Delta = \pm \frac{\tan 2\gamma}{\sin 2\chi} \tag{8.3}$$

8.1 Calibration Procedure

The Fourier-coefficients α and *beta* can be calculated as a function of different polarizer dial settings P, the ellipsometric parameters of the sample Ψ and Δ and three calibration parameters A_S, P_S and η.

$$\alpha = \frac{1}{\eta}\left[\alpha' \cos\left(2A_S\right) - \beta' \sin\left(2A_S\right)\right. \tag{8.4}$$

$$\beta = \frac{1}{\eta}\left[\alpha' \sin\left(2A_S\right) + \beta' \cos\left(2A_S\right)\right. \tag{8.5}$$

$$\alpha' = \frac{\tan^2\Psi - \tan^2\left(P - P_S\right)}{\tan^2\Psi + \tan^2\left(P - P_S\right)} \tag{8.6}$$

and

$$\beta' = \frac{2\tan\Psi\cos\Delta\tan\left(P - P_S\right)}{\tan^2\Psi + \tan^2\left(P - P_S\right)} \tag{8.7}$$

The procedure is as follows: The above mentioned standard sample, in general a Si- wafer with about 250 Å of SiO_2 with known optical constants is mounted and the Fourier coefficients $\alpha_{exp}(P)$ and $\beta_{exp}(P)$ are measured for several polarizer azimuths. From equations **??** $\alpha_{calc}(P, \Psi, \Delta, P_S, A_S, \eta)$ and $\beta_{calc}(P, \Psi, \Delta, P_S, A_S, \eta)$ are fitted to the experimental data minimizing χ^2 [108] with an iterative non-linear regression method, in our case the Levenberg-Marquardt method.

8.2 Measuring a Mueller-Matrix

The Mueller matrix multiplication and corresponding Stokes vectors of incoming and outgoing beam for our setup:

$$\mathbf{S}^D = \left[M_{Analyzer}\, M_{Sample}\, M_{Retarder}\, M_{Polarizer}\right] \mathbf{S}^i \tag{8.8}$$

The multiplication is carried out in several steps to show which elements are accessible. On the right the Stokes vector of the light beam coming from the light source. It is unpolarized. The total intensity is represented by the first component (here normalized to unity). It passes through a polarizer with angle P letting through half the intensity. The resulting Stokes vector of the polarized beam on the left side.

$$\frac{1}{2}\begin{bmatrix} 1 \\ \cos 2P \\ \sin 2P \\ 0 \end{bmatrix} = \frac{1}{2}\begin{bmatrix} 1 & \cos 2P & -\sin P & 0 \\ \cos 2P & \cos^2 2P & \sin 2P\cos 2P & 0 \\ \sin 2P & \sin 2P\cos 2P & \sin^2 2P & 0 \\ 0 & 0 & 0 & 0 \end{bmatrix} \times \begin{bmatrix} 1 \\ 0 \\ 0 \\ 0 \end{bmatrix} \tag{8.9}$$

The next element is a retarder adding a variable phase shift Δ_r to the beam that we later assume here to be zero.

$$\frac{1}{2}\begin{bmatrix} 1 \\ \cos 2P \\ \sin 2P \cos \Delta_r \\ -\sin 2P \sin \Delta_r \end{bmatrix} = \begin{bmatrix} 1 & 0 & 0 & 0 \\ 0 & 1 & 0 & 0 \\ 0 & 0 & \cos \Delta_r & \sin \Delta_r \\ 0 & 0 & -\sin \Delta_r & \cos \Delta_r \end{bmatrix} \times \frac{1}{2}\begin{bmatrix} 1 \\ \cos 2P \\ \sin 2P \\ 0 \end{bmatrix} \tag{8.10}$$

The resulting Stokes vector shows a non-vanishing fourth component representing the tendency for circular polarization. Next the polarized beam is reflected off a sample represented by the Mueller matrix[1]

$$\frac{1}{2}\begin{bmatrix} S_0^R \\ S_1^R \\ S_2^R \\ S_3^R \end{bmatrix} = \begin{bmatrix} m_{11} & m_{12} & m_{13} & m_{14} \\ m_{21} & m_{22} & m_{23} & m_{24} \\ m_{31} & m_{32} & m_{33} & m_{34} \\ m_{41} & m_{42} & m_{43} & m_{44} \end{bmatrix} \times \frac{1}{2}\begin{bmatrix} 1 \\ \cos 2P \\ \sin 2P \cos \Delta_r \\ -\sin 2P \sin \Delta_r \end{bmatrix} \tag{8.12}$$

And finally the beam passes the analyzer with angle A:

$$\frac{1}{2}\begin{bmatrix} 1 & \cos 2A & -\sin 2A & 0 \\ \cos 2A & \cos^2 2A & -\sin 2A \cos 2A & 0 \\ -\sin 2A & \sin 2A \cos 2A & \sin^2 2A & 0 \\ 0 & 0 & 0 & 0 \end{bmatrix} \times \begin{bmatrix} S_0^R \\ S_1^R \\ S_2^R \\ S_3^R \end{bmatrix} \tag{8.13}$$

and reaches the detector where only the fist component, i.e. the full intensity is measured:

$$\frac{1}{2}\begin{bmatrix} S_0^R + \cos 2A\, S_1^R - \sin 2A\, S_2^R \\ \cos 2A\, S_0^R + \cos^2 2A\, S_1^R - \cos 2A \sin 2A S_2^R \\ -\sin 2A\, S_0^R - \cos 2A \sin 2A\, S_1^R + \sin^2 2A\, S_2^R \\ 0 \end{bmatrix} \tag{8.14}$$

In the following we assume that for p polarized light the Polarizer angle is zero and that retarder angle Δ_r to be zero too. With equation 3.74 the ellipsometric parameters follow:

$$\begin{aligned} S_1^D \quad = \tfrac{1}{4}(1 - \cos 2\Psi_{pp} \cos 2P(1 \quad &+ \tfrac{\cos 2P - \cos 2\Psi_{pp}}{1 - \cos 2\Psi_{pp} \cos 2P} \cos 2A(t) \\ &+ \tfrac{\cos \Delta_{pp} \sin 2\Psi_{pp} \sin 2P}{1 - \cos 2\Psi_{pp} \cos 2P} \sin 2A(t) \end{aligned} \tag{8.15}$$

[1]

$$\begin{aligned} S_0^R &= \tfrac{1}{2}\left(m_{11} + m_{12} \cos 2P + (m_{13} \cos\ \Delta_r - m_{14} \sin \Delta_r) \sin 2P\right) \\ S_1^R &= \tfrac{1}{2}\left(m_{21} + m_{22} \cos 2P + (m_{23} \cos\ \Delta_r - m_{24} \sin \Delta_r) \sin 2P\right) \\ S_2^R &= \tfrac{1}{2}\left(m_{31} + m_{32} \cos 2P + (m_{33} \cos\ \Delta_r - m_{34} \sin \Delta_r) \sin 2P\right) \\ S_3^R &= \tfrac{1}{2}\left(m_{41} + m_{42} \cos 2P + (m_{43} \cos\ \Delta_r - m_{44} \sin \Delta_r) \sin 2P\right) \end{aligned} \tag{8.11}$$

In this equation we have already taken into account that the polarizer angle is rotating continuously and therefore $A = A(t)$. As shown in the previous section, we can again identify the Fourier-coefficients of the modulated signal α and β

$$\begin{aligned} \alpha &= \frac{\cos 2P - \cos 2\Psi_{pp}}{1 - \cos 2\Psi_{pp} \cos 2P} \\ \beta &= \frac{\cos \Delta_{pp} \sin 2\Psi_{pp} \sin 2P}{1 - \cos 2\Psi_{pp} \cos 2P} \end{aligned} \tag{8.16}$$

Inversion leads to:

$$\cos 2\Psi_{pp} = \frac{\cos 2P - \alpha}{1 - \alpha \cos 2P} \tag{8.17}$$

and

$$\cos \Delta_{pp} = \frac{\beta}{\sqrt{1 - \alpha^2}} \frac{\sin 2P}{|\sin 2P|} \tag{8.18}$$

To account for all 12 accessible matrix elements of the Mueller matrix, the fourier components of at least 6 different configurations of P and Δ_r have to be measured. With the Woollam VASE RAE, more than 6 configurations are measured and the components are evaluated via regression.

Bibliography

[1] E. Dagotto, Science **309**, 257 (2005). 7

[2] J. Zaanen and O. Gunnarson, Phys. Rev. B **40**, R7391 (1989). 7

[3] J. M. Tranquada, J. D. Sternlieb, J. D. Axe, Y. Nakamura, and S. Uchida, Nature **375**, 561 (1995). 7

[4] U. Löw, V. J. Emery, K. Fabricius, and S. A. Kievelson, Phys. Rev. Lett. **72**, 1918 (1994). 7

[5] E. Dagotto, J. Riera, and D. Scalapino, Phys. Rev. B **45**, 5744 (1992). 7, 12, 13, 14, 79, 80

[6] M. Sigrist, T. M. Rice, and F. C. Zhang, Phys. Rev. B **49**, 12058 (1994). 7

[7] S. R. White and D. J. Scalapino, Phys. Rev. B **65**, 165122 (2002). 7

[8] S. T. Carr and A. M. Tsvelik, Phys. Rev. B **65**, 195121 (2002). 7

[9] M. Kato, K. Shiota, and Y. Koike, Physica C **258**, 284 (1996). 7, 78, 85

[10] S. A. Carter, B. Batlogg, R. J. Cava, J. J. Krajewski, W. F. Peck, Jr., and T. M. Rice, Phys. Rev. Lett. **77**, 1378 (1996). 7, 78, 81, 85

[11] T. Osafune, N. Motoyama, H. Eisaki, S. Uchida, and S. Tajima, Phys. Rev. Lett. **82**, 1313 (1999). 7, 8, 78, 80, 81, 85

[12] M. Uehara, T. Nagata, J. Akimitsu, H. Takahashi, N. Môri, and K. Kinoshita, J. Phys. Soc. Jpn. **65**, 2764 (1996). 7, 14, 79, 81

[13] G. Blumberg, P. Littlewood, A. Gozar, B. S. Dennis, N. Motoyama, H. Eisaki, and S. Uchida, Science **297**, 584 (2002). 7, 81, 82

[14] S. Gorshunov, P. Haas, T. Rõõm, M. Dressel, T. Vuletić, B. Korin-Hamzić, S. Tomić, J. Akimitsu, and T. Nagata, Phys. Rev. B **66**, 060508(R) (2002). 7, 82

[15] T. Vuletić, B. Korin-Hamić, S. Tomić, B. Gorshunov, P. Haas, T. Rõõm, M. Dressel, J. Akimitsu, T. Sasaki, and T. Nagata, Phys. Rev. Lett. **90**, 257002 (2003). 7, 81

[16] H. K. *et al.*, Europhys. Letters **56**, 434 (2001). 7

[17] P. Abbamonte, G. Blumberg, A. Rusydi, A. Gozar, P. G. Evans, T. Siegrist, L. Venema, h Eisaki, E. D. Isaacs, and G. A. Sawatzky, Nature **431**, 1078 (2004). 7, 81, 82

[18] A. Rusydi, P. Abbamonte, H. Eisaki, Y. Fujimaki, G. Blumberg, and S. U. G. A. Sawatzky, PRL **97**, 016403 (2006). 7, 81, 82, 83

[19] R. E. Peierls, *Quantum Theory of Solids*, Oxford University, New York/London, 1955. 7, 80

[20] B. Ruzicka, L. Degiorgi, U. Ammerahl, G. Dhalenne, and A. Revcolevschi, Physica B **259-261**, 1036 (1999). 8, 81

[21] C. Kim, A. Y. Matsura, Z. X. S. an N Motoyama, H. Eisaki, S. Uchida, T. Tohoyma, and S. Maekawa, Phys. Rev. Lett. **77**, 4054 (1996). 8, 113

[22] C. Kim, Z. X. S. an N Motoyama, H. Eisaki, S. Uchida, T. Tohoyma, and S. Maekawa, Phys. Rev. B **56**, 15589 (1997). 8, 113

[23] Y. J. Kim, J. P. Hill, H. Benthien, F. H. L. Essler, E. Jeckelmann, H. S. Choi, T. W. Noh, N. Motoyama, K. M. Kojima, S. Uchida, D. Casa, and T. Gog, Phys. Rev. Lett. **92**, 137402 (2004). 8, 9, 22, 113, 116, 117

[24] J. Hubbard, Proc. Roy. Soc. (London) A **276**, 238 (1963). 11, 24

[25] H. Bethe, Z. Phys. **71**, 205 (1931). 12, 13

[26] N. D. Mermin and H. Wagner, Phys. Rev. Lett. **17**, 1133 (1966). 12

[27] S. Chakravarty, B. I. Halperin, and D. R. Nelson, Phys. Rev. B **39**, 2344 (1989). 12

[28] L. D. Faddeev and L. A. Takhtajan, Phys. Lett. **85A**, 375 (1981). 13

[29] M. Karbach, G. Müller, A. H. Bougourzi, A. Fledderjohann, and K.-H. Mütter, Phys. Rev. B **55**, 12510 (1997). 13

[30] J. des Cloizeaux and J. J. Pearson, Phys. Rev. **128**, 2131 (1962). 13

[31] E. Dagotto and T. M. Rice, Science **271**, 618 (1996). 13

[32] E. Dagotto and A. Moreo, Phys. Rev. B **38**, 5087 (1988). 13

[33] C. Knetter, K. P. Schmidt, M. Grüninger, and G. S. Uhrig, Phys. Rev. Lett. **87**, 167204 (2001). 14

[34] T. Barnes, E. Dagotto, J. Riera, and E. S. Swanson, Phys. Rev. B **47**, 3196 (1993). 14

[35] M. S. Windt, *Optical Spectroscopy of Spin Ladders*, Doktorarbeit, Universität Köln, 2002. 14, 60, 61, 98

[36] M. Windt, M. Grüninger, T. Nunner, C. Knetter, K. P. Schmidt, G. S. Uhrig, T. Kopp, A. Freimuth, U. Ammerahl, B. Büchner, and A. Revcolevschi, Phys. Rev. Lett. **87**, 127002 (2001). 14

[37] M. Azuma, Z. Hiroi, and M. Takano, Phys. Rev. Lett. **73**, 3463 (1994). 14

[38] E. M. McCarron, M. A. Subramanian, J. C. Calabrese, and R. L. Harlow, Mat. Res. Bull. **23**, 1355 (1988). 14, 77

[39] J. G. Bednorz and K. A. Müller, Z. Phys. B **64**, 189 (1986). 14

[40] J. Zaanen, G. A. Sawatzky, and J. W. Allen, Phys. Rev. Lett. **55**, 418 (1985). 16

[41] V. J. Emery, Phys. Rev. Lett. **58**, 2794 (1987). 16

[42] P. W. Anderson, Phys. Rev. **115**, 2 (1959). 17

[43] F. C. Zhang and T. M. Rice, Phys. Rev. B **37**, 3759 (1988). 17, 83

[44] H. Eskes and G. A. Sawatzky, Phys. Rev. Lett. **61**, 1415 (1988). 17

[45] H. Eskes, L. H. Tjeng, and G. A. Sawatzky, Phys. Rev. B **41**, 288 (1990). 17

[46] P. Horsch, W. H. Stephan, K. v Szczepanski, and W. von der Linden, Physica C **162**, 783 (1989). 17

[47] S. K. Y Tokura and T. Arima, Phys. Rev. B **41**, 11657 (1990). 18, 19

[48] S. Uchida, T. Ido, H. Takagi, T. Arima, Y. Tokura, and S. Tajima, Phys. Rev. B **43**, 7942 (1991). 18, 35

[49] M. D. Sturge, Phys. Rev. **127**, 768 (1962). 20

[50] P. Wrobel and R. Eder, Phys. Rev. B **66**, 035111 (2002). 21, 22

[51] J. E. Hirsch, Phys. Rev. Lett. **59**, 228 (1987). 21

[52] J. E. Hirsch, **295**, 2226 (2002). 21

[53] H. J. A. Molegraaf, C. Presura, D. van der Marel, P. H. Kes, and M. Li, **295**, 2239 (2002). 21

[54] D. G. Clarke, Phys. Rev. B **48**, 7520 (1993). 22

[55] Y. Y. Wang, F. C. Zhang, V. P. Dravid, K. K. Ng, M. V. Klein, S. E. Schnatterly, and L. L. Miller, Phys. Rev. Lett. **77**, 1809 (1996). 22, 25, 26, 27, 28, 38

[56] F. C. Zhang and K. K. Ng, Phys. Rev. B **58**, 13520 (1998). 22, 25, 28, 30, 38

[57] R. O. Kuzian, R. Hayn, and A. F. Barabanov, Phys. Rev. B **68**, 195106 (2003). 22

[58] M. E. Símon, A. A. Aligia, C. D. Batista, E. R. Gagliano, and F. Lema, Phys. Rev. B **54**, R3780 (1996). 22

[59] E. Hanamura, N. T. Dan, and Y. Tanabe, Phys. Rev. B **62**, 7033 (2000). 22

[60] A. S. Moskvin, R. Neudert, M. Knupfer, J. Fink, and R. Hayn, Phys. Rev. B **65**, 180512 (2002). 22, 25, 26, 38, 91, 117

[61] H. Gomi, A. Takahashi, T. Ueda, H. Ito, and M. Aihara, Phys. Rev. B **71**, 045129 (2005). 22

[62] H. Itoh, A. Takahashi, and M. Aihara, Phys. Rev. B **73**, 075110 (2006). 22

[63] E. Collart, A. Shukla, J. P. Rueff, P. Leininger, H. Ishii, I. Jarrige, Y. Q. Cai, S. W. Cheong, and G. Dhalenne, Phys. Rev. Lett. **96**, 157004 (2006). 22, 25

[64] D. S. Ellis, J. P. Hill, S. Wakimoto, R. J. Birgeneau, D. Casa, T. Gog, and Y.-J. Kim, Phys. Rev. B **77**, 060501 (2008). 22, 25, 30, 38, 40

[65] E. Jeckelmann, Phys. Rev. B **67**, 075106 (2003). 22, 23, 24

[66] J. V. den Brink, M. B. J. Meinders, J. Lorenzana, R. Eder, and G. A. Sawatzky, Phys. Rev. Lett. **75**, 4658 (1995). 22

[67] F. B. Gallagher and S. Mazumdar, Phys. Rev. B **56**, 15025 (1997). 22

[68] R. Neudert, M. Knupfer, M. S. Golden, J. Fink, W. Stephan, K. Penc, N. Motoyama, H. Eisaki, and S. Uchida, Phys. Rev. Lett. **81**, 657 (1998). 22

[69] F. H. L. Essler, F. Gebhard, and E. Jeckelmann, Phys. Rev. B **64**, 125119 (2001). 22, 23, 24

[70] A. Hübsch, J. Richter, C. Waidacher, K. W. Becker, and W. von der Linden, Phys. Rev. B **63**, 205103 (2001). 22

[71] A. S. Moskvin, J. Málek, M. Knupfer, R. Neudert, J. Fink, R. Hayn, S. L. Drechsler, N. Motoyama, H. Eisaki, and S. Uchida, Phys. Rev. Lett. **91**, 037001 (2003). 22, 25, 26, 27, 30, 31, 38, 40, 91

[72] H. Matsueda, T. Tohyama, and S. Maekawa, Phys. Rev. B **71**, 153106 (2005). 22

[73] E. L. Lieb and F. Y. Wu, Phys. Rev. Lett. **20**, 1445 (1968). 24

[74] S. Tomonaga, Prog. Theor. Phys. **5**, 544 (1950). 24

[75] J. M. Luttinger, J. Math. Phys. **4**, 1154 (1963). 24

[76] R. Neudert, T. Boeske, O. Knauff, M. Knupfer, M. s Golden, G. Krabbes, J. Fink, H. Eisaki, and S. Uchida, Physica B **230-232**, 847 (1997). 25, 27, 38

[77] J. Fink, R. Neudert, H. C. Schmelz, T. Boeske, O. Knauff, S. Haffner, M. Knupfer, M. S. Golden, G. Krabbes, H. Eisaki, and S. Uchida, Physica B **237-238**, 93 (1997). 25, 27, 38

[78] A. S. Moskvin, S. L. Drechsler, R. Hayn, and J. Málek, Cond-mat , 0507707 (2005). 25, 26, 28, 30, 31, 38, 40, 91, 117

[79] J. J. M. Pothuizen, R. Eder, N. T. Hien, M. Matoba, A. A. Menovsky, and G. A. Sawatzky, Phys. Rev. Lett. **78**, 717 (1997). 28

[80] C. Duerr, S. Legner, R. Hayn, S. V. Borisenko, Z. Hu, A. Theresiak, M. Knupfer, M. S. Golden, J. Fink, R. Ronning, Z. X. Shen, H. Eisaki, S. Uchida, C. Janowitz, R. Mueller, R. L. Johnson, K. Rossnagel, L. Kipp, and G. Reichardt, Phys. Rev. B **63**, 014505 (2000). 28

[81] H. S. Choi, Y. S. Lee, T. W. Noh, E. J. Choi, Y. Bandg, and Y. J. Kim, Phys. Rev. B **4646**, 60 (1999). 28, 29, 30, 38, 40

[82] J. P. Falck, A. Levy, M. A. Kastner, and R. J. Birgeneau, Phys. Rev. Lett. **69**, 1109 (1992). 29, 30, 38, 40

[83] Y. Mizuno, T. Tohyama, S. Maekawa, T. Osafune, N. Motoyama, H. Eisaki, and S. Uchida, Phys. Rev. B **57**, 5326 (1998). 32, 33, 40

[84] S. Atzkern, M. Knupfer, and e. M Golden, ibid. **62**, 7845 (2000). 32

[85] J. Málek, S. L. Drechsler, U. Nitzsche, H. Rosner, and H. Eschrig, Cond. Mat. , arXiv:0807.0833 (2008). 32, 33, 40

[86] T. Osafune, N. Motoyama, H. Eisaki, and S. Uchida, Phys. Rev. Lett. **78**, 1980 (1997). 34, 35, 36, 40, 75, 76, 78, 80, 98, 100

[87] Z. V. Popović, M. J. Konstantinović, V. A. Ivanov, O. P. Khuong, R. Gaji, A. Vietkin, and V. V. Moshchalkov, Phys. Rev. B **62**, 4963 (2000). 34, 112

[88] H. Eisaki, N. Motoyama, K. M. Kojima, S. Uchida, N. Takeshita, and N. Mori, Physica C **341-348**, 363 (2000). 34, 98, 99

[89] H. Eskes, A. Oleś, M. Meinders, and W. Stephan, Phys. Rev. B **50**, 17980 (1994). 35

[90] Y. Mizuno, T. Tohyama, and S. Maekawa, J. Phys. Soc. Jpn. **66**, 937 (1997). 35, 36, 37, 40, 78

[91] M. Dressel and G. Grüner, *Electrodynamics of Solids: Optical Properties of Electrons in Matter*, Cambridge University Press, Cambridge, 2002. 42, 43, 84

[92] T. Möller, Doktorarbeit, Universität Köln, 2008. 45

[93] H. Kuzmany, *Solid-State Spectroscopy*, Springer-Verlag, Berlin, Heidelberg, 1998. 46

[94] M. Grüninger, M. Windt, T. Nunner, C. Knetter, K. P. Schmidt, G. S. Uhrig, T. Kopp, A. Freimuth, U. Ammerahl, B. Büchner, and A. Revcolevschi, J. Phys. Chem. Sol. **63**, 2167 (2002). 46

[95] A. Goessling, Doktorarbeit, Universität Köln, 2006. 46, 67

[96] M. Born and E. Wolf, *Principles of Optics*, Pergamon Press, Inc., New York, 1970. 47, 125

[97] G. G. Stokes, Trans. Camb. Phil. Soc. **9**, 399 (1852). 47

[98] W. A. Shurcliff, *Polarized Light*, Harvard University Press, Cambridge, Mass., 1962. 47, 48, 50, 51

[99] E. Hecht, *Optics*, Addison-Wesley Publishing Company, Reading, 1987. 47, 48, 49

[100] E. Hecht, Am. J. Phys. **38**, 1156 (1970). 47, 49

[101] M. J. Walker, Am. J. Phys. **22**, 170 (1954). 47, 50

[102] E. Collett, Am. J. Phys. **36**, 713 (1968). 47, 49

[103] H. Mueller, J. Phys. Soc. Jpn. **38**, 661 (1948). 50

[104] R. C. Jones, J. Opt. Soc. Amer. **31**, 488 (1941). 51

[105] J. A. W. Company, *A Short Course in Ellipsometry*, WVASE Manual, 2001. 53, 57

[106] D. E. Aspnes. 58, 69

[107] J. Gronholz and W. Herres, *Understanding FT-IR Data Processing*, Dr. Alfred Huethig Publishers, 1985. 60, 61

[108] B. Johs, Thin Solid Films **234**, 395 (1993). 66, 126

[109] J. M. Tranquada, J. D. Axe, N. Ichikawa, A. R. Moodenbaugh, Y. Nakamura, and S. Uchida, Phys. Rev. Lett. **78**, 338 (1997). 79

[110] J. B. Grant and A. K. McKahan, Phys. Rev. B **46**, 8422 (1992). 80

[111] V. Kataev, K.-Y. Choi, M. Grüninger, U. Ammerahl, B. Büchner, A. Freimuth, and A. Revcolevschi, Phys. Rev. B **64**, 104422 (2001). 81, 96, 122

[112] A. Gozar, G. Blumberg, P. B. Littlewood, B. S. Dennis, N. Motoyama, H. Eisaki, and S. Uchida, Phys. Rev. Lett. **91**, 087401 (2003). 81, 82

[113] A. Rusydi, M. Berciu, P. Abbamonte, S. Smadici, H. Eisaki, Y. Fujimaki, S. Uchida, M. Rübhausen, and G. A. Sawatzky, Phys. Rev. B **75**, 104510 (2007). 80, 82, 83, 84

[114] N. Nücker, M. Merz, C. A. Kuntscher, S. Gerhold, S. Schuppler, R. Neudert, M. S. Golden, J. Fink, D. Schild, S. Stadler, V. Chakarian, J. Freeland, Y. U. Idzerda, K. Conder, M. Uehara, T. Nagata, J. Goto, J. Akimitsu, N. Motoyama, H. Eisaki, S. Uchida, U. Ammerahl, and A. Revcolevschi, Phys. Rev. B **62**, 14384 (2000). 80, 82

[115] M. Matsuda, K. Katsumata, H. Eisaki, N. Motoyama, S. Uchida, S. M. Shapiro, and G. Shirane, Phys. Rev. B **53**, 12201 (1996). 81

[116] R. S. Eccleston, M. Uehara, J. Akimitsu, H. Eisaki, N. Motoyama, and S. Uchida, Phys. Rev. Lett. **81**, 1702 (1998). 81

[117] L. P. Regnault, J. P. Boucher, H. Moudden, J. E. Lorenzo, A. Hiess, U. Ammerahl, G. Dhalenne, and A. Revcolevschi, Phys. Rev. B **59**, 1055 (1999). 81

[118] U. Ammerahl, B. Büchner, L. Colonescu, R. Gross, and A. Revcolevschi, Phys. Rev. B **62**, 8630 (2000). 82

[119] S. R. White, R. M. Noack, and D. J. Scalapino, Phys. Rev. B **75**, 180501 (2007). 83

[120] C. Hilgers, *Optische Reflexionsmessungen an dotierten Spinleitern*, Diplomarbeit, Universität Köln, 2003. 96

[121] B. Ruzicka, L. Degiorgi, U. Ammerahl, G. Dhalenne, and A. Revcolevschi, Eur. Phys. J. B **6**, 301 (1998). 98

[122] Z. V. Popović, V. A. Ivanov, M. J. Konstantinović, A. Cantarero, J. Martínez-Pastor, D. Olguín, M. I. Alonso, M. Garriga, O. P. Khuong, A. Vietkin, and V. V. Moshchalkov, Phys. Rev. B **63**, 165105 (2001). 111, 112, 114, 115

[123] E. V. Benckiser, Doktorarbeit, Universität Köln, 2007. 112, 114, 117

[124] I. A. Zaliznyak, H. Woo, T. G. Perring, C. L. Broholm, C. D. Frost, and H. Takagi, Phys. Rev. Lett. **93**, 087202 (2004). 113, 114

[125] M. Z. Hasan, P. A. Montano, E. D. Isaacs, Z. X. Shen, H. Eisaki, S. K. Sinha, Z. Islam, N. Motoyama, and S. Uchida, Phys. Rev. Lett. **88**, 177403 (2002). 113

[126] W. Stephan and K. Penc, Phys. Rev. B **54**, R17269 (1996). 113

[127] P. Ribeiro, C. Hess, P. Reutler, and B. Büchner, J. Magn. and Magn. Mat. **290-291**, 334 (2005). 114

[128] M. Knupfer, R. Neudert, M. Kielwein, S. Haffner, M. S. Golden, J. Fink, C. Kim, Z. X. Shen, M. Merz, N. Nücker, S. Schuppler, N. Motoyama, H. Eisaki, S. Uchida, Z. Hu, M. Domke, and G. Kaindl, Phys. Rev. B **55**, R7291 (1997). 114

Danksagung

Mein ganz besonderer Dank gilt meinem Doktorvater, Herrn Professor Dr. Axel Freimuth, der seine Doktoranden stets fördert und unterstützt. Er besitzt die Gabe, seine Mitarbeiter motivieren und begeistern zu können und hat zudem noch stets ein offenes Ohr für die Sorgen und Nöte eines verzweifelten Doktoranden. Vielen Dank für kurzfristige Audienzen im Rektorat, das Aufpäppeln der Moral und Hilfe im Ernstfall!

Prof. Dr. Markus Grüninger danke ich für die Betreuung dieser Arbeit, die Verbesserungsvorschläge und Diskussionen sowie seine Beharrlichkeit, wenn es darum geht, den Dingen auf den Grund zu gehen. Dank für die Gründung der Optikertruppe!

Professor L.H. Tjeng für seine Unterstüztung in der Endphase der Doktorarbeit.

Herrn Professor Dr. L. Bohatý für die Übernahme des Prüfungsvorsitzes.

Meinen lieben Optikern Eva Benckiser, Reinhard Rückamp, Alexander Gößling, Thomas Möller, Julia Küppersbusch und Louis Mäder danke ich für die gute Zusammenarbeit und allseits beste Stimmung. Ich hoffe, wir werden in Kontakt bleiben. Mein besonderer Dank gilt Eva für ihre Freundschaft, die 1A Zusammenarbeit, Kletterausflüge und die immer gute Stimmung. Die gemeinsame Zeit im Inschtitut möchte ich nicht missen. Alex danke ich für die lehrreiche und interessante kollegiale Tüftelei am Ellipsometer. Auch wenn wir zum Thema Kabelbinder wahrscheinlich nie einer Meinung sein werden, hat es mir sehr viel Spaß gemacht, die Elli mit Dir aufzubauen. Dank auch für hilfreiche Tipps und Tricks beim Auswerten. Reinhard, dem Organisationstalent und Mann für die Symmetrie Danke ich für all seine Untersützung, Aufmunterung, seinen unermüdlichen Optimismuns und die interessanten Diskussionen über die Gruppentheorie. Thomas danke ich für das neue benutzbare Krakro-Programm. Ohne dies wäre ich jetzt nicht hier. Julia Danke ich für das rege Interesse und die spannenden Diskussionen über die Ellipsometrie. Das war prima und es ist gut zu wissen, dass das Ellipsometer in guten Händen ist.

Carmen Handels, der guten Seele des Instituts danke ich für ihre Unterstützung in Zeiten, die manchmal so gar nicht lustig waren. Ich hoffe, Carmen bleibt noch lange am Institut und wäscht den Jungs hin und wieder mal den Kopf. Inge Simons, die das Institut am allerbesten kennt, danke ich, dass sie stets mit Rat und Tat hilfreich zur Seite steht.

Niko Johannsen (Botschafter der Wahrheit), Holger Roth (König), Martin Valldor (GOTT oder der Schwede) und Oliver Heyer (der Stoiker). Vielen Dank für

das Refugium in Zimmer 218, in dem Becherpalmen wachsen und ein freier Wind weht. Besonderer Dank gilt natürlich Niko, der mich immer wieder an die wirklich wichtigen Dinge des Lebens erinnert. Danke für Deine Freundschaft, Mettmännchen und Käsebällchen.

Thomas Lorenz, Kai Berggold, Jörg Baier, den alten Transportlern für die lustigen Gespräche über Kryostatfüllstrategien und herausfliegende Messstäbe. Immer wieder ein Erlebnis. Dank für kurzzeitige Aufnahme in die Radltruppe und Mitnahme auf die (kleine) Dienstagsrunde. Spezieller Dank an Thomas Lorenz für wirklich hilfreiche und anschauliche Diskussionen über Physik, sogar Optik wenn es sein muss. Herzlichen Dank auch für das Aushalten diverser Probevorträge und die konstruktiven Tipps danach.

Daniel Senff für alte und neue gute Kollegenschaft, die Schwätzchen zwischendurch, die Unterstützung beim Formatieren dieser Arbeit und das Korrekturlesen diverser Kapitel.

Den Mitarbeitern der Mechanik- und Elektronikwerkstätten für die Geduld, mit der uns immer wieder erklärt wurde, was geht und was nicht und wie eine technische Zeichnung eigentlich auszusehen hat. Herrn Külzer, Herrn Hansmann und Herrn Menz gilt hier mein besonderer Dank für die große Hilfsbereitschaft. Ihre Lösungsvorschläge waren stets die besten. Und natürlich danke ich der gesamten Besatzung für das Ausrichten der jährlichen Grillfeste. Rolf Dommel, Herr über das Helium, vielen Dank für die zuverlässige Versorgung mit dem Stoff und das Überleben im Keller, für erlebnisreiche Institutsfeiern dank des Aufpeppens des weihnachtlichen Glühweins. Lucie Hamdan für die Weitergabe ihres großen Know-Hows zum Thema UHV-Technik und die Möglichkeit, sich immer mal wieder ein Ersatzteil oder Werkzeug zu klauen. Ralf Müller für die Versorgung mit allem was so man braucht, auch wenn es eigentlich unmöglich ist. Andrea Severing für die Organisation des SFBs und zahlreiche gute Gespräche.

Ich danke meinen neuen Kollegen im VDI Technologiezentrum für die gute Arbeitsatmosphäre, die vielen Aufmunterungen und die Aussicht auf ein Leben danach. Jochen Dreßen, dem noch nicht einmal die Spinleitern fremd sind, für sein Verständnis im Falle äußerst kurzfristiger Urlaubsanträge im Dienste der Doktorarbeit und Schaffung eines Anreizes, die Abgabe schnell voranzutreiben.

An dieser Stelle ein besonderer Dank an *Die Mülheimer Blase* Carsten, Anika, Holger, Niko, Rita und Klaus. Vielen Dank, dass ihr mich während meiner arbeitssamen Zeit ertragen und immer wieder aufgemuntert habt. Für das Leben im Mülheimer Hinterhof, die wunderbaren Sommer im Garten und das köstliche Essen kann ich gar nicht oft genug danken. Ihr werdet hoffentlich immer die Heimatbasis bleiben. Meinen besten Freundinnen Heike (Tiffi) Hübener und Kathrin (Schmittie) Schaarschmidt dafür, dass wir gemeinsam durch dick und dünn gehen. Ejal watt och passiert. Anika und Florian für die glorreichen Soprano-Abende und vieles mehr! Meinen Eltern, meiner Schwester Michaela und meinem Schwager Oliver dafür, dass Sie immer für mich da sind. Meinen süßen Nichten Sophie und

Alice danke ich dafür dass es sie gibt und sie mich immer zum Lachen bringen. Und ja, ich gedenke, sie mit Tantenliebe zu überschütten. Ursel und Otto Borchert, Rosemarie und Eberhard Heimann für ihre Anteilnahme, den guten Zuspruch, Care-Pakete und ihre Freundschaft.

Mein größter Dank gilt Carsten, der mich auch noch lieb umsorgt hat, wenn ich wirklich ungenießbar war, ohne den ich das alles so nicht geschafft hätte. Danke für die unermüdliche Unterstützung, Ruhe und Verständnis. Ich wiederhole mich, ohne ihn wäre ich sicherlich längst verhungert.

Der Deutschen Forschungsgemeinschaft (DFG) für die Finazierung meiner Doktorandenstelle im Rahmen des SFB 608.

Offizielle Erklärung

Ich versichere, dass ich die von mir vorgelegte Dissertation selbständig angefertigt, die benutzten Quellen und Hilfsmittel vollständig angegeben und die Stellen der Arbeit - einschließlich Tabellen, Karten und Abbildungen -, die anderen Werken im Wortlaut oder dem Sinn nach entnommen sind, in jedem Einzelfall als Entlehnung kenntlich gemacht habe; daß diese Dissertation noch keiner anderen Fakultät oder Universität zur Prüfung vorgelegen hat; daß sie noch nicht veröffentlicht worden ist sowie, daß ich eine solche Veröffentlichung vor Abschluß des Promotionsverfahrens nicht vornehmen werde. Die Bestimmungen dieser Promotionsordnung sind mir bekannt. Die von mir vorgelegte Dissertation ist von Prof. Dr. M. Grüninger betreut worden.

Köln, den 10. Februar 2009

Christina Hilgers

Kurzzusammenfassung

Im Rahmen dieser Doktorarbeit wurde ein spektroskopisches Ellipsometer zusammen mit einem UHV-Durchflusskryostat in Betrieb genommen. Ziel war die Ermöglichung optischer Untersuchungen an Übergangsmetalloxiden und Dünnschichtsystemen bei tiefen Temperaturen in einem Energiebereich zwischen 0,8 und 5 eV. Nach erfolgreicher Inbetriebnahme des Ellipsometers erfolgte die systematische Untersuchung von Kuperoxid-Spinleiterverbindungen mit verschiedenen Dotierungen. Hierbei handelt es sich um das mit 0.2 Löchern pro Einheitszelle dotierte $La_{5.2}Ca_{8.8}Cu_{24}O_{41}$ und das System $Sr_{14-x}Ca_xCu_{24}O_{41}$ (x = 0, 5 und 8), welches mit 6 Löchern pro Einheitszelle dotiert ist. Die optische Leitfähigkeit der hochkorrelierten Elektronensysteme wurde ellipsometrisch bestimmt und mit Daten der optischen Leitfähigkeit aus Fourierspektroskopiemessungen kombiniert. Die Abhängigkeit der optischen Interbandanregungen von der Temperatur, der Loch- und der Kalziumdotierung wurde untersucht. Die Interbandanregungen entlang der drei kristallographischen Achsen sind stark anisotrop und zeigen in zwei Richtungen eine Multipeakstruktur. Anhand eines Drude-Lorentz Modells und durch Vergleich mit der Literatur konnte eine Zuweisung der Anregungen in der komplizierten Struktur vorgenommen werden Die niedrigste Ladungstransferanregung in $\sigma_c(\omega)$ wird als exzitonische Resonanz mit entsprechenden Kontinuum bei höherer Energie erklärt. Diese Aussage wird durch die Temperaturabhängigkeit des spektralen Gewichts der beiden Anregungen unterstützt. Durch Kombination von Reflexions- und Transmissionsdaten aus Fourierspektroskopiemessungen mit den ellipsometrischen Messungen wurde mittels Kramers-Kronig Transformation die optische Leitfähigkeit $\sigma_c(\omega)$ von 10 meV bis 5 eV ermittelt. Durch eine Analyse des spektralen Gewichtstransfers konnte die Temperaturabhängigkeit der Interbandanregungen mit einem Ladungstransfer hin zu niedrigeren Energien erklärt werden. Darüber hinaus zeigte die Untersuchung des spektralen Gewichts eine Abhängigkeit von der Dotierung x. Neben den Spinleitersystemen wurde die optische Leitfähigkeit der eindimensionalen Spinkette $SrCuO_2$ entlang der Richtung der Kette und senkrecht dazu bestimmt. Das Elektron-Loch-Anregungsspektrum zeigt eine starke, sehr steil ansteigende Absorption nahe der Bandlücke, die in der Literatur im Rahmen einer exzitonischen Resonanz diskutiert wird. Wir vergleichen die Ergebnisse der eindimensionalen Kette mit denen der Spinleitern mit dem Ziel, der Formulierung einer einheitlichen Beschreibung der Interbandanregungen näher zu kommen.

Abstract

Within the scope of this thesis, a spectroscopic ellipsometer has been put into operation and equipped with a UHV liquid Helium flow cryostat to enable low temperature optical measurements down to 10 K in the energy range between 0.8 to 5 eV. After successful installation of the ellipsometer, a systematic investigation of the electronic structure of one-dimensional copper-oxide spin ladders and spin chains was carried out. Ellipsometric optical conductivity data of the biaxial copper oxide compounds $La_{5.2}Ca_{8.8}Cu_{24}O_{41}$ (LCO) with 0.2 holes per formula unit and $Sr_{14-x}Ca_xCu_{24}O_{41}$ for x = 0 (SCO) and x = 5, 8 (SCCO), doped with 6 holes per formula unit, were derived in all three crystallographic axes. We investigated the temperature, hole-doping and Ca-doping dependence of the interband excitations. We find a multipeak structure in the interband region in the two crystallographic directions a and c. A pronounced temperature dependence in $\sigma_c(\omega)$ is observed. We investigated the dependence of those absorptions on temperature and Ca content and identified them with CT excitations of different character by using a Drude-Lorentz parameter fit and by comparison with the literature. We find a new interpretation of the lowest interband excitation in σ_c that we identify with a ZN excitonic resonance (a ZN exciton is described as a bound pair of empty site Cu^+ and a Zhang-Rice singlet state on a neighboring site) and the corresponding continuum at higher energy. A new absorption observed in x = 0 shows a strong dependence on temperature that could be related to charge-ordering temperatures in SCO. To further investigate the temperature dependence of the optical spectra along c at low energy, we combined the ellipsometric data with far and mid-infrared reflectance and transmittance data from FT spectroscopy and performed a Kramers-Kronig transformation followed by a spectral-weight analysis. This showed a spectral-weight transfer from the CT-region to the low-energy region with rising temperature in x = 0, 5, and 8. Moreover, a spectral weight shift with Ca substitution x is observed below 2.5 eV. Another compound investigated by ellipsometry within the scope of this thesis was the 1D zigzag chain $SrCuO_2$. We investigated $\sigma_c(\omega)$ along the chains and $\sigma_a(\omega)$ perpendicular to the chains as a function of temperature. The spectrum shows a prominent absorption feature at 2 eV that is assigned to a charge-transfer excitonic resonance and one with lower intensity at 4.2 eV that is assigned to one-center charge transfer excitation similar to those observed in basically all low dimensional copper oxides. In summary, the data show that a unified picture might be found for the electron hole excitations in low dimensional cuprates.